REAL-TIME BAYESIAN ESTIMATION AND FEEDBACK CONTROL WITH A NITROGEN VACANCY CENTER IN DIAMOND

by

ETHAN TURNER

A DISSERTATION

Presented to the Department of Physics
and the Division of Graduate Studies of the University of Oregon
in partial fulfillment of the requirements
for the degree of
Doctor of Philosophy

June 2022

DISSERTATION APPROVAL PAGE

Student: Ethan Turner

Title: Real-Time Bayesian Estimation and Feedback control with a Nitrogen Vacancy Center in Diamond

This dissertation has been accepted and approved in partial fulfillment of the requirements for the Doctor of Philosophy degree in the Department of Physics by:

Dr. Steven Van Enk	Chairperson
Dr. Hailin Wang	Advisor
Dr. David Allcock	Core Member
Dr. Andrew Marcus	Institutional Representative

and

Krista Chronister	Vice Provost for Graduate Studies

Original approval signatures are on file with the University of Oregon Division of Graduate Studies.

Degree awarded June 2022

DISSERTATION ABSTRACT

Ethan Turner

Doctor of Philosophy

Department of Physics

June 2022

Title: Real-Time Bayesian Estimation and Feedback control with a Nitrogen Vacancy Center in Diamond

Quantum sensing utilizes the sensitivity of a quantum system to a given physical quantity in order to derive an estimate for that physical quantity. Nitrogen vacancy (NV) centers in diamond have emerged as a popular quantum system for sensing purposes. Due to their sensitivity to a wide variety of physical quantities, NV centers in single and ensemble densities have been employed as magnetometers, electrometers, pressure sensors, and thermometers. While sensing of static and periodic signals has been achieved at nanoscale resolutions, time-varying signals are still under study. In this dissertation we demonstrate real-time sensing of a time-varying magnetic field using a single NV center placed in the dark state via coherent population trapping. Estimation carried out by a Bayesian inference-based estimator generates estimates of the field with the detection of a single photon. The estimator's sensitivity to statistical parameters of the fluctuating magnetic field allows for parameter optimization using feedback

control. Real-time magnetometry using a single solid-state spin can add a new and powerful tool to quantum sensing.

This dissertation contains previously published and unpublished material.

ACKNOWLEDGEMENTS

Thank you to the Wang lab for the work that we have all accomplished together and for the support provided. Thank you Mark Kuzyk for showing me the ropes and helping me lay the foundation for the rest of my time in lab. Thank you to Ignas Lekavicius for teaching me how to use the cold temperature setup and always being there to help with troubleshooting (even after you graduated). Thank you Abigail Pauls for our conversations from politics to Star Trek, for helping me clean the lab, for your words of encouragement when working in the dark felt overwhelming, and most of all, for your unwavering comradery which I will undoubtedly miss. Thank you to Shuhao Wu for being such a collaborative, curious, and fun lab partner and friend. Completion of the projects in this thesis would have taken many more years without you. Thank you to Xinzhu Li for your excellent fabrication skills, encouragement and questions. Finally, I would like to thank my advisor, Hailin Wang, for always having your door open, available for questions about the lab and for providing me with the resources to carry out these experiments. It has been a pleasure to work with you all and to get to know you.

I would also like to thank all the teachers and mentors that have shaped me into the scientist I am. Thank you to the teachers of Chittenango High School, especially to Ms. Carpenter, my first physics teacher, for your enthusiastic introduction to physics and to Mr. & Mrs. Clancy for helping me realize that I had a knack for mathematics and encouraging me to explore where it could take me. Thank you to the SUNY Geneseo physics department for passing on the knowledge and motivation that I needed to finish this thesis and to Dr. Padalino and Dr. Marcus for my initiation into research. Education is the gift that keeps on giving.

I dedicate this dissertation to my family and friends.

Thank you all for your support.

TABLE OF CONTENTS

LIST OF TABLES

CHAPTER I

INTRODUCTION

Technological advancements of the last decade have generated remarkable strides towards reliable control of quantum systems. These advancements coupled with rigorous studies of quantum systems have enabled the construction of a variety of quantum technologies [1, 2] from quantum cryptography [3], to enhanced imaging and sensing [4, 5, 6] and quantum computers [7, 8]. An essential feature of all quantum technologies is quantum coherence, which allows for reliable operation of a quantum system. Any practical quantum system is coupled in some way to its environment, causing the phase relation between quantum states to decohere and consequentially limiting the utility of the system. While decoherence gives the impression of quantum malevolence, studying its effects can be helpful in uncovering information about the quantum system and its surrounding environment.

Magnetic fields are a significant source of decoherence in a variety of quantum systems. Fluctuating magnetic fields can be found in magnetic films and heterostrucures [9], 2D magnetic materials [10], and biological systems [11]. Specifically, the nitrogen vacancy (NV) center in diamond, the subject of this dissertation, is surrounded by a bath of ^{13}C nuclear spins that generate randomly time-varying magnetic field fluctuations. The spin bath couples with the NV center spin, randomly shifting its ground spin states, lowering the coherence time from its electronic spin lifetime limited (≈ 1 ms) by three orders of magnitude [12, 13, 14]. Quantum magnetometry, applied to these systems, can provide important physical insights for understanding these materials.

1

In this dissertation, we develop a novel quantum sensor using nitrogen vacancy (NV) centers in diamond to demonstrate real-time sensing of a magnetic field using coherent population trapping (CPT). Additionally, we introduce a feedback process that stabilizes the NV center in the presence of the fluctuating field. This process can be used to infer information about the spin bath environment surrounding the NV center which is a primary cause of its decoherence. We then provide a technique for improving the sensitivity of our sensor using nuclear spin pumping.

1.1. Quantum Sensing

Quantum sensing employs the fundamental sensitivity of a quantum system to its environment for measurement of a physical quantity [15]. These quantities range from electric and magnetic fields to temperature and pressure. While sensitivity to these quantities is typically seen as an obstacle to overcome in fields such as quantum computing, quantum sensing reframes these susceptibilities as a tool for learning about quantum systems. Atomic clocks [16], precision spectroscopy, and nuclear magnetic resonance are each historic examples of quantum sensing prior to the development of quantum sensing as a sub-field. Valued progress in the field of quantum sensing involves the design and engineering of quantum systems for sensing purposes with the goal of reaching new regimes of sensitivity from nanometer resolution in materials [17] to the detection of dark matter[18].

The fundamental descriptors of a quantum sensor [15] include (1) the use of a quantum object to measure a physical quantity. The quantum object typically has well resolved, discrete energy levels that are sensitive to the quantity to be

2

sensed. (2) The use of quantum coherence to measure a physical quantity. (3) The use of entanglement to improve the sensitivity or precision of a measurement beyond classical means. Entanglement-assisted sensing is also referred to as quantum metrology [6, 19, 20].

1.2. Quantum Sensors

For general sensing applications, a physical process (e.g. temperature change) induces a response in a well characterized sensor (thermometer). Due to the known reactivity of the sensor, i.e. calibration, the response can be converted into a metric (temperature). Quantum sensors use this same process to detect a physical quantity that shifts the discrete energy levels of a quantum system.

There are criteria for selecting a quantum sensor. The first is that the sensor must have discrete and resolvable energy levels. Next, the sensor must be capable of quantum state initialization and easy read-out so that information can be extracted from the system. Often the system is coherently manipulated, typically with the use of external fields. The physical characteristics of the sensor determines the physical quantity that it is sensitive to. Charged-based sensors typically detect electric fields and spin-based sensors can be used to detect magnetic fields. Some sensors, such as NV centers, can be used to detect multiple quantities.

Another important characteristic of a sensor is its sensitivity to stimuli. The sensor must be sensitive to the desired measurable quantity but must also be robust to other physical noise. This sensitivity is determined by the stability of the sensor's descrete quantum states and the scale at which those levels can be shifted. The stability of a sensor's quantum states is limited by the state

population decay and the decay of coherence between states, these are typically referred to as lifetime and decoherence rates.

When it comes to choosing a sensor for a particular task, there are a multitude of quantum sensors being developed today, each with its own unique advantages and disadvantages. With the increased development of atomic vapor based quantum computing so has the ability for atoms to be employed as quantum sensors. Being a spin-based sensor, a thermal vapor of atoms can be used as a magnetic field sensor and has achieved sensitivities in the range of 100×10^{-18} T/$\sqrt{\text{Hz}}$ [5, 21, 22]. Similarly, electromagnetically trapped ions have been used as electric field sensors capable of sensing electric forces as low as 1×10^{-24}N/$\sqrt{\text{Hz}}$ using quantized motional states [23, 24] as well as magnetic fields as low as 4.6×10^{-12} T/$\sqrt{\text{Hz}}$ using the ground state spin sublevels [25]. Such work has also lead to development of dynamical decoupling which can be used to measure the frequency of oscillating magnetic fields such as nuclear spin precession [24].

1.2.1. Solid State Sensors

Another useful class of quantum sensors are those that lie within solid state media. Solid state hosts allow for much larger densities of sensors than their atomic counterparts [26]. One of the oldest of these technologies are those that use nuclear magnetic resonance (NMR), used to determine magnetic field strength by measuring the Larmor precession of an atom's nuclear spin. NMR techniques have a variety of applications from *in situ* and dynamical field mapping in magnetic resonance imaging (MRI), and gyroscopes [15].

Solid state quantum sensors can also be made out of electronic defects in a host material. The most widely studied solid-state quantum sensor, and the focus

of this dissertation, is the nitrogen vacancy (NV) center in diamond. NV centers can be grown in a range of densities, parts-per-billion to parts-per-million, in diamond sizes from 5 nm to 10 mm [17]. The defect can be initialized and readout optically for sensing purposes at cryogenic and room temperatures. For densely doped diamonds, NV ensembles have been used for biological imaging [27] and mapping microscopic magnetic inclusions in meteorites [28]. Additionally, spin coherence times of high density ensembles are reduced by 100-1000 times due to an excess of substitutional nitrogen spins inherent to the strongly doped samples [15].

Single NV centers have also been used for a variety of applications such as magnetometers [26], electrometers [29], pressure sensors [30], and thermometers [31]. Single NV centers are able to be individually addressed optically using a confocal setup, which enables sensing of a local environment without disturbing other nearby defects. Another advantage of NV centers is that they are firmly trapped within a solid. In order to detect nanometer resolution magnetic fields one needs to bring their sensors as close to the field source as possible, which is difficult to achieve using an atomic vapor tube. Single NV centers are able to be implanted within 5 nm of a diamond surface with coherence times as high as 100 μs [32].

NVs have been useful for detecting time varying signals as well as static signals. Such efforts primarily employ Ramsey interferometry [26, 33] which limits the sensing window of the NV to a snapshot in time. For sensing periodic signals Ramsey interferometry can only sense slowly varying signals with frequencies on the order of the sensing window [15]. This is solved using multipulse techniques based on spin - echos [34] such as the Car-Purcell pulse sequence [35] and periodic dynamical-decoupling [36]. Such techniques can be used to refocus the decoherence

caused by the surrounding spin bath of the NV [37, 38]. However, such multipulse procedures require long pulse sequences that accumulate pulse shaping errors and imposes disruptive forces on the quantum system under study. Magnetometry procedures that are discussed in this dissertation occur in real-time and are minimally invasive to surrounding quantum systems.

Particularly, in this dissertation, we demonstrate a real-time sensing procedure that uses a three-level quantum system instead of the two-level systems used in traditional quantum sensing techniques [15]. To do this we monitor the fluorescence of the NV while we place it in a special quantum superposition known as the dark state. The dark state gets its name due to destructive quantum interference that prevents the state from being optically excited, preventing optical decay and the emission of a photon. Such a state is achieved with the use of coherent population trapping (CPT). Fluctuations caused by local magnetic fields can disrupt the conditions that place the NV in the dark state, allowing for excitation and the emission of a photon. The degree of which the dark state fluoresces is then determined by the detuning of the applied fields. By monitoring the spectral response of a CPT curve, which has been used for static sensing [39], in addition to using a Bayesian inference technique we can update our estimation of a time-varying magnetic field with the detection of a single-photon. The temporal resolution of the sensor is therefore set by the computation latency (μs) and the photon count rate (kHz) which is determined by the optical power of the CPT fields and its sensitivity to magnetic field fluctuations is set by the linewidth of the CPT spectral response. The figures of merit for quantum sensors applied to static and periodic signals cannot be directly compared to the sensor discussed in this dissertation due to trade-offs between its resolution and sensitivity. In

6

this dissertation we sense magnetic field fluctuation amplitudes with a standard deviation as low as 0.18 G and real time dynamics as fast as 0.1 ms.

Furthermore, since the estimation occurs in real time, we can also provide real-time feedback control to counteract fluctuations imposed on the NV and it's surroundings as they occur. We introduce a feedback mechanism to our real-time sensor and verify performance using Ramsey interferometry to measure the improved spin-decoherence time of the ground state, T_2^*. By adjusting the input parameters used to estimate the time-varying magnetic field, we can determine the statistical parameters of the fluctuating field. This presents a promising technique for characterizing the solid state environment that surrounds a solid state spin.

Additionally we demonstrate steps towards increasing the sensitivity of the NV. By polarizing the nuclear spin of the NV center we can eliminate linewidth contributions that arise from the three hyperfine NV states. This is carried out using nuclear spin pumping which utilizes the total-spin conserving optical transitions of the NV center's excited state to initialize the hyperfine state of the NV via optically forbidden transitions. The result is a smaller CPT linewidth and therefore a steeper spectral response, increasing sensitivity, and enabling the sensing of smaller magnitude fluctuations born from decoherence sources such as the ^{13}C spin bath.

1.3. Dissertation Outline

In the first few chapters we introduce the NV and the various quantum control techniques required for real-time estimation. In Chapter II, we describe the NV center's physical and electronic structure which dictates the quantum states it can occupy. We then explore the NV center ground state down to the hyperfine

7

interaction. Next, we discuss how to access the individual states of the NV center's excited state manifold and how they are affected by external forces such as strain. In Chapter III, we provide an outline of the experimental setup used throughout the dissertation. We also touch upon the fundamentals of NV ground state control such as optically detected magnetic resonance (ODMR), Rabi oscillations, and Ramsey interferometry using microwaves and present preliminary results. In Chapter IV, we provide the theoretical background of CPT. We describe the experimental procedure for accessing the dark state and show that the hyperfine states of the NV center can be resolved using CPT as well.

In Chapter V we demonstrate real-time estimation of a time varying magnetic field. We discuss the various estimators and their theoretical background used as well as the theoretical estimation bounds that can be achieved. We discuss how those estimators can be compared and compare their performance to the theoretical bound. For the next chapter (VI), feedback control is employed to counteract magnetic field fluctuations imposed on the NV. We observe improvement in the spin decoherence time via the Ramsey interferometry. We optimize this improvement to estimate the parameters of the fluctuating field. In Chapter VII, we demonstrate an approach towards nuclear spin polarization using forbidden optical transitions and MW control in a strain regime in the NV that has yet to be explored. We then wrap up our discussion in Chapter VIII by summarizing our findings and provide direction for further work to progress the field.

1.4. List of Acronyms used in this Dissertation

NV - Nitrogen Vacancy Center

MW - Microwave

ODMR - Optically Detected Magnetic Resonance

EOM - Electro-Optical Modulator

CPT - Coherent Population Trapping

FPGA- Field Programmable Gate Array

OU Process - Ornstein-Uhlenbeck Process

CRLB - Cramer-Rao Lower Bound

CPW - Coplanar Waveguide

BPE - Bayesian Parameter Estimation

CHAPTER II

THE NITROGEN VACANCY CENTER

2.1. Electronic Structure

The nitrogen vacancy center is a color center located at a point in a diamond lattice. Color centers are defects within a crystalline medium that can absorb and emit light at a specific color or wavelength. Diamonds host a large band gap (5.5 eV) which allows for color centers to be optically addressed in the largely transparent medium. In addition to its optical properties, diamonds make an excellent host material for solid state quantum sensors as it is chemically inert, has a remarkably fast speed of sound (12,000 m/s), and a high Debye temperature (2250 K). While NV centers occur naturally in diamond, they can also be grown in the lab with engineered abundance using microwave assisted chemical vapor deposition (CVD) [11] or implanted in the diamond surface [40][32]. Nitrogen abundances range between < 1 parts-per-million (type IIa) and 200 parts-per-million (type Ib) for single and ensemble NV applications respectively [41]. High purity samples of < 5 parts-per-billion have been achieved in "electronics grade" diamonds [41]. The final lattice environment primarily consists of ^{12}C isotopes, however the non-zero spin ^{13}C isotope has non-negligible abundance.

The nitrogen vacancy center is composed of a substitutional nitrogen with an adjacent vacancy (Figure 2.1) located at a point in the carbon lattice of diamond. Spatially, the various dangling bonds that surround the vacancy exhibit a C_{3v} symmetry, oriented along the [111] crystalline direction [42]. Each carbon bond donates a single electron to the orbital structure while the nitrogen atom

10

provides two. The electrons occupy orbital states shown in Figure 2.1b dictated by combinations of dangling bonds that satisfy the C_{3v} symmetry [41]. Two stable charge states exists for the NV, the neutral NV^0 and the negative NV^- [43]. The NV^0 has 5 electrons making it a spin-1/2 system with a zero phonon line (ZPL) located at 520 nm. The NV^- accepts an electron from the diamond's valance band [44] and has a zero phonon line located at 637 nm [45]. This leaves the NV^- with a total of six electrons, yielding a total spin of $S = 1$ and an effective orbital structure of $1s2sp^3$. The NV^- will be the primary focus of this dissertation and from here on will be referred to simply as "NV" unless otherwise stated.
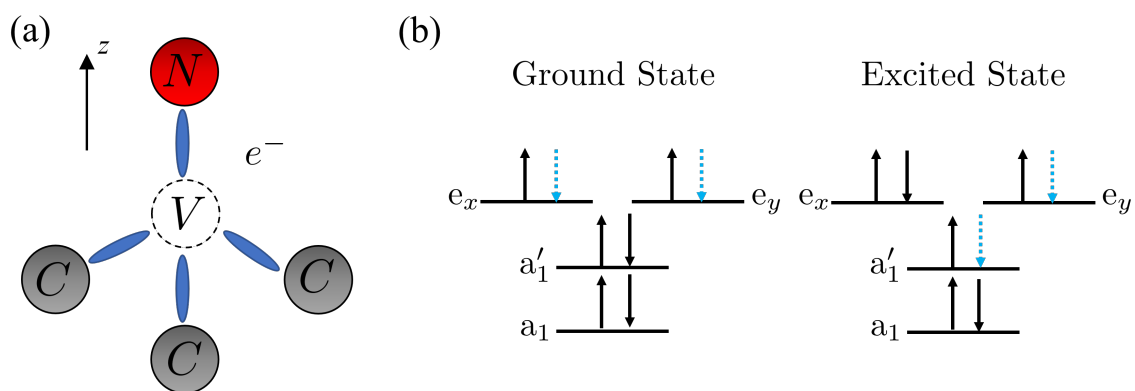
FIGURE 2.1. (a) Physical structure of the NV. (b) Electron occupation of orbital states a_1, a_1', e_x and e_y.

2.2. Ground State

The ground state of the NV center is a spin triplet $(S = 1, m_s = 0, \pm 1)$ which can be described by its ground state Hamiltonian,

$$H_{gs} = D_{gs}(S_z - S(S+1)/3) + A_{gs}^{\parallel}S_zI_z + A_{gs}^{\perp}(S_xI_x + S_yI_y) + P_{gs}(I_z + I(I+1)/3)$$

(2.1)

where the $m_s = 0$ spin projection is separated from the degenerate non-zero spin projections, $m_s = \pm 1$, by a zero-field splitting of $D_{gs} = 2.88$ GHz (Figure 2.2) [42]. We will sometimes refer to the electronic projection states as $|0\rangle$ and $|\pm 1\rangle$. Degeneracy of the $m_s = \pm 1$ projections is lifted by the application of an external magnetic field via the Zeeman interaction. The Zeeman interaction adds a $\gamma_{NV}\vec{B}\cdot\vec{S}$ term to the NV ground state Hamiltonian where $\gamma_{NV} = g\mu_B \approx 2.8$ MHz/G is the gyromagnetic ratio of the NV. This factor scales the sensitivity of our magnetic field sensor when applied to the real time sensing experiment discussed in Chapter V.

The hyperfine interaction also plays a role in the ground state structure. The nitrogen isotope with the largest abundance in diamond is ^{14}N, whose total nuclear spin is $I = 1$, with spin projections $m_I = 0, \pm 1$. The hyperfine interaction couples the $m_s = \pm 1$ spin projections with each nuclear spin projection m_I. This results in a hyperfine splitting of $A_{gs}^{\parallel} = $ -2.2 MHz between each nuclear spin projection and a nuclear quadrupole shift of $P_{gs} = -5$ MHz systematically lowers the nonzero nuclear spin projections [42].
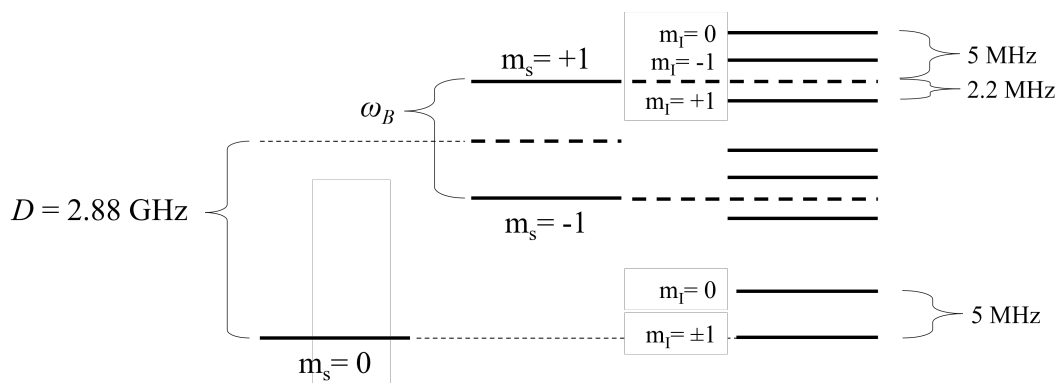
FIGURE 2.2. Ground state manifold of the NV center. D is the zero field splitting and ω_B is Zeeman splitting. The nuclear spin states are further split by the quadrapole interaction (5 MHz) and the hyperfine interaction (2.2 MHz).

2.3. Excited State

The NV center's excited state is accessed by the promotion of an s-orbital electron to one of the p-orbitals via optical excitation. The energy required for excitation is determined primarily determined by the Coulomb interaction which has a magnitude of 1.94 eV corresponding to a ZPL of 637 nm (Figure 2.3). Beyond the excited state there exists a continuum of vibronic states otherwise referred to as a phononic sideband (PSB) which extends to 800 nm [42]. The excited state manifold is both an orbital doublet and a spin triplet yielding six unique states ($|E_{x,y}\rangle$, $|E_{1,2}\rangle$, $|A_{1,2}\rangle$). The spin character of each state dictates the selection rules of each transition from the NV ground state. States $|E_{x,y}\rangle$ are of $m_s = 0$ character while $|A_{1,2}\rangle$ and $|E_{1,2}\rangle$ are of non-zero spin character. The contribution of the spin-orbit and spin-spin interactions, H_{so} and H_{ss} respectively, further jostle the states about in the manifold. Their Hamiltonians are

$$H_{so} = \lambda_z(|A_1\rangle\langle A_2| + |A_2\rangle\langle A_2| - |E_1\rangle\langle E_1| - |E_2\rangle\langle E_2|) \tag{2.2}$$

$$H_{ss} = \Delta(|A_1\rangle\langle A_2| + |A_2\rangle\langle A_2| + |E_1\rangle\langle E_1| + |E_2\rangle\langle E_2|)$$
$$-2\Delta(|E_x\rangle\langle E_x| + |E_y\rangle\langle E_y|) + \Delta'(|A_2\rangle\langle A_2| - |A_1\rangle\langle A_1|) \tag{2.3}$$
$$+\Delta''(|E_1\rangle\langle E_y| + |E_y\rangle\langle E_1| - i|E_2\rangle\langle E_x| + i|E_x\rangle\langle E_2|)$$

where λ_z is the spin orbit interaction, $3\Delta = 1.42\text{GHz}$ and $\Delta' = 1.55$ GHz are the spin-spin contributions. Δ'' leads to the non-spin conserving cross transitions that play a role in optical pumping [41].

The NV can be optically addressed using the resonant ZPL at 637 nm or non-resonantly at 532 nm. Resonant excited state transitions are sensitive to the polarization of the excitation light. Each transition is total spin conserving and

13
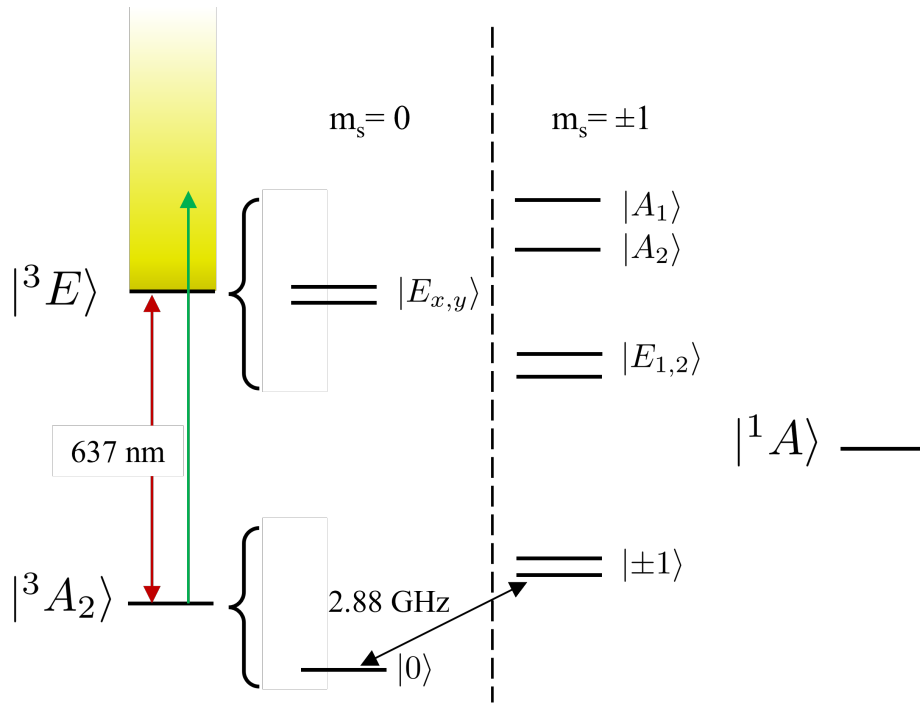
FIGURE 2.3. Energy level diagram of the NV's ground and excited state. The state furthest right is the meta-stable singlet.

stronger transitions are characterized by the spin character of the initial state from which they are excited, e.g. linearly polarized light ($\hat{x}$ and $\hat{y}$) primarily excites the $|E_x\rangle$ and $|E_y\rangle$ transitions from $|0\rangle$ with decay pathways that result in the same spin character. A table of transitions and their selection rules are shown in Table 2.1. Exciting the NV non-resonantly is also spin dependant. Non-resonant excitation while in the electron is initially in the $m_s = 0$ ground spin state radiatively cycles the electron between triplet configurations in the excited and ground state. If the electron is initially in the $m_s = \pm 1$ spin state, after non-resonant excitation, the electron will preferentially decay non-radiatively via the intersystem crossing (ISC) to the meta-stable singlet state (Figure 2.3) before decaying to any of the spin ground states. Repeated cycling via non-radiative excitation, therefore can optically pump the NV into the $|0\rangle$ state. This is an

important feature of the NV useful for initialization and readout which occurs at room and cryogenic temperatures. Continuous resonant excitation can ionize the NV to it's neutral charge state. Recovery of the negative charge can be achieved via off-resonant excitation [44].

Initial State	$|E_x\rangle$	$|E_y\rangle$	$|E_1\rangle$	$|E_2\rangle$	$|A_1\rangle$	$|A_2\rangle$
$|-1\rangle$			σ_+	σ_+	σ_-	σ_-
$|0\rangle$	$\hat{x}$	$\hat{y}$				
$|+1\rangle$			σ_+	σ_+	σ_-	σ_-

TABLE 2.1. Polarization of light needed for transitions between initial states and final excited states where $\sigma_{+,-}$ represents right and left handed circularly polarized light respectively and $\hat{x}$, $\hat{y}$ are x- and y-linearly polarized light.

2.4. Strain

Crystallographic defects caused by interruptions in the crystalline structure or composition of the diamond exert external forces on the NV. One of these effects is localized strain which we describe with the strain Hamiltonian, $\hat{H}_{Strain}$. Strain effects on the excited state energy levels can be described by two parameters, $\delta_{1,2}$. One of which systematically alters the band structure altering the exact ZPL. The other splits the orbital doublet states and introduces cross terms between the various excited state energy levels which is referred to as state-mixing. State-mixing complicates the selection rules of exciting the NV to the excited state, allowing previously forbidden transitions to occur. The resulting Hamiltonian can be written as a sum of each contribution, $H = H_{so} + H_{ss} + H_{Strain}$,

which can be written in the basis states $\{|A_1\rangle, |A_2\rangle, |E_x\rangle, |E_y\rangle, |E_1\rangle, |E_2\rangle\}$ as

$$\hat{H} = \begin{pmatrix} \Delta - \Delta' + \lambda_z & 0 & 0 & 0 & \delta_1 & -i\delta_2 \\ 0 & \Delta + \Delta' + \lambda_z & 0 & 0 & i\delta_2 & -\delta_1 \\ 0 & 0 & -2\Delta + \delta_1 & \delta_2 & 0 & i\Delta'' \\ 0 & 0 & \delta_2 & -2\Delta - \delta_1 & \Delta'' & 0 \\ \delta_1 & i\delta_2 & 0 & \Delta'' & \Delta - \lambda_z & 0 \\ i\delta_2 & -\delta_1 & i\Delta & 0 & 0 & \Delta - \lambda_z \end{pmatrix} \tag{2.4}$$

Figure 2.4 shows the shift in the unperturbed excited states of the NV center as a function of δ_1. Transitions with $m_s = 0$ are linearly split, this is a key feature for determining a given NV center's strain environment. Looking closer, notice that there exists a level anti-crossing around 7 GHz between the E_y and E_1 states. Excitation of the NV center with a strain parameter near this regime allows for optical electronic spin-flip transitions [46]. This is due to state mixing between the $m_s = 0$ spin character excited state E_y and the nonzero spin states $E_{1,2}$, also be seen in the cross terms of Eq 2.4. These spin-flip transitions will be a vital part of the experiments discussed in Chapter VII.

2.5. ^{13}C Nuclear Spin Bath

An additional defect found in the diamond host is the ^{13}C isotope. The defect, also referred to as a P1 center, has a net nuclear spin $I = 1/2$, with a typically low abundance in diamond (1.1%) [14]. While considered low, this abundance accumulates to a "^{13}C nuclear spin bath" which creates a time-varying magnetic field, which results in a shift of the non-zero electronic spin states of the NV center. This is the primary source of decoherence of the NV limiting

16
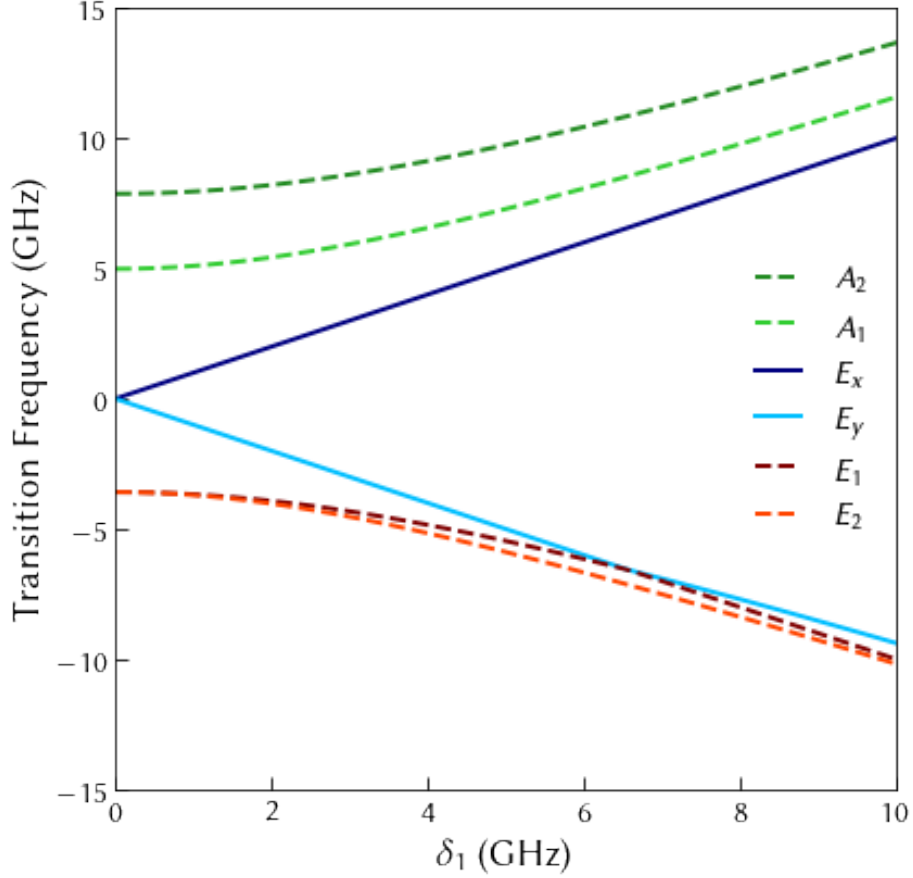
FIGURE 2.4. A plot of transition energy with respect to the unperturbed $E_{x,y}$ excited state with respect to strain parameter δ_1. Dashed lines indicate non-zero spin character

its electronic spin coherence time, T_2, from milliseconds to a few microseconds [47, 48]. The concentration of ^{13}C changes from sample to sample and even within the same sample. The isotope can be eliminated altogether in isotopically pure samples [11, 43, 49]. On the other hand, nearby ^{13}C couple strongly to the NV and feature very long coherence times exceeding one second [50]. These spins can be individually addressed via the hyperfine interaction with the NV center [48, 51, 52, 53].

The nuclear spin bath plays a role in this dissertation as the model fluctuating magnetic environment. As it will be discussed in detail further in

Chapter V, we treat the nuclear spin bath as an Ornstein-Uhlenbeck (OU) process. The OU process is a commonly used stochastic process that is both Markovian and normally distributed. The process features a memory time, which encompasses the potential dynamics of the ^{13}C spin bath [54, 55, 56]. In the following chapters we lay out the process taken to develop and test our quantum sensor which captures the real-time dynamics of a time-varying magnetic field in the hopes that it can inform the dynamics of the spin bath.

CHAPTER III

EXPERIMENTAL METHODS

The following sections describe the experimental setup and various methods frequently employed for locating the NV and its atomic transitions, controlling the ground state electron spin, and determining environmental parameters.

3.1. Experimental Setup

The experiments discussed in this dissertation were carried out using a home-built confocal microscopy setup whose schematic is shown in Figure 3.1. The NV center is optically addressed through a high power objective lens (Nikon L Plan 100x/0.85 NA) focused just below the diamond surface. The beam's position on the diamond can be controlled via a remote computer using a 2D - Galvanometer or "galvo" (Thorlabs). The red fluorescence from the NV center is collected using the same objective. The collection path runs counter to the excitation path to a dichroic mirror through which its fluorescence is transmitted. Scattered and reflected excitation light is then filtered out using a 637 nm notch filter and a 150 nm bandpass filter centered at 750 nm limiting the collected photons to those emitted from the NV's phononic sideband. The filtered light is then launched into an optical fiber with a core diameter of 10 μm, which acts as our confocal pinhole and sets the resolution of the confocal image. The collection fiber is then coupled to a Perkin Elmer SPCM-AQR-16-FC Avalanche Photodiode (APD) which outputs a TTL pulse for each detected photon. Single photon counting is achieved through a photon counting card (National Instruments, PCI 6602).
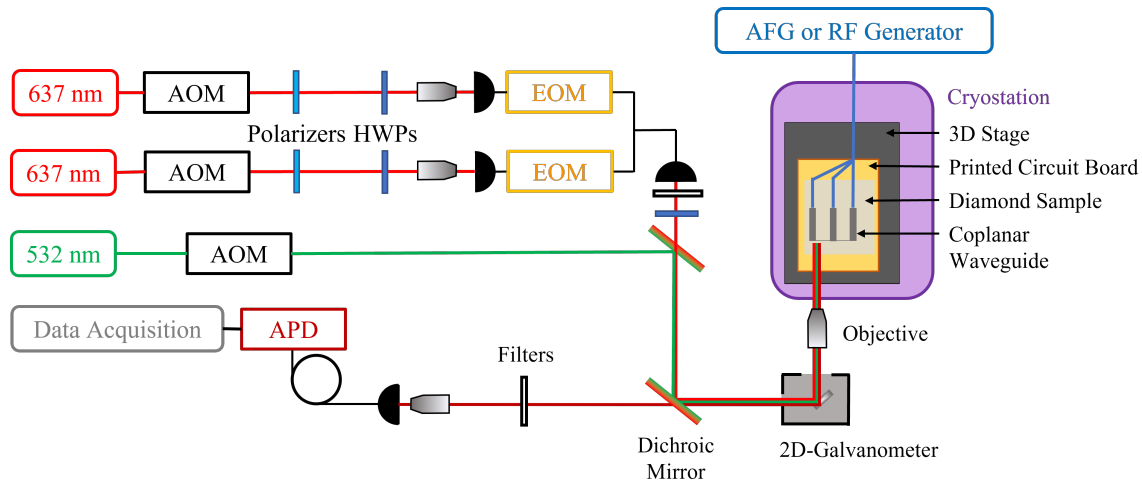
FIGURE 3.1. Schematic of the experimental setup. Initialization and coherent population trapping beams are generated from 532 nm (green) and 637 nm (red) lasers combined and focused onto an NV located in the diamond sample. Fluorescence from the NV (maroon) works back through the excitation path, transmitting through a dichroic mirror and filtered before being sent to an avalanche photodiode (APD) detector.

Non-resonant excitation used for initializing the NV to its negative charge state and optically pumping electron population to the $m_s = 0$ ground state is achieved using laser light generated by a Laser Flow Technologies 532 nm (green) laser (LCS-0532-TFC-0050-05). This beam is switched on and off using an IsoMet acousto-optic modulator (AOM) which is driven by a pulse modulated IsoMet AO Driver 525C-L. Resonant excitation is achieved using tunable 637 nm (red) diode lasers (New Focus TLB-6700) whose beams are pulsed using a pair of Gooch and Housego R15210 AOMs. Additional optical sidebands are generated using fiber coupled electro-optical phase modulators or EOMs (Jenoptic and EOSpace). The red beams are combined in a polarization maintaining fiber. At the output is a half-wave plate used to rotate the polarization of the beam to meet selection rule criteria set by the resonant transitions. Green and red beams are combined in

free space using a Semrock Di02R594 dichroic mirror before reflecting off a second dichroic mirror (Semrock Di02R 635) and entering the galvo.

In order to resolve the excited states of the NV, all experiments that follow are run at cryogenic temperatures. The sample is mounted our on the cold finger of a closed-cycle optical cryostation (from Montana Instruments, Inc) which cools it down to temperatures as low as 8 K. Coarse positioning of the sample occurs within the cryostation thanks to three stacked attocubes, one for each Cartesian direction. In order to accommodate the low-working-distance of our objective a thin window (1mm) through which we can focus the excitation beam onto the NV is installed.

The diamond sample used for all experiments is a type IIa electronic grade chemical-vapor-deposition grown diamond (from Element Six, Inc.). Due to the high index of refraction of our defect's host material ($n_{Diamond} = 2.42$) much of the fluorescence from the NV is totally internally reflected (Figure 3.2a) lowering the effective numerical aperture (NA) of our objective. To enhance the collected fluorescence a solid immersion lens (SIL) with dimensions matching the NA of our objective is milled into the surface of the diamond sample using a focused ion beam (FIB) [57](Figure 3.2b).

DC current and microwave (MW) radiation can be applied to the NV using a coplanar waveguide (CPW) fabricated on the surface of the diamond. The aluminum waveguide is deposited and shaped using laser-writer before development with photolithography. The waveguide is wirebonded to a printed circuit board (PCB) which is wired to an input outside the cryostation. An RF generator is used as a MW source for NV ground state control described in the following sections. The MW signal is amplified by a Mini-Circuits ZHL-16W-43-

(a)

$n_0 = 1$
$n_{diamond} = 2.42$
$\theta_{TIR} = 24.4°$
$\theta_{NA} = 64°$
NV

(b)

10 µm

(c)
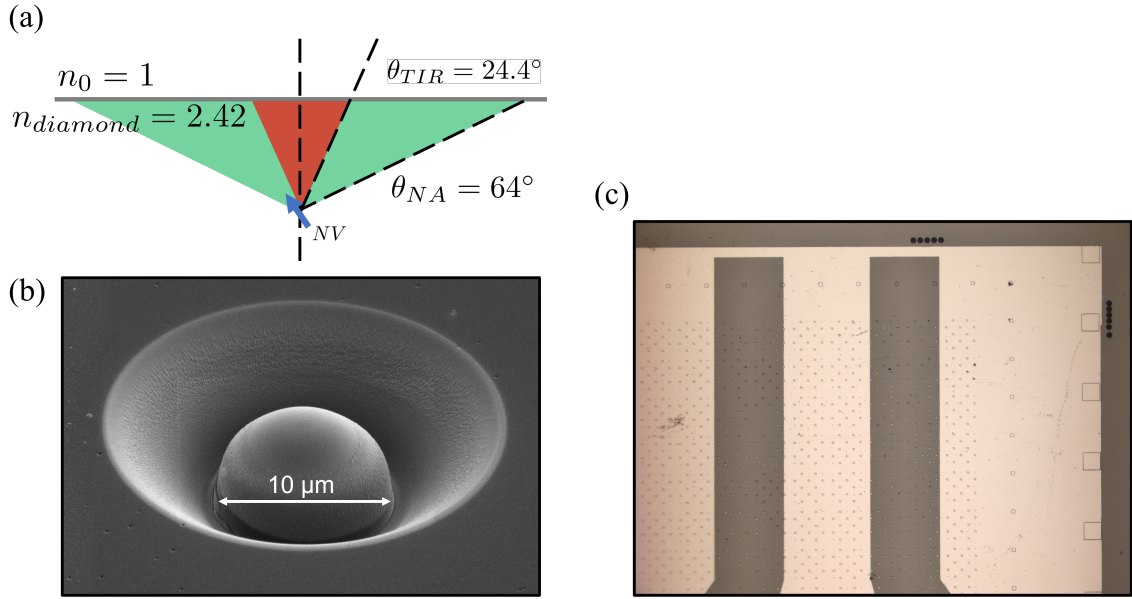
FIGURE 3.2. (a) Schematic of the total internal reflection (red) due to the high index of refraction of diamond while the acceptance angle determined by the NA of our objective is much larger (green). (b) A scanning electon microscope image of our SIL which is approximately 10 μm in diameter and enhances the NV's fluorescence by a factor of approximately 5. (c) Pictures of the diamond sample with the deposited aluminum coplanar waveguide (white) and several FIB milled SILs (top, black).

S+ amplifier. A Tektronics arbitrary function generator (AFG30523) is used as a magnetic fluctuation source for real-time magnetometry experiments.

To achieve the Zeeman splitting needed for individual ground state spin control a permanent magnet is mounted outside of the cryostation and oriented along the NV's quantization axis. A pulse generator (Spin Core, PulseBlaster ESR-PRO-400) is used to control pulse duration and synchronization of laser and microwave pulses, photon collection, and real-time estimation procedures discussed in later chapters.
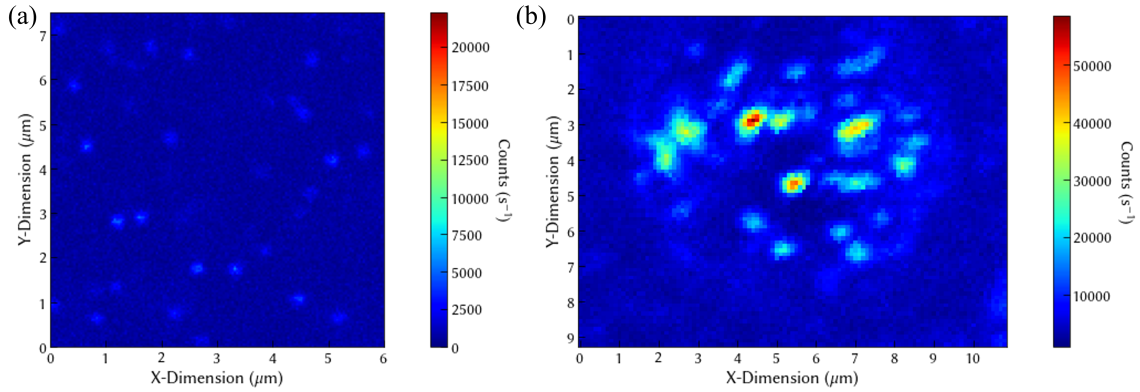
FIGURE 3.3. (a) Photoluminecent (PL) map of NV centers in the diamond bulk. (b) PL map of a SIL. Both images were taken while illuminated with 1 mW of 532 nm laser light.

3.2. Imaging the NV

Confocal imaging is necessary to locate and target the NV center with an imaging resolution of <1 μm in the x, y, and z - dimensions. To locate the NV, a photoluminescence (PL) map is generated at the focal point of the objective lens. PL maps are created by continuously radiating the sample with 532 nm laser light as the beam is rastored across the diamond surface. Fluorescence is collected for each galvo position, thereby mapping corresponding fluorescence levels onto a 2D image as seen in Figure 3.3.

Comparing the bulk PL map in Figure 3.3a with that of the SIL in Figure 3.3b we can see the enhanced fluorescence gained when using a SIL. The edge of the SIL can be identified in the image as a ring that surrounds multiple bright red spots. The NV chosen for all of the experiments described is located at the map coordinates (5.5, 4.5) μm. This NV was chosen because of its relatively high fluorescence, low surrounding background fluorescence and excited state strain splitting.

3.3. Photoluminescent Excitation

As mentioned previously, the NV center ground state is separated from the excited state by a ZPL located near 637 nm. Tuning a laser across this wavelength at low temperatures drives each of the various excited state transitions [46]. MWs tuned to the NV's ground state zero-field splitting of 2.87 GHz cycles the ground state spin projection between the $m_s = 0$, and ± 1 spin sublevels. This results in the spectra of excited state transitions observed in Figure 3.4b. It is important to notice that some of the "forbidden" transitions can be observed as well such as the $|0\rangle \rightarrow |E_{1,2}\rangle$. This is due to the existence of transverse strain within the NV's environment. The strain component can be determined by measuring the splitting between the $|0\rangle \rightarrow |E_y\rangle$ and $|0\rangle \rightarrow |E_x\rangle$ transitions, which are typically the brightest spectral transitions. The NV in our study has a strain splitting of approximately 4 GHz. The relative spectral location of the other transitions are consistent with the theoretical predictions shown in Figure 2.4.

Continuous resonant excitation for longer durations can cause the NV to ionize, resulting in the neutral NV which has a different ZPL. Therefore periodic green pulses must be added to the pulse sequence in order to reinitialize the NV into its desired charge state. The intrinsic linewidth of the NV center is 13 MHz [58]. A closer look at the $|0\rangle \rightarrow |E_y\rangle$ transition in Figure 3.3c shows a broadened Lorentzian resonance with a spectral linewidth of approximately 300 MHz. Spectral broadening is caused by many factors including diffusion within the host material, temperature, and power broadening among others.

By applying continuous resonant excitation at smaller time scales we observe optical pumping due to state mixing. We can investigate the effects of optical pumping by recording the number of photon counts we get relative to the start of
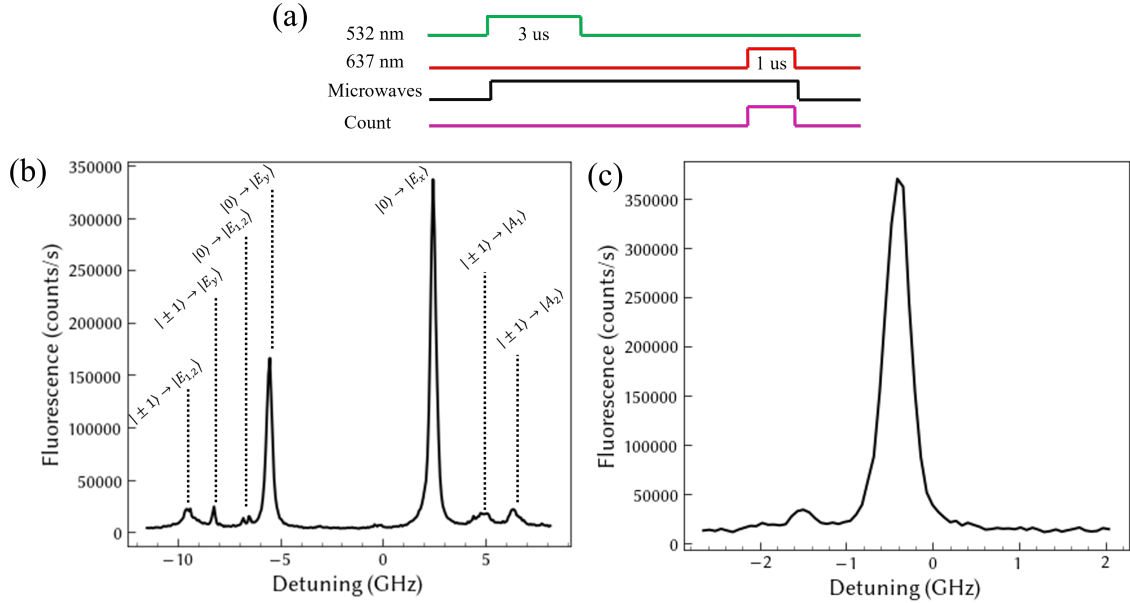
FIGURE 3.4. (a)Pulse sequence for spectrum (b) & (c) uses a green, 532 nm, initialization pulse of 3 μs to initialize the NV in the $m_s = 0$ ground spin state. Microwaves are applied to cycle the ground state spin sublevel population before being readout using a detuned red 637 nm laser. (b). PLE spectrum of all NV excited state transitions due to microwave cycling of ground state spin sublevels and state mixing within the excited state. (c) Zoomed in spectra of the $|0\rangle \rightarrow |E_y\rangle$ transition. The spectral linewidth is broadened to 300 MHz.

the excitation pulse. Figure 3.5 shows the effect of optical pumping at two optical powers while the laser is tuned to the $|0\rangle \rightarrow |E_y\rangle$ transition.

Due to state mixing caused by axial strain, with each excitation there is a probability that decay from the excited state can result in a different spin projection. Therefore after repeated excitations the population of the $m_s = 0$ sublevel decays. Comparing the powers in Figure 3.5, we see a slower decay corresponding to low powers due to lower driving frequencies and faster decays at higher powers. These transitions can be utilized for readout of the ground state spin population with a detection window corresponding to the decay speed.
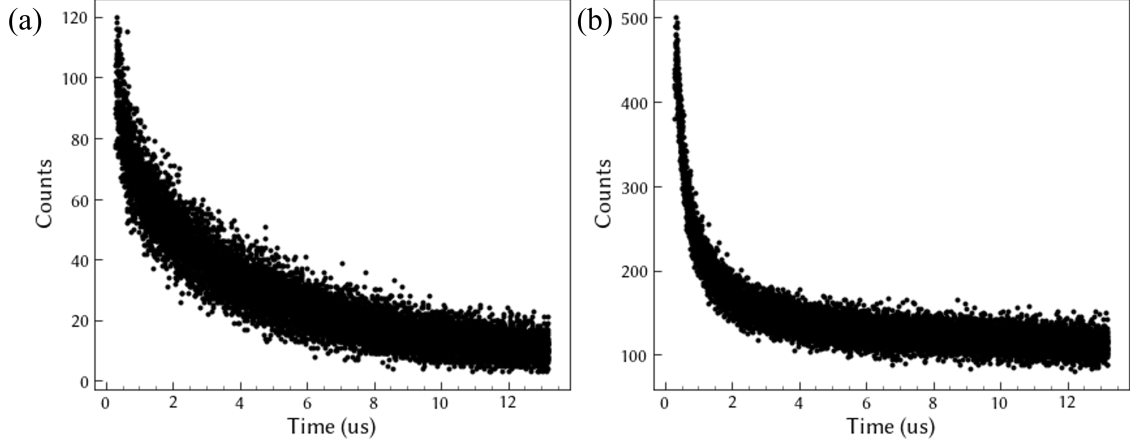
FIGURE 3.5. **(a)** & **(b)** Time resolved PLE of the $|0\rangle \rightarrow |E_y\rangle$ transition while being illuminated by 340 nW and 106 μW of 637 optical power respectively. The rate at which the fluorescence decays determines the optimal detection window for PLE. Photoionization, and optical pumping into different spin sublevels are responsible for the decay.

3.4. NV Ground State Control

3.4.1. Optically Detected Magnetic Resonance

Optically detected magnetic resonance or ODMR utilizes fluorescence from PLE readout to detect a change in the population of ground state $m_s = 0$ spin sublevel. The pulse sequence used for ODMR measurement is shown in figure 3.6a, beginning with a 3 μs green pulse, initializing the spin population to $|0\rangle$. Then the NV is radiated with microwaves for a specified duration before readout of the $m_s = 0$ population using the $|0\rangle \rightarrow |E_y\rangle$ transition. This sequence is repeated as the microwave frequency is swept. In Figure 3.6b we see the zero-field resonance located at 2.87 GHz, demonstrating a transfer in population from the $m_s = 0$ to the $m_s = \pm 1$ spin sublevel. Inserting a permanent magnet along the NV's axis we can split the $m_s = \pm 1$ levels seen in Figure 3.6c. We can maximize the population

transferred in ODMR by pulsing the microwaves with a duration equal to a π-rotation of the spin state described in the next section.
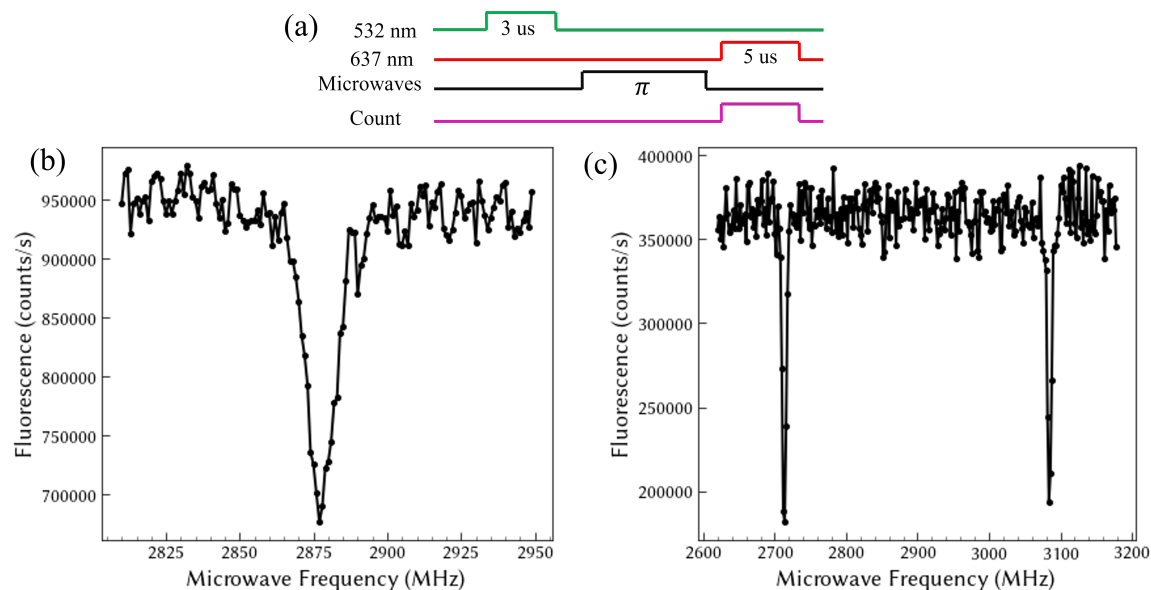
FIGURE 3.6. **(a)** Pulse sequence for pulsed ODMR uses a microwave π-pulse to maximize signal contrast. **(b)** Pulsed ODMR of the zero-field ground state sublevel resonance. A π-pulse duration of 300 ns transfers the spin population in the ground state from $m_s = 0$ to $m_s = \pm 1$. Readout using the $m_s = 0 \rightarrow |E_y\rangle$ on resonance exhibits a dip in fluorescence due to the transfer of spin population. **(c)** In the presence of a magnetic field oriented along the NV axis we see Zeeman splitting of 290 MHz between the $m_s = \pm 1$ spin sublevels.

Looking closer at the $|0\rangle \rightarrow |+1\rangle$ transition we can probe the MW power dependence. In Figure 3.7b we see that at low powers we can resolve the hyperfine interaction between the NV's electron spin and the nuclear spin associated with the ^{14}N isostope. Since the total nuclear spin of ^{14}N is $I = 1$ the possible spin projections are $m_I = 0$, and ± 1. Each of these transitions are observed here with the expected hyperfine splitting of 2.2 MHz. As power is increased, we see the effects of power broadening (Figure 3.7a).
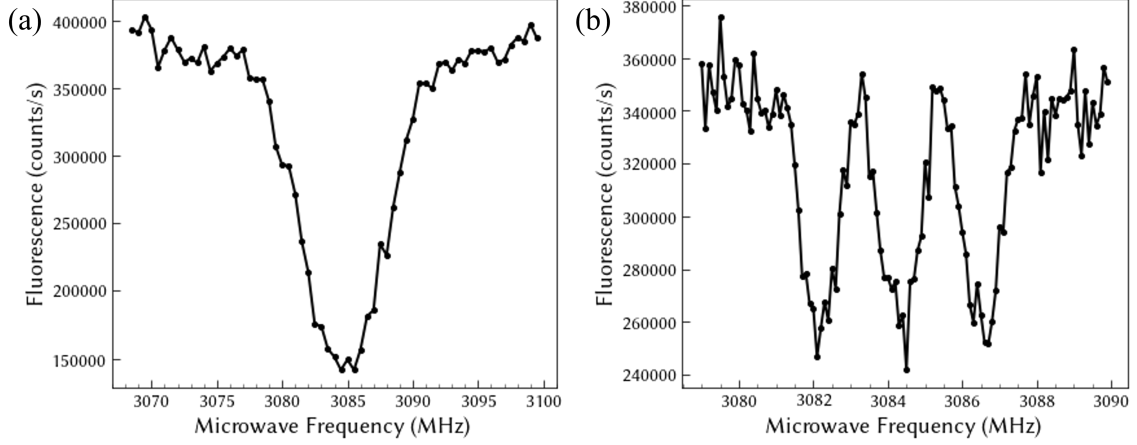
FIGURE 3.7. Pulsed ODMR of the $m_s = 0$ to $m_s = +1$ microwave transition. **(a)** At high power the transition becomes power broadened. **(b)** At lower powers we can resolve the individual nuclear spin transitions.

3.4.2. Rabi Oscillations

Observing the effects of ODMR in the temporal domain reveals Rabi oscillations, corresponding to the electron population transfer within the spin sublevels of the ground state. This is carried out using the pulse sequence shown in Figure 3.8a which starts with green initialization followed by a microwave pulse with duration τ. Electronic population in the $m_s = 0$ state is readout by pulsing our red laser while tuned to the $|0\rangle \rightarrow |E_y\rangle$ transition. Incrementally increasing τ while recording the observed fluorescence we can see coherent oscillations (Figure 3.8c) corresponding to a transfer between $m_s = 0$ and $m_s = +1$. Increasing the power of our MW pulse we see the frequency of these oscillations increase (Figure 3.8d). Figures 3.8c & d are fit using a sinusoidal curve with a Rabi frequency (Ω_0). The Rabi frequency linearly follows the square root of the applied microwave power (Figure 3.8b).

Zooming out in time, as in Figure 3.9, the amplitude of Rabi oscillations appears to oscillate as well. This can be attributed to the various hyperfine

28
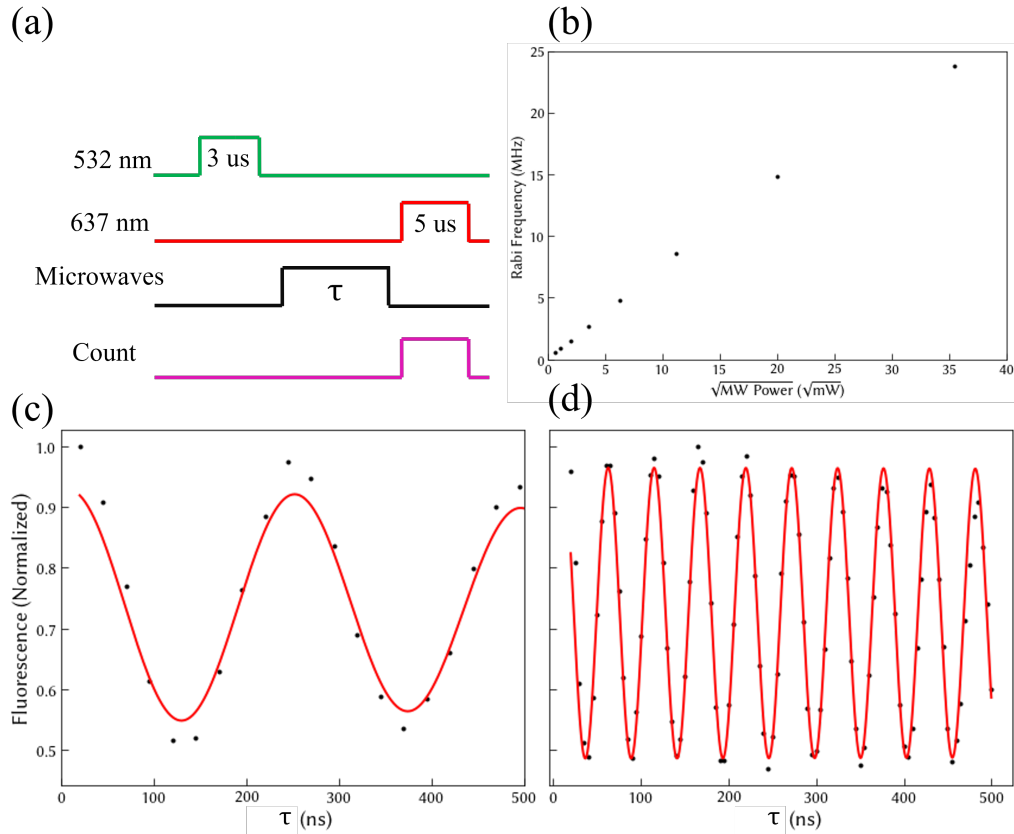
FIGURE 3.8. **(a)** Pulse sequence for observing Rabi oscillations. **(b)** Rabi frequency dependence as a function of the square root of MW power reveals a linear trend. **(c)** & **(d)** Rabi oscillations at relatively low and high powers are fit with a sinusoidal curve.

transitions within a given electronic transition. Rabi oscillations corresponding to each m_I state are each slightly detuned. The data in Figure 3.9 is fit with the sum of three sinusoidals with frequencies Ω_0 and $\Omega = \sqrt{\Omega_0^2 + (\pm 2.2\text{MHz})^2}$ with amplitudes A and $A \times \Omega_0/\Omega$ respectively, where Ω is the generalized Rabi frequency and ± 2.2 MHz corresponds to the detuning from the other two hyperfine transitions. Each hyperfine transition can be driven separately at low MW powers where each hyperfine resonance is individually resolved (Figure 3.7b).
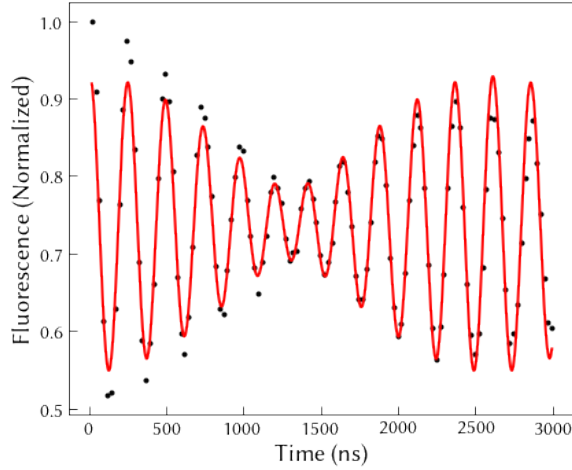
FIGURE 3.9. Rabi oscillations observed for longer times reveals the effect of the hyperfine transitions which cause beats in the Rabi oscillation's amplitude.

3.4.3. Ramsey Fringes

Ramsey fringe interferometry allows for us to measure the accumulated phase between quantum states. The pulse sequence used for Ramsey interferometry uses the now familiar initialization and readout pulse with a different MW control sequence in between (Figure 3.10a). For this sequence we start with a $\pi/2$ pulse which places the NV in an equal superposition between the $m_s = 0$ and $m_s = +1$ or -1 state. The NV is then allowed to freely presses for a duration τ, allowing for phase to accumulate between the two states. The spin is then rotated by another $\pi/2$- pulse before being readout. Varying the duration of τ results in the fringe pattern seen in Figure 3.10b & c.

The data shown in Figures 3.10b & c are fit with the sum of three sinusoids corresponding to each hyperfine transition. Each sinusoid is has a frequency of δ and $\delta \pm 2.2$MHz where δ is the MW detuning from the central hyperfine resonance. Consequentially, the oscillations get much faster at higher δ as shown in Figure 3.10c. The interferometric pattern is however limited by the spin-coherence
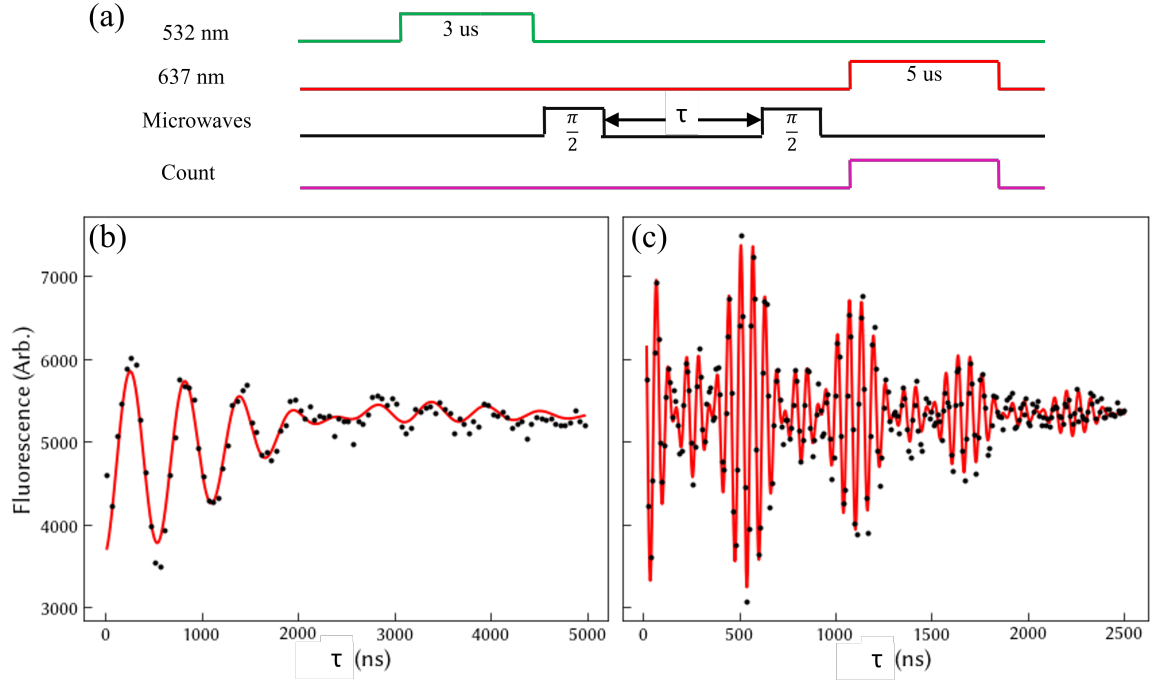
FIGURE 3.10. **(a)** Pulse sequence used for Ramsey fringe interferometry. **(b)** Ramsey fringes at zero detuning from the central hyperfine resonance with a $\pi/2$-pulse of 25 ns. The beating pattern observed is due to the detuning from the adjacent hyperfine transitions. **(c)** Ramsey fringes at a large detuning of 30 MHz from the central resonance results in faster oscillations.

time of the NV center. Therefore the sinusoidal fit is multiplied by a Gaussian envelope, $e^{-(\tau/T_2^*)^2}$, where T_2^* is the spin dephasing time. The dephasing time is the amount of time that it takes for the $m_s = 0$ and $m_s = +1$ states to accumulate random phase. The fits in Figure 3.10b & c indicate that our NV has a $T_2^* = (2.04 \pm 0.15)\mu$s. The dephasing is due to decoherence sources near the NV which is primarily attributed to ^{13}C nuclear spins. Decoherence times of up to 1.3 ms have been found in isotopically purified samples of diamond [11].

3.5. Summary

With the use of confocal microscopy we gain access to the NV within the diamond host, allowing us to optically initialize, and readout the electronic, and hyperfine state of the NV. MW control lets us control the NV center's ground spin states which opens up a host of applications such as Ramsey interferometry and real-time magnetometry and feedback as discussed later. Cooling the NV down to cryogenic temperatures allows us to investigate the NV center's excited state and useful for applications such as CPT and nuclear spin pumping.

CHAPTER IV

COHERENT POPULATION TRAPPING

Content in this chapter was written as supplemental material for a paper coauthored by Shuhao Wu and Hailin Wang [59]. All experiments discussed were performed by the author.

CPT acts as a very sensitive probe for measuring the effects of external fields on the NV's electronic structure, particularly magnetic fields. While ground state control such as ODMR and Ramsey fringes are one way to do this, CPT enables an optical alternative to such sensing enabling the ability to address individual defects with micron resolution [60]. This chapter contains discussion about the theoretical background for CPT, various experimental approaches and uses for CPT as well as how CPT is realized using the NV. In this chapter we also see that the hyperfine structure of the NV can also be probed.

4.1. Theory

CPT can be realized with the Λ-type three-level system shown in Figure 4.1. This system consists of two lower states, $|-\rangle$ and $|+\rangle$, which couple to an excited state, $|e\rangle$ via two respective dipole optical transitions. For a CPT process, the two transitions are driven by two resonant or nearly resonant laser fields with transition frequencies ω_- and ω_+ as well as Rabi frequencies, Ω_- and Ω_+, respectively. When the two laser fields are Raman-resonant with the two lower states, the interaction Hamiltonian of the system in the rotating frame becomes

$$\hat{H} = \frac{\hbar}{2}(\Omega_- |-\rangle \langle e| + \Omega_+ |+\rangle \langle e|) + h.c. \qquad (4.1)$$
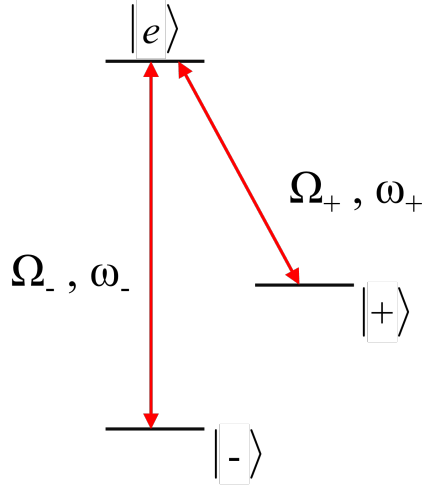
FIGURE 4.1. Schematic of a generic Λ-type three level system for CPT.

This Hamiltonian features an eigenstate given by,

$$|D\rangle = \frac{1}{\sqrt{\Omega_+^2 + \Omega_-^2}}(\Omega_- |+\rangle - \Omega_+ |-\rangle). \tag{4.2}$$

$|D\rangle$ is a special superposition of the two lower states. Since the transition coefficient, $\langle e| \hat{H} |D\rangle = 0$, an electron in this superposition state will remain trapped in this state preventing optical emissions from the excited state in spite of the resonant dipole optical coupling. In this context, $|D\rangle$ is a dark state [61]. This occurs due to the destructive quantum interference caused by the superposition of the two transitions. Detuning between one of the two transitions determines how much fluorescence is observed. This is the guiding principle of our sensing apparatus that allows us to do real-time magnetometry discussed in Chapter V. Note that if the system is not initially in $|D\rangle$, it can be pumped into $|D\rangle$ via a few cycles of optical excitation and subsequent spontaneous emission [62].

We discuss the expected spectral response to be observed in experiment by first considering the wave function of the system in a rotating frame which can be

written as

$$|\Psi\rangle = \tilde{C}_e \, |e\rangle + \tilde{C}_+ \exp\left(i\omega_+ t\right) |+\rangle + \tilde{C}_- \exp\left(i\omega_- t\right) |-\rangle \tag{4.3}$$

The density matric elements in this rotating frame are defined as $\rho_{ij} = \langle \tilde{C}_i \tilde{C}_j^{\;*}\rangle$. The corresponding density matrix equations are then given by

$$\dot{\rho}_{e+} = -(i\Delta_+ + \gamma)\rho_{e+} + \frac{i\Omega_+}{2}(\rho_{ee} - \rho_{++}) - \frac{i\Omega_-}{2}\rho_{-+} \tag{4.4}$$

$$\dot{\rho}_{e-} = -(i\Delta_- + \gamma)\rho_{e-} + \frac{i\Omega_-}{2}(\rho_{ee} - \rho_{--}) - \frac{i\Omega_+}{2}\rho_{+-} \tag{4.5}$$

$$\dot{\rho}_{-+} = -[i(\delta - \omega_B) + \gamma_s]\rho_{-+} + \frac{i\Omega_+}{2}\rho_{-e} - \frac{i\Omega_-}{2}\rho_{e+} \tag{4.6}$$

$$\dot{\rho}_{ee} = -\Gamma\rho_{ee} + (\frac{i\Omega_+}{2}\rho_{e+} + c.c.) + (\frac{i\Omega_-}{2}\rho_{e-} + c.c.) \tag{4.7}$$

where γ_s and γ are the decay rates for the spin coherence and optical dipole coherence respectively, Γ is the decay rate fro the excited state population, $\Delta_- = \omega_{opt} - \omega_-$, $\Delta_+ = \omega_{opt} - \omega_+$, with ω_{opt} and ω_B being the frequency separation between states $|e\rangle$ and $|-\rangle$ and between states $|+\rangle$ and $|-\rangle$, respectively. For our experiments, $\gamma_s << (\gamma, \Gamma)$ and $\Omega_+ \approx \Omega_-$. Note that textbook treatment of CPT typically assumes $\Omega_+ << \Omega_-$, with the electron initially in the state $|+\rangle$.

With $\gamma_s << (\gamma, \Gamma, \rho_{ee})$ and the optical dipole coherences characterized by ρ_{e+} and ρ_{e-} can reach steady state in a timescale much faster than that for the spin coherence characterized by ρ_{-+}. In this limit, ρ_{e+} and ρ_{e-} as well as the diagonal matrix element follow adiabatically the dynamics of ρ_{-+}, with

$$\rho_{e+} = -\frac{i}{2\gamma}(\Omega_+ N_+ - \Omega_- \rho_{-+}) \tag{4.8}$$

$$\rho_{e-} = -\frac{-}{2\gamma}(\Omega_- N_- + \Omega_+ \rho_{+-}) \tag{4.9}$$

where $N_\pm = \rho_{\pm\pm} - \rho_{ee}$ is the population difference between lower and upper states. For simplicity, we have also assumed $|\Delta_\pm| << \gamma$ and have thus set $\Delta_\pm = 0$ for Eq. 4.8 and 4.9. The steady-states excited state population is then given by

$$\rho_{ee} = \frac{1}{2\Gamma\gamma}[(\Omega_+^2 N_+ + \Omega_-^2 N_-) + 2\Omega_+\Omega_- Re(\rho_{-+})]. \qquad (4.10)$$

The CPT-induced dip in the excited state population is determined by the real part of ρ_{-+}.

Using Eq. 4.8 and 4.9, we arrive at the equation of motion for the spin coherence

$$\rho_{-+} = -[i(\delta - \omega_B) + \gamma_s + \frac{\Omega_+^2 + \Omega_-^2}{4\gamma}]\rho_{-+} - \frac{\Omega_+\Omega_-}{4\gamma}(N_+ + N_-) \qquad (4.11)$$

The $\Omega_\pm/4\gamma$ terms in Eq. 4.11 correspond to the power broadening of the optically-driven spin transition and thus the power broadening of the CPT resonance. The steady-state solution of ρ_{-+} is given by

$$\rho_{-+} = -\frac{\Omega_+\Omega_-}{4\gamma}\frac{N}{i(\delta - \omega_B) + \gamma_S + (\Omega_+^2 + \Omega_-^2)/4\gamma}, \qquad (4.12)$$

where $N = N_+ + N_-$. For $\rho_{ee} << 1$, N can be approximated as the total population in the who lower states, n. In the limit of equal Rabi frequencies for the two optical fields, $\Omega_+ = \Omega_- = \Omega_0$, the excited state population is then given by

$$\rho_{ee} = \frac{\Omega_0^2 n}{2\Gamma\gamma}[1 - \frac{\Omega_0^2}{2\gamma}\frac{\gamma_s + \Omega_0^2/2\gamma}{(\delta - \omega_B)^2 + (\gamma_s + \Omega_0^2/2\gamma)^2}]. \qquad (4.13)$$

Strong suppression of the excited state population occurs when $\Omega_0^2 >> 2\gamma\gamma_s$ and the two incident optical fields are Raman resonant with the three-level system.

Note that even when the system is initially prepared in a given lower state, with $\Omega_+ = \Omega_-$ optical excitations can quickly equalize the population in the two lower states.

4.2. Experiment

Observation of electromagnetically induced transparency (EIT) was first observed using NV centers in 1999 using MW transitions in the ground state [63]. CPT has been performed in a variety of Λ-type systems using optically allowed transitions of the NV [64][65][66]. Figure 4.2a shows the Λ-type three-level system used in our experiments for the CPT process. The $|0\rangle$ to $|E_y\rangle$ transition is allowed due to the natural spin character of $|E_y\rangle$. Due to the high strain environment of our NV, we have sufficient state mixing for the $|+1\rangle$ to $|E_y\rangle$ transition, which is otherwise dipole-forbidden, to be dipole-allowed.

To obtain the CPT spectral response, we must first split the $m_s = \pm 1$ electron sublevels using a permanent magnet along the NV axis. The $|+1\rangle$ to $|E_y\rangle$ transition is located using PLE while microwaves are on (Figure 3.4). While tuned to this transition, the EOM shown in Figure 3.1 is modulated by an external RF source whose frequency generates a sideband off of the pump laser. The sideband frequency is swept across the separation between the $|0\rangle$ and $|+1\rangle$ sublevels. Figure 4.2b shows a full CPT spectral response at the resonance of the $|0\rangle$ to $|E_y\rangle$ transition. CPT and the corresponding quenching of the fluorescence occur when the detuning between two laser fields approaches the frequency separation between the two lower states. A close-up of a CPT dip is displayed in Figure 4.3c.

A Lorentzian least-square fit to the CPT dip in Figure 4.2c yields a CPT linewidth of 11.6 MHz. Contributions to this linewidth include the spin
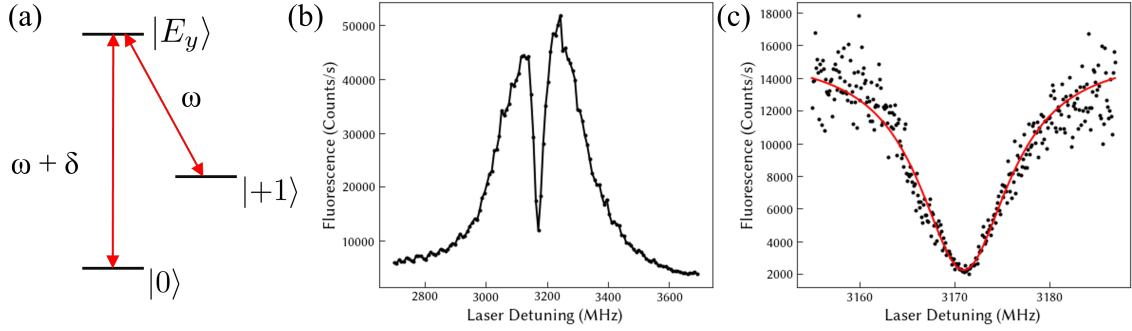
FIGURE 4.2. **(a)** The Λ-type three-level system used in the real-time sensing. **(b)** A full CPT spectral response occurring at the resonance of the $|0\rangle$ to $|E_y\rangle$ transition. **(c)** A closer look at a CPT dip obtained under experimental conditions used for real-time sensing. The red line is a least-square fit to an inverted Lorentzian.

dephasing induced by the nuclear spin bath, the hyperfine splitting, and the power broadening. The hyperfine splitting is 2.2 MHz. The linewidth due to the spin dephasing is 0.6 MHz, as determined from a separate ODMR experiment. To estimate the power broadening, we numerically fit the CPT dip with a sum of three inverted Lorentzians with the same linewidths and with 2.2 MHz hyperfine splitting between adjacent Lorentzians [67]. The numerical fit yields a power broadening of 4.7 MHz. Using the expression given in Golter et. al. ([68], supplementary information) on the power broadening contribution to the CPT resonance, we estimate the Rabi frequency for the optical fields to be of order 5 MHz.

To resolve the individual hyperfine contributions of the ^{14}N nuclear spin we employ the same Λ-type three level system on each nuclear spin (Figure 4.3a). Lowering the power of the two applied fields reduces the power broadening and each CPT response. Figure 4.3b shows the three individual CPT-dips at a carrier power of approximately 50 nW .
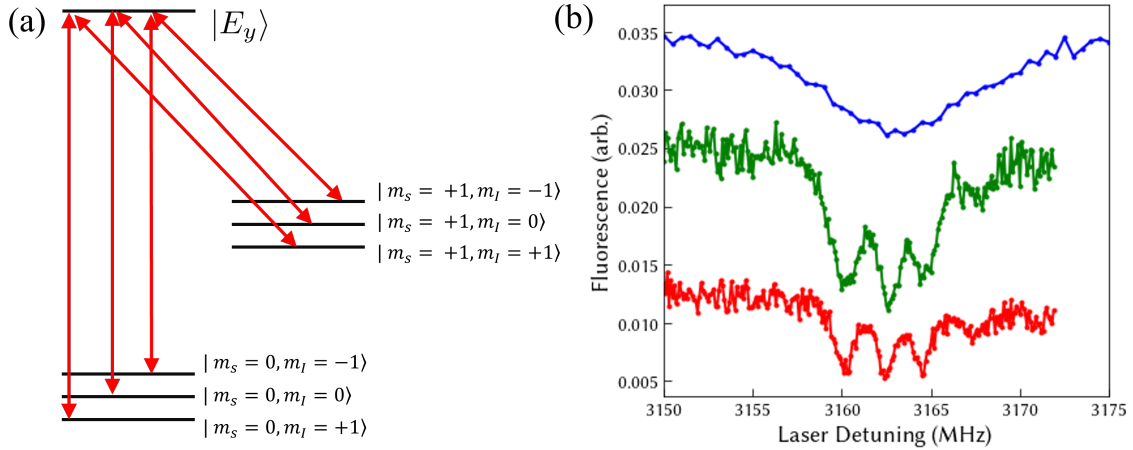
FIGURE 4.3. **(a)** Energy level schematic for nuclear spin resolved CPT. **(b)** Nuclear spin resolved CPT spectral response from high to lower laser powers: 430 nW (blue), 81 nW (green), and 51 nW (red). Each trace is offset from the other for clarity.

4.3. Summary

By utilizing the nonzero spin states of the NV center for coherent population trapping, we can use the technique for monitoring the effects of magnetic fields on the quantum system. Furthermore, we have seen that measurement of the CPT spectral response is not only sensitive to the electron population of the NV but also sensitive to its nuclear state.

As we will see in Chapter V, lowering the linewidth of the CPT spectral response such that we can resolve the nuclear spins increases the sensitivity of the system to smaller magnetic field fluctuations. However, due to the multiple nuclear spin states, the spectral dip is split between three nuclear spin projections. In Chapter VII, we demonstrate an approach to polarizing the nuclear spin to a single state for optimal sensitivity using hyperfine resolved CPT.

CHAPTER V

MAGNETIC FIELD SENSING USING CPT

This chapter contains material coauthored by Hailin Wang and Shuhao Wu in reference [59]. The experiments were carried out by the author and Shuhao Wu.

5.1. Introduction

The first steps for developing a good sensor is to calibrate and ensure that it is representing the measured quantity in an accurate way. Quantum sensors using a single solid-state spin, such as the NV center, open up a range of quantities to measure such as magnetic and electric fields, temperatures, pressures with high sensitivity and nanometer spatial resolution [26][29][30][11][69]. Previous studies have primarily focused on the measurement of static and periodic signals [15][6]. The logical progression is to then sense time-varying signals [70][71][72]

To date, nearly all sensing experiments with single NV's are based on the use of Ramsey interferometry discussed in Chapter III. While repeated Ramsey interferometric measurements provide information on the system, it only give insight to a given snapshot in time at specific and limited time intervals. This places limitations to using Ramsey interferometry for real-time sensing.

In this chapter we report the experimental demonstration of real-time sensing of a time-varying magnetic field by using CPT of a NV center and exploiting the statistical information known about our fluctuating magnetic field. By using CPT, we place the NV in the dark state, limiting optical excitation and emission through destructive quantum interference [61]. A time-varying field can kick the NV center out of or into the dark state, leading to a change in the single-photon emissions

from the NV center. We use this sequence of single-photon emissions to estimate the time-varying magnetic field in real time, with estimation carried out in a field-programmable gate array (FPGA) as illustrated in Figure 5.1.
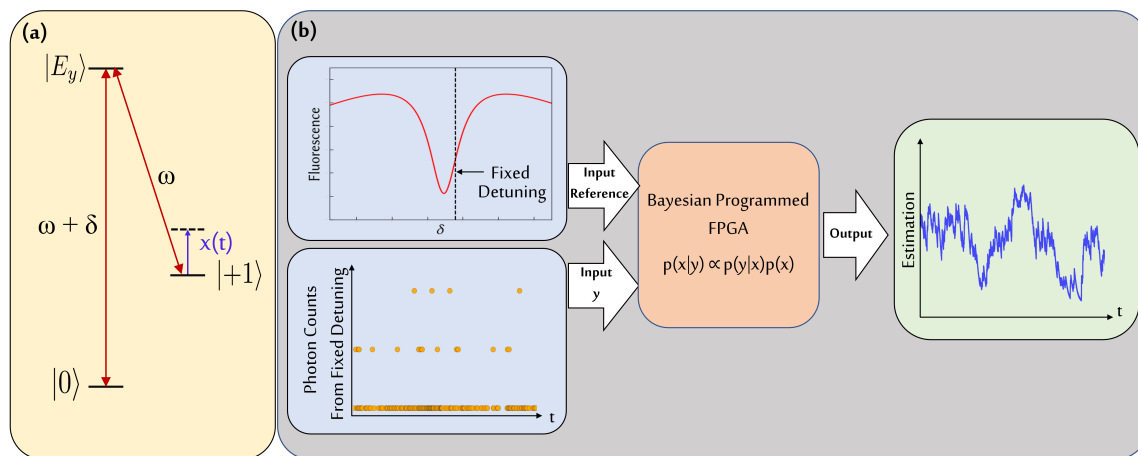
FIGURE 5.1. **(a)** Energy level schematic of CPT system used for real time magnetometry utilizes the $|0\rangle \rightarrow |E_y\rangle$ and $|+1\rangle \rightarrow |E_y\rangle$ transitions while a time varying fluctuation, $x(t)$ is applied. **(b)** Schematic depicting the workflow of the estimation process. A field programmable gate array (FPGA) is programmed with a Bayesian estimator which uses refers to a CPT spectrum with a specific detuning for estimation. As the estimator receives photon counts in real time, the estimator uses Bayesian inference to calculate the probabilities of a frequency shift associated with the received count rate and outputs the estimated fluctuation (blue).

The primary challenge associated with sensing using the dark state is that experimentally, the detection rate of the single-photon emissions limits the effective updating rate of the real-time estimation. With the overall collection efficiency for optical emissions from a NV center at only a few percent under typical experimental conditions, a key challenge is to obtain dynamical information with the few photons detected. This can be overcome by taking advantage of the statistical properties of the time-varying fields, using Bayesian inference to update dynamical information in real time with the detection of just a single photon, demonstrating real-time magnetometry. In this chapter, we discuss the

theoretical framework of our Bayesian estimator and how it compares with other estimators, compare estimation with the actual fluctuations imparted on the NV center and show good agreement between the experimental results and the theoretical expectation. We also compare the experimental results with the the classical Cramer-Rao lower bound (CRLB) for the estimation process.

5.2. Theory

For real-time magnetic-field sensing, we couple the $m_s = 0$ and $m_s = +1$ ground spin states to the E_y excited state in a NV center through two dipole transitions driven respectively by two resonant optical fields (Figure 5.1a). In the limit of equal Rabi frequency, Ω, the dark state for the Λ- type three-level system can be simply written as $(|0\rangle - |+1\rangle)/\sqrt{2}$. As illustrated in Figure 5.1, the electron becomes trapped in the dark state and the optical emission is quenched when the Raman resonance condition, $\Delta = \delta - \omega_B = 0$ is met, where ω_B is the frequency separation between the two spin states and δ is the detuning between the two laser fields.

A time-varying magnetic field, $x(t)$, leads to a corresponding change in ω_B. With an average Raman detuning or bias, $\delta - \langle \omega_B \rangle$, near the half width of the CPT spectral response (Figure 5.1b), the optical excitation of the NV center and the resulting time sequence of single-photon emissions will be directly correlated with the field variation as long as the variation in ω_B does not exceed the half width. It takes only a few spontaneous emission events for the CPT process to reach steady state [62]. For field variations that occur on a timescale that is much longer than the NV radiative lifetime (12 ns [58]), the time series of photon counts, $\{\mathbf{y}_n\} = \{y_1, y_2, ..., y_n, ...\}$, where y_n is the number of photons detected during

the nth time interval, each with a duration of τ, carries the information on the corresponding change in ω_B, denoted as $\{\mathbf{x}_n\} = \{x_1, x_2, ..., x_n, ...\}$ [13].

5.2.1. Ornstein-Uhlenbeck Process

The Ornstein-Uhlenbeck (OU) process is a commonly used stochastic process [54, 55, 56, 73, 74], which is both Gaussian and Markovian. The OU process features two key parameters, memory time (i.e. correlation time), τ_c and standard deviation , σ. The process is characterized by an autocorrelation function $R(t) = \langle x(t_0)x(t_0 + t) \rangle = \sigma^2 e^{-|t|/\tau_c}$ and can be described by the conditional probability between two adjacent events,

$$p_{OU}(x, t_0 + t | x_0, t_0) = \mathcal{N}(x_0 e^{-|t|/\tau_c}, \sigma^2(1 - e^{-2|t|/\tau_c})), \qquad (5.1)$$

where $\mathcal{N}$ is a normal distribution and the mean of the distribution, $x_0 e^{-|t|/\tau_c}$, the variance, $\sigma^2(1 - e^{-2|t|/\tau_c})$, tend toward 0 and σ^2, respectively, for long separation t. As such, the conditional probability converges to $\mathcal{N}(0, \sigma^2)$ which is independent of the previous event. An example of a simulated OU process with $\tau_c = 5$ms and $\sigma/2\pi = 2.2$MHz is shown in Figure 5.2 .

5.2.2. Estimators

Three different estimators were used to output a time series of estimated frequency changes, $\{\tilde{\mathbf{x}}_n\} = \{\tilde{x}_1, \tilde{x}_2, ..., \tilde{x}_n, ...\}$, from the observed time series of photon counts $\{\mathbf{y}_n\}$.

43
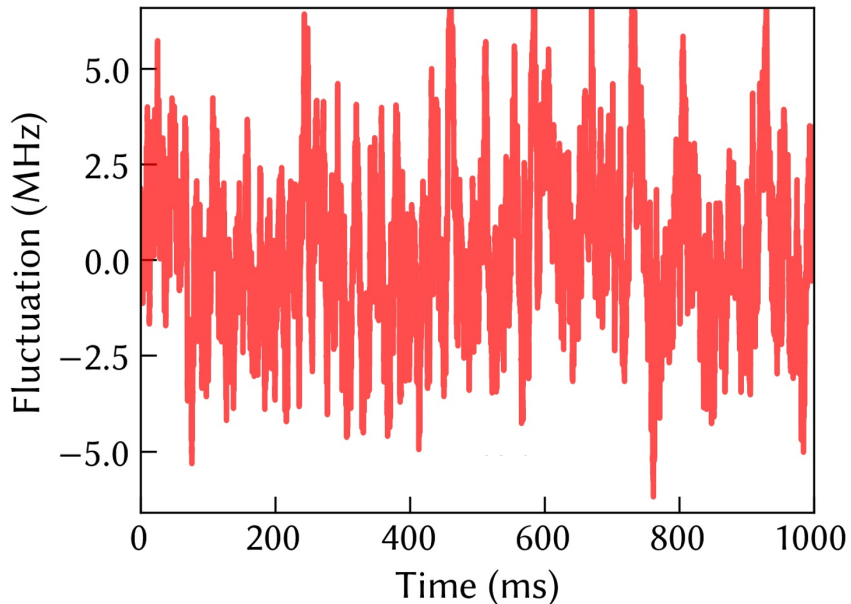
FIGURE 5.2. An example of an AFG output, which follows a simulated OU-process with a correlation time $\tau_C = 5$ ms and a standard deviation, $\sigma/2\pi = 2.2$ MHz.

5.2.2.1. Average Count Estimator

The most intuitive estimator for our experiment is the average count estimator. As implied by the name, the estimator uses the average photon count detected in a relatively long duration, τ_a, to estimate $x(t)$, with

$$y_n^{(a)} \propto \tau_a \rho_{ee}(\tilde{x}_n), \tag{5.2}$$

where $y_n^{(a)}$ is the photon count accumulated between time $nt - \tau_a$ and nt. We then find the estimation by searching for the closest point on our CPT spectral response with a step size of $\sigma/20$.

When choosing a suitable averaging time a tradeoff must be considered. Taking long average times leads to better averaging but with a time lag introduced by the estimator tabulating photon counts for the additional time. Since the

44

estimation at t is determined by the counts accumulated between $t - \tau_a$ and t, the average count estimator has an inherent delay of approximately $\tau_a/2$, which is evident in the experimental results in Figure 5.9b. Based on the results of several estimations for different values of τ_a, we chose to use $\tau_a = 1.3\tau_c$ to carry out our average estimator experiments.

Another issue with the average count estimator is that the difference between $\{\tilde{\mathbf{x}}_n\}$ and $\{\mathbf{x}_n\}$ is often asymmetric, as seen in Figure 5.9b, which shows a much greater positive differences than negative differences. The time series of photon counts used for the estimation is obtained at a given bias δ_0. The bottom of the CPT resonance to δ_0 has a slope that is different from that from δ_0 to $\delta_0 + 3\sigma$. This asymmetry results in different performances on the different sides of δ_0 for the average count estimator.

5.2.2.2. Bayesian Estimator

Our other estimators use Bayesian inference, which has been used in earlier sensing studies with NV centers [72] [75]. Bayesian inference, where

$$p(x_n | y_n, y_{n-1}, \ldots, y_1) \propto p_{\bar{y}_n}(y_n | x_n) \times p'(x_n | y_{n-1}, \ldots, y_1), \tag{5.3}$$

makes use of Baye's Theorem, where $p(x_n | y_n, y_{n-1}, \ldots, y_1)$ is the posterior or the final probability distribution, $p_{\bar{y}_n}(y_n | x_n)$ is the conditional probability of detecting y_n photons in the n-th time interval given x_n, $p'(x_n | y_{n-1}, \ldots, y_1)$ is the prior probability based on the previous information. We assume $p_{\bar{y}_n}$ follows a Poisson distribution with

$$p_{\bar{y}_n}(y_n | x_n) = \frac{\bar{y}_n^{y_n} e^{-\bar{y}_n}}{y_n!}, \tag{5.4}$$

where $\bar{y}_n$ is the average photon counts.

For the simple Bayesian estimator, the prior probability distribution of x_n is the same as the posterior of x_{n-1}. This estimator can be further improved by considering the statistical properties of the OU process. We call this improved estimator the OU Bayesian estimator. For the OU process, the probability of finding x_n at $t_0 + \tau$ given x_{n-1} at t_0 is given by a Gaussian distribution. The prior distribution of x_n can thus be written as a convolution of the posterior distribution of x_{n-1} and the Gaussian conditional probability,

$$p'(x_n = x | y_{n-1}, \ldots, y_1) = \int d\omega \times p(x_{n-1} = x - \omega | y_{n-1}, \ldots, y_1) \times p_{OU}(x_n = x_{n-1} + \omega, t_0 + \tau | x_{n-1}, t_0),$$
(5.5)

where $\tau = 10 \ \mu$s is the interval we choose to discretize estimations, time-varying fields, and photon counts during the experiment. The estimation is then given by,

$$\tilde{x}_n = \int p(x | y_n, y_{n-1}, \ldots, y_1) x dx.$$
(5.6)

As shown in Figure 5.3, the simple Bayesian estimator converges quickly to a constant near zero (the mean for our OU process), which has also been confirmed in our experiment. In this regard, the simple Bayesian estimator is not suitable for real-time estimations. The simple Bayesian estimator does not make use of the statistical properties of the OU process and therefore does not use all available information for the estimation.

5.2.3. Cramer-Rao Lower Bound

The Cramer-Rao Lower Bound (CRLB) is the theoretical bound for the performance of an estimator. How close an estimation is to the actual signal is
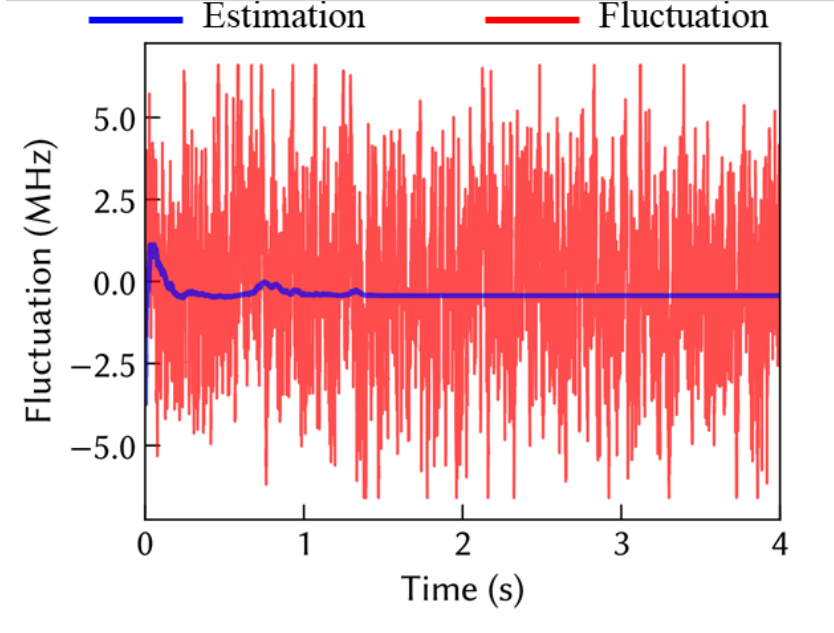
FIGURE 5.3. Simulated estimations using the simple Bayesian estimator (blue). At long times the estimations converge to a value near zero and is unable to capture the dynamics of the actual OU-process (red curve). The parameters used are nearly the same as the raw data shown in Figure 5.9.

characterized by the average estimation variance, defined as $\mathrm{Var}[\tilde{x}_n(\mathbf{y}_n)] =< (\tilde{x}_n(\mathbf{y}_n) - x_n(\mathbf{y}_n))^2 >$. CRLB gives the best estimation variance we can get given the estimation problem. A detailed derivation of the CRLB for CPT-based real-time estimations of an OU process can be found in an earlier study [13]. For this experiment, the CRLB can be formulated as

$$\mathrm{Var}[\tilde{x}_n(\mathbf{y}_n)] \geq \frac{\sigma^2}{\sqrt{1 + 2\tau_c\sigma^2 g(\sigma)}} \times \frac{2}{1 + 4/\sqrt{1 + 32\tau_c\sigma^2 g(\sigma)}}, \qquad (5.7)$$

where $g(\sigma) =< (\partial f/\partial\delta)^2/f >_\delta$ is an average over various detunings, f is the average count rate of the photons detected at a given detuning, δ. It should be noted that a necessary condition for an achievable CRLB is that the posterior follows a Gaussian distribution [73]. For our system, this is only an approximation

since the CPT spectral response around the bias point is neither linear nor quadratic.

5.3. Experiment

To carry out real-time estimation we use the same confocal microscopy setup described in Chapter III. To form the Λ-type system required by the CPT process, a permanent magnet was used to split the $m_s = \pm 1$ states by 590 MHz, allowing for us to resolve the $|0\rangle \rightarrow |E_y\rangle$ and $|+1\rangle \rightarrow |E_y\rangle$ transitions. The two resonant optical fields for the CPT process were derived from a single 637 nm diode laser and a sideband generated by an EOM. Under these conditions, the CPT dip obtained from the Λ-type system shown in Figure 4.2 features a linewidth of 11.6 MHz, which includes contributions from hyperfine splitting (2.2 MHz), spin dephasing (0.6 MHz), as well as power broadening (near 5 MHz).

As this is a proof-of-principle demonstration, we apply an external time-varying magnetic field to the NV center by passing an electric current through the (CPW) fabricated next to the SIL. The electrical current is generated by an arbitrary function generator (AFG), follows a simulated OU process with given σ and τ_c and with $\langle x(t) \rangle = 0$ (Figure 5.4). This allows us to investigate the dependence of the sensing on key parameters of the noise such as σ and τ_c. An identical AFG channel is sent to an oscilloscope used to compare the supplied noise to the CPT-based real-time estimation.

To calibrate the shift in the frequency separation between the $m_s = 0$ and $m_s = +1$ states induced by the external field, we measure the resonance shift of our CPT spectral response as a function of the AFG output voltage (Figure 5.4a). Figure 5.4b plots the frequency separation derived from the least-square Lorentzian

fit to the CPT dip as a function of the corresponding output voltage. The least-square linear fit in Figure 5.4b yields a frequency-to-voltage slope of 3.81 MHz/V.
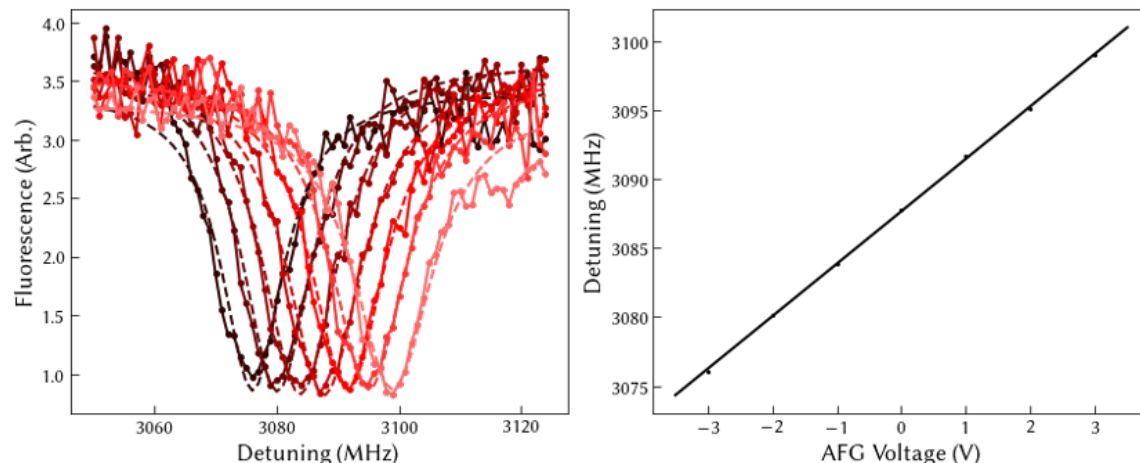
FIGURE 5.4. **(a)** Examples of CPT spectral takes at various fixed AFG voltages. The solid lines are least-square fits to inverted Lorentzians. **(b)** CPT Resonances vs. the corresponding AFG voltages. The solid line is a least-square fit which provides the parameters used by the FPGA.

5.3.1. Pulse Sequence and effects of NV Ionization

Recall from Chapter III that continuous resonant excitation of a NV can ionize the NV to its neutral charge state, NV^0 [76]. To minimize the ionization, we interrupt the sensing process periodically with a 10 μs green laser pulse, with the APD gated off during this initialization or reinitialization process. Figure 5.5a shows the pulse sequence used during the sensing process. The duration between the two successive green laser pulses is set to 100 μs.

The NV^0 center not only makes no contribution to the sensing process, but also distorts the time series of the photon counts used for the estimation. The effects of the NV^0 can be seen clearly from the photon number probability distributions shown in Figures 5.5b and 5.5c, for which the duration between the

two successive initialization pulses is set to 100 and 500 μs, respectively. For these photon number probability distributions, we time-tag the detected photons for 10 s and bin the photon counts in 10 ms bins. The solid red lines in Figures 5.5b and 5.5c are the corresponding Poisson distributions, for which the average count rate is set by the experimentally observed value. The photon number distribution in Figure 5.5c exhibits a greater deviation from the Poisson distribution as well as a lower average count rate than that in Figure 5.5b, indicating increasing effects of NV ionization with the increasing separation between successive initialization pulses.
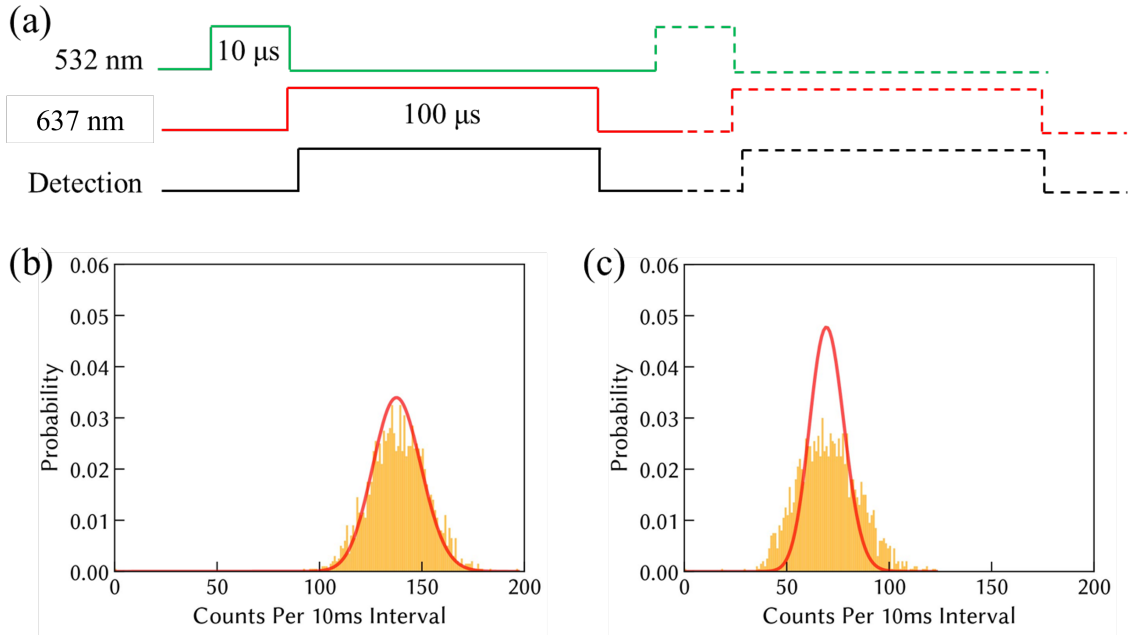
FIGURE 5.5. **(a)** Schematic of the repeating pulse sequence used for real-time sensing. **(b)** & **(c)** Photon number probability distributions obtained from the time-tagged photon counts, for which the separation between two successive green pulses is 100 and 500 μs, respectively. The red curves are the Poisson distributions with the average photon counts set by the experimentally observed values.

To determine the fidelity of charge initialization or reinitialization, we apply a repeating pulse sequence consisting of a 10 μs, 532 nm initialization

pulse followed by a 1 ms resonant excitation pulse (near 637 nm) for 20s, time-tagging each photon received. We then bin the number of photons detected during each red pulse (which is our readout interval). Figure 5.6 shows the distribution of photon counts per readout interval, which appears to be bimodal. We apply a least-squares fit of the observed distribution to the sum of two Poisson distributions, one for each charge state. An average count rate of 0.65 and 4.45 counts per readout interval are obtained from the numerical fit for the NV^0 and NV^-, respectively. The relative contribution of counts from the NV^- determines the fidelity for charge initialization. The observed fidelity of approximately 75% is consistent with earlier studies [77].
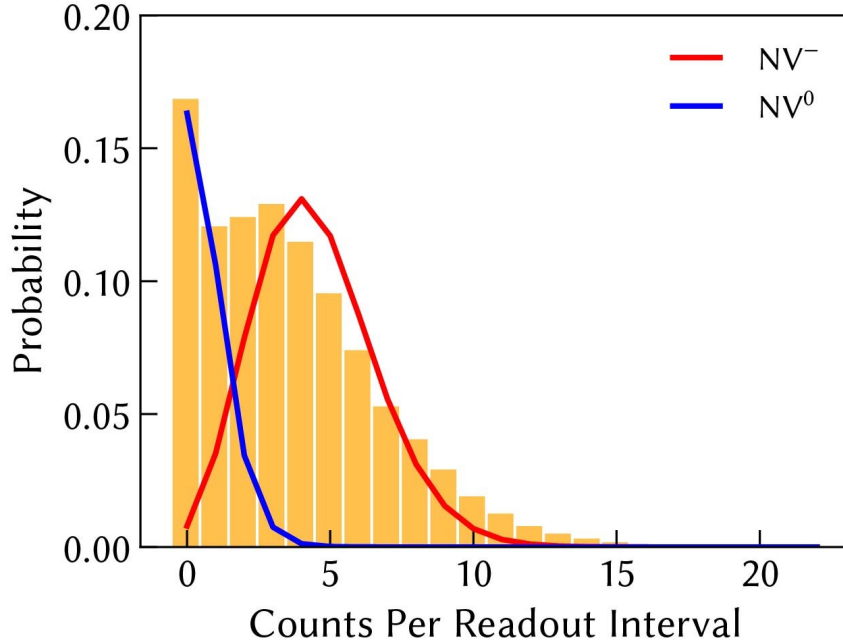
FIGURE 5.6. Photon number probability distribution for the separation between two successive initialization pulses equals the readout interval (1ms). The distribution can be described as a sum of two Poisson distributions, with an average count rate of 0.65 and 4.45 counts per readout for the NV^0 (blue) and the NV^- charge states, respectively.
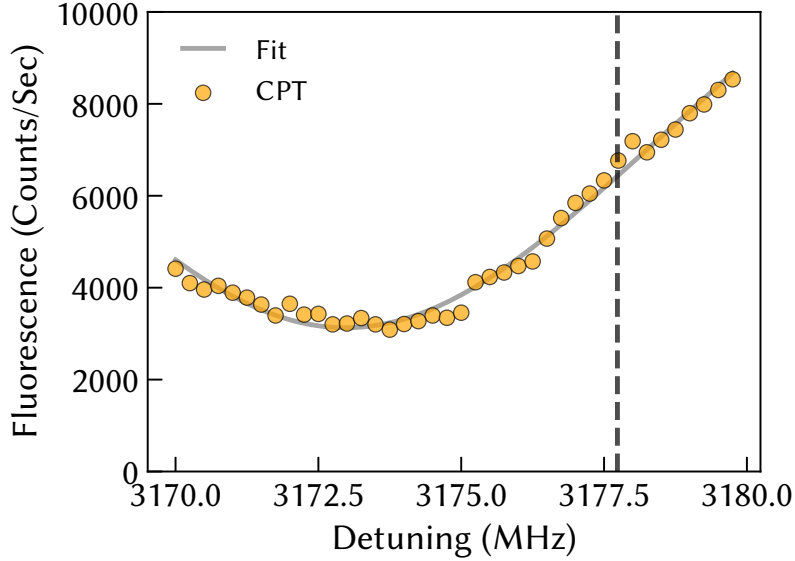
FIGURE 5.7. An example of a CPT spectral response and the least-square fit to an inverted Lorentzian used in the estimation. The vertical dashed line indicates the position of the fixed detuning, at which the real-time sensing is carried out. The corresponding photon count rate (obtained from the CPT spectral response) sets the average count rate for the estimations carried out at this detuning.

5.3.2. Field Programmable Gate Array

For the real-time estimations, we implemented the three different estimators using a FPGA (Xilinx 7k410t) included in the Keysight M3302A card. The FPGA takes as input the time series of detected photon counts, y_n, as well as other relevant parameters, such as the CPT spectral response and the bias or Raman detuning, and then outputs an estimation, $\tilde{x}_n$, of the frequency shift, x_n, induced by the external time-varying magnetic field. Prior to each estimation run, we experimentally measure the CPT spectral response and numerically fit the CPT dip to an inverted Lorentzian. An example is given in Figure 5.7. The numerical fit of the CPT spectral response is then used in the subsequent estimation process.

Here we discuss specifically the implementation of the OU-Bayesian estimator. Similar approaches are also used in the implementation of average

count as well as simple Bayesian estimators. For the OU-Bayesian estimator, the arrays, $p_{\bar{y}_n}(y_n|x_n)$ and $p_{OU}(x_n, t_0 + \tau|x_{n-1}, t_0)$, (see Section 3.3)) are evaluated for $y_n = 0, 1, 2, 3$ and $-3\sigma \leq x_n \leq 3\sigma$ with a step size of $\sigma/10$. We choose cutoff values of $y_n \leq 3$ and $|x_n| \leq 3\sigma$ since the probabilities for values beyond these ranges are negligible. These two arrays are uploaded to the FPGA for use during the estimation.

The Keysight M3302A card contains a digitizer and an arbitrary waveform generator (AWG) as well as a FPGA. During the estimation process, photon counts in the form of TTL pulses received by the Keysight M3302A card are digitized by the built-in digitizer. Within the Keysight card, an AND logic block asserts high if the system is gated within the detection pulse shown in Figure 5.5a, allowing the signal to proceed to the photon accumulator (see Figure 5.8). For every time interval ($\tau = 10$ μs), the photon accumulator block sends the number of photon counts detected in the interval, y_n, to the FPGA. The FPGA, with the additional inputs as discussed above, then follows the process outlined in Section 5.8 to output an estimated x_n. A voltage proportional to the estimated x_n is then generated by the AWG. We monitor both the estimations and the AFG output voltages (which are proportional to the time-varying external fields) on an oscilloscope (see Figure 5.9).

Note that the estimators are initially programmed in C++. For the implementation in a FPGA, the C++ programs are converted to the native FPGA language, Verilog, using Xilinx HLS. The processing time for the estimation process from receiving y_n to outputting an estimation is approximately 7 μs.
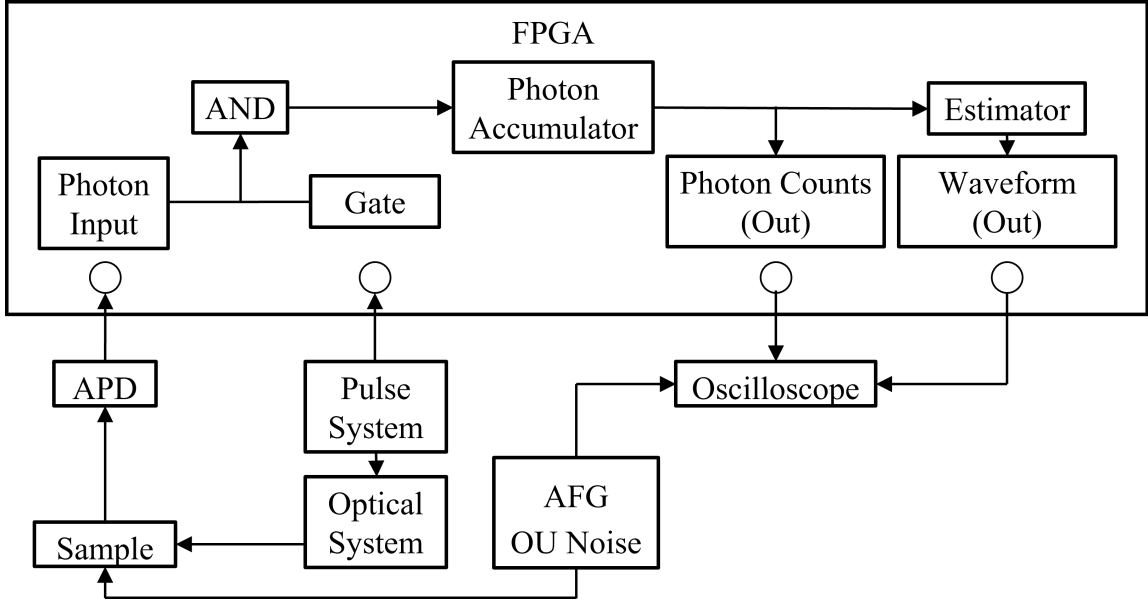
FIGURE 5.8. A block diagram of the functions of the Keysight M3302A card and its relation to the rest of the experimental setup.

5.4. Real Time Magnetometry

Estimations obtained with the OU-Bayesian estimator, which takes into account the statistical properties of the OU process, and with the average count estimator are shown in Figure 5.9a and 5.9b, respectively, as well as a direct comparison between the estimations and the actual frequency changes. For these experiments, we used $\sigma/2\pi = 2.2$ MHz, $\tau_c = 5$ms, and an average phton count rate of 5400 per second. The Raman detuning or bias was set to $(\delta - \langle\omega_B\rangle)/2\pi = 4$MHz. As shown in the figures, estimations obtained with the OU-Bayesian estimator closely follow the actual field dynamics, whereas estimations obtained with the average count estimator exhibit large deviations from the actual frequency changes for extended periods of time.

Zooming in to relatively short durations (marked by the dashed-line boxes in Figures 5.9a and 5.9b), the differences between these two estimators are
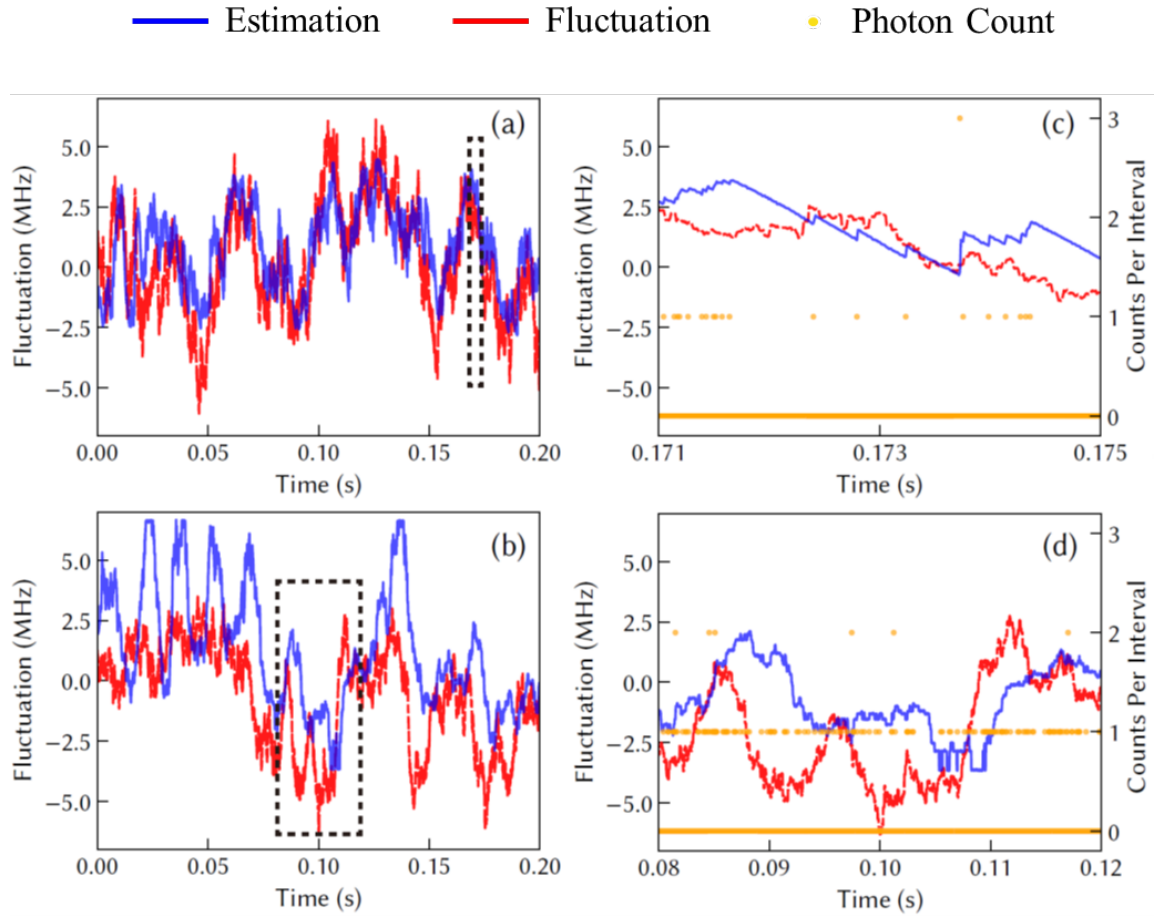
FIGURE 5.9. **(a)&(b)** Estimations (blue solid line) of the fluctuations in $\omega_B/2\pi$ obtained with the OU-Bayeseian and the average count estimators, respectively, along with the actual fluctuations (red dashed line). **(c)** & **(d)** A closer look at the results in the dashed-lined boxes in (a) and (b), respectively, along with the corresponding photon counts (orange dots) per updating interval.

highlighted and plot with the corresponding time series of photon counts. Figure 5.9c shows that the OU-Bayesian estimator can effectively update the dynamics of the frequency change in real time at the single photon level. A previous study used the complete CPT spectrum of a sinle NV for the sensing of the magnetic fluctuations induced by the nuclear spin bath [78], for which it took about 100 detected photons to obtain a single estimation.

In comparison with the OU-Bayesian estimator, the average count estimator is susceptible to photon number shot noise, which leads to large spikes in the estimation observed in Figure 5.9b. The asymmetry in spikes is in part due to the choise of the Raman bias, which is considerably smaller than the halfwidth of the CPT spectral response. As can be seen from Figure 5.9d, there is also a large delay between the estimation and the actual frequency change due to the relatively long τ_a used. Note that significantly increasing τ_a and thus $y_n^{(a)}$ leads to reduced fluctuation in the estimation but at the expense of lower time resolution. Average count estimators could, however, work well for the sensing of static signals. For example, electromagnetically induced transparency (EIT), which is closely related to CPT, of an ensemble of NV centers has been used successfully for static sensing [39].

5.5. Analysis

For a quantitative analysis of the estimations, we take a look at the estimation variance which is defined as $\mathrm{Var}[\tilde{x}_n] = \langle (\tilde{x}_n - x_n)^2 \rangle$ and in particular $\langle (\tilde{x}_n - x_n)^2 \rangle / \sigma^2$, which we denote as Var/σ^2. We also compare the estimation variances obtained from the experimentally observed time series of photon counts and those obtained from the theoretically simulated time series of photon counts.

The theoretical model used for the simulations is presented in our earlier study [13]. To directly compare with the experiment we simulate single-photon emissions with the assumption that those emissions follow a Poisson distribution. To account for the 75% charge initialization fidelity, we label each readout period (100μs) as a zero count readout with 25% probability, or as a Poissonian readout with 75% probability. We then simulate a time series of photon counts, with an

update time interval $\tau = 10$ μs, during which the counts are generated according to a Poisson distribution or zero counts are generated, depending on the readout label. We set the average count rate, $\bar{y}_n$, to that derived from the numerical fit to the experimentally obtained CPT spectral response (see Figure 5.7). We load the simulated time series of photon counts and the conditional probability arrays discussed in Sections 5.3.2 to a simulated FPGA (programmed in Python), which then outputs the estimations. The simulated estimations are analyzed in the same manner as the experimental results.

Figure 5.10a plots Var/σ^2 as a function of τ_c and compares the relative variances obtained with the OU-Bayesian estimator, the average count estimator, and the simple Bayesian estimator, which takes no account of the statistical properties of the OU proscess. As expected, the variances for both average count and the OU-Bayesisan estimators decrease with increasing τ_c. Nevertheless, Var/σ^2 for the average count estimator is far above 1 when τ_c is near 1 ms and only falls slightly below 1 when τ_c approaches 10 ms. In comparison Var/σ^2 for the OU-Bayesisan estimator remains significantly below 1 when τ_c approaches 1 ms.

It should be noted that with Var/$\sigma^2 \approx 1$ for the range of τ_c used in Figure 5.10a, the simple Bayesian estimator essentially provides no information on the time-varying field. As shown in our earlier theoretical study [13] and confirmed in additional experiments, estimations obtained with the simple Bayesian estimator quickly converge to the average value, with $\tilde{x}(t) \approx 0$.

Figure 5.10b compares the experimentally observed variances with the corresponding simulated variances. Both variances were obtained with the OU-Bayesian estimator. We found that the experimentally observed variances, for which a perfect charge state initialization for the negatively charged NV center is
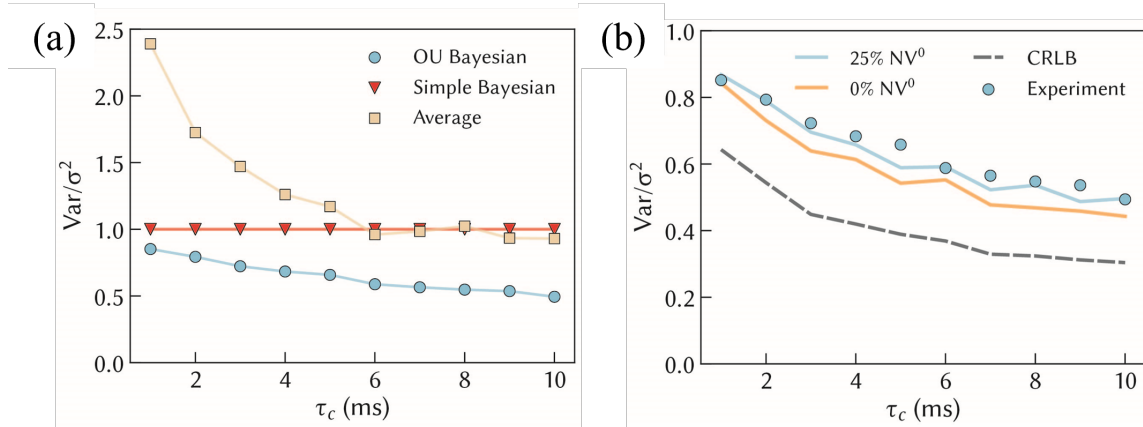
FIGURE 5.10. **(a)** Comparison of estimation variances obtained with OU-Bayesian, simple Bayesian, and average count estimators as a function of τ_c. **(b)** Comparison of the estimation variances obtained with the OU-Bayesian estimator wih the corresponding simulated values, for which charge initialization fidelity of 100% (dotted line) and 75 % (solid line) is assumed. The dashed line shows the calculated CRLB. Experimental parameters used are he same as those for the above figure, unless otherwise specified.

assumed. As shown in section 5.3.1, the charge initialization fidelity is about 75 %. Including the nonideal charge initialization in the model yields a good agreement between the experiment and the simulation. Figure 5.10b also shows that the experimentally observed variance is considerably above the calculated CRLB which can only be reached when the CPT response is linear or quadratic.

The estimation variances also depend on the choice of CPT parameters, especially the bias. Figure 5.11a shows Var/σ^2 obtained with the OU-Bayesian estimator as a function of the the bias, with other experimental conditions the same as those used for Figure 5.9a. As expected the estimations become ineffective when the bias approaches 0 (near the bottom of the CPT dip), in agreement with the theoretical expectation. The estimations also perform poorly when the bias significantly exceeds the halfwidth of the CPT dip. Note that near the wings of the CPT dip, effects of hyperfine splitting of the relevant spin states, which are

58

not included in the theoretical model, become important, leading to the observed variances that are large than the simulated values, as shown in Figure 5.11a.
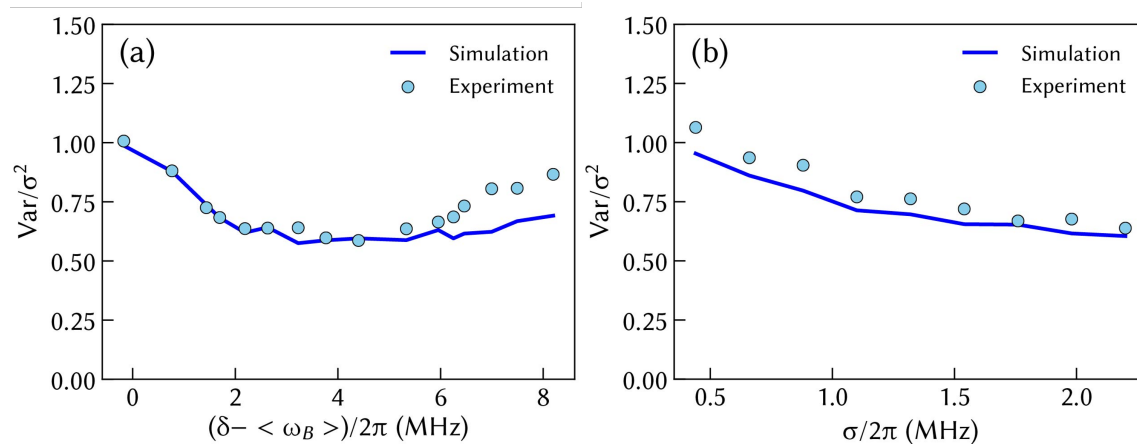
FIGURE 5.11. **(a)** Estimation variances obtained with the OU-Bayesian estimator as a function of the bias (i.e. Raman detuning). (b) Estimation variances obtained with the OU- Bayesian estimator as a function of σ. The solid lines in both figures show the corresponding simulated values.

The sensitivity and range of the real-time sensing process also depends on the CPT parameters. In particular there is a tradeoff between the largest and the smallest frequency changes that can be sensed via a CPT process. The CPT linewidth sets the range of the sensing process, smaller linewidths creating a more sensitive sensor. Figure 5.11b shows Var/σ^2 obtained with the OU-Bayesian estimator as a function of σ, with other experimental conditions the same as those used for Figure 5.9a. For relatively small σ, Var/σ^2 increases with decreasing σ and goes above 1 when $\sigma/2\pi$ falls below 0.5 MHz. In this case, the large CPT linewidth (11.6 MHz) used in the experiment limits the sensitivity of the real-time sensing process. The experimental results are in good agreement with the simulated values, as shown in Figure 5.11b.

The sensitivity of the real-time sensing process can be further improved by reducing the CPT linewidth. For example, polarizing the ^{14}N nuclear spin with

optical pumping avoids the complication of hyperfine splitting [66]. The use of isotopically purified diamond reduces the dephasing induced by the nuclear spin bath and can lead to a CPT linewidth less than 1 kHz [11]. Additional improvements in the overall sensing performance can also be achieved through better charge initialization, perhaps through the use of real-time control techniques [79]

5.6. Summary

In summary, we have demonstrated real-time magnetometry using dark states in a NV center by estimating the time-varying magnetic field from the corresponding time series of photon counts in a CPT setting. A Bayesian estimator that takes advantage of the statistical properties of the time-varying field can effectively update the dynamical information of the field with the detection of a single photon. While the statistical parameters needed for the OU-Bayesian estimator can be obtained using traditional time-resolved measurement techniques, these techniques are not suitable for directly probing the real-time dynamics at nanoscale resolutions.

While a NV center has been used as a model system for our proof-of-principle demonstration, the technique we have described can be extended to other solid state spin systems [80]. The magnetometry can be used for studies of time-varying magnetic fields in a variety of systems at the nanoscale, for example, nuclear spin baths [12, 13, 14], and two-dimensional semiconductors [9, 10]. As we will see in the next chapter, combining real-time sensing with feedback control also opens new avenues, such as protecting a spin qubit from the fluctuating magnetic

environment via feedback control [12, 71] and estimating the statistical parameters of the field using Bayesian parameter estimation.

CHAPTER VI

FEEDBACK CONTROL

The following section contains material coauthored with Shuhao Wu and Hailin Wang. The experiments discussed were performed by myself and Shuhao Wu.

6.1. Introduction

Spin-based quantum sensors, such as single NV centers, allow sensitive measurements of physical quantities, including magnetic and electric fields, temperature, and strain, with nanometer spatial resolution. Most spin-based sensors are based on transient Ramsey interferometry. As we saw in the last chapter, quantum sensing can also take place by continuously monitoring the sensor through photon counting [59]. Bayesian inference, an effective and versatile platform for parameter estimations, has also played a major role in the development of quantum sensors [81][82]. Combining Bayesian parameter estimations (BPE) with Ramsey interferometry has led to major improvements in measurement sensitivity, speed, and dynamics [75]. BPE, however, can have serious limitations. For the single-photon real-time sensing demonstrated in the last experiment, it is essential that the statistical properties of the magnetic field fluctuations are known and are taken advantage of in the BPE, which is not feasible for many intended applications.

In this chapter, we show that we can overcome this limitation by introducing feedback control to the continuous BPE, followed by a separate verification period. Using the same CPT-based sensor with a feedback control mechanism we extend

the decoherence time caused by a time-varying magnetic field. As previously discussed, the sensor operates while placing two ground spin states of the NV center in a special superposition known as the dark state. By monitoring the dark state fluorescence, we estimate magnetic field fluctuations using a Bayesian inference based estimator informed by the time series of detected photon counts and the parameters of the time-varying field. Feeding the estimated signal back into the system, we counteract the fluctuations, stabilizing the dark state and extending the coherence time of the ground state (Figure 6.1). We perform a verification of the feedback loop's performance by measuring the spin decoherence rate of the NV, $1/T_2^*$, before and after introducing feedback control using Ramsey interferometry. Additionally, we report a means of parameter optimization, useful for determining the statistical parameters of the fluctuating magnetic field by exploiting the Bayesian estimator's sensitivity to its input field parameters. The parameters of the fluctuating field can be attained by sampling various parameters and optimizing the each parameter's measured improvement in T_2^*.

6.2. Feedback Control

Feedback control solves several problems posed from the previous Chapter's experiments. The first being that the comparison between the applied fluctuation and estimation in the previous chapter are a indirect measure of sensing performance. The other is that to output an estimation of the magnetic field using the detected photon sequence, a statistical model of noise is required for the FPGA to output an estimation, the model and its parameters are typically unknown. We solve these problems by inserting a feedback loop to the system and monitor how the system respond.

The feedback loop in our system uses a simple T junction depicted in Figure 6.1, which subtracts the estimated fluctuation from the generated fluctuation, $x(t)$. Due to the accuracy of our estimator, the final fluctuation is reduced, thereby stabilizing the dark state and corresponding photon counts. However, by introducing the feedback mechanism, we reduce the effects of the magnetic field
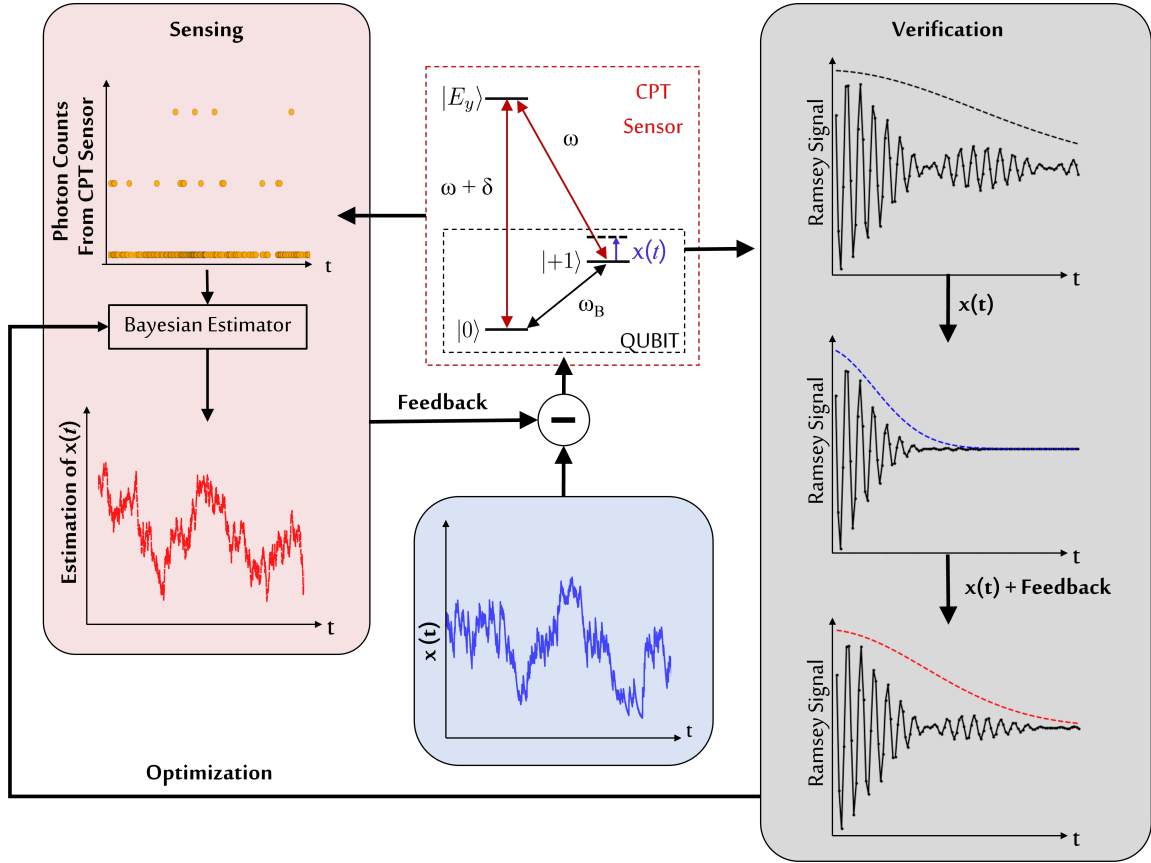
FIGURE 6.1. Schematic illustrating real-time feedback control of time-varying magnetic fields using single-photon emissions from a CPT-based sensor. The sensing process (red section) estimates a fluctuating magnetic field, $x(t)$, by feeding single photons from the CPT sensor (red dashed box) into a Bayesian estimator whose output estimation is subtracted from the fluctuating signal. Verification of the feedback process (grey section) is carried out by performing Ramsey interferometry on the ground state qubit of the NV (black dashed box). Verification results can be optimized by altering the fluctuation parameters used for real-time estimation.

fluctuations on the likelihood of photon emission. Taking this into account, the likelihood function then becomes

$$p_{\bar{y}_n}(y_n|x_n, \tilde{x}_{n-1}) = \frac{\bar{y}_n^{y_n} e^{-\bar{y}_n}}{y_n!}, \qquad (6.1)$$

where $\bar{y}_n \propto \tau \rho_{ee}(x_n - \tilde{x}_{n-1})$ is modified by previous estimation.

The combination of estimator and feedback loop results in a more accurate and sensitive system. The principle behind such improvement is illustrated in Figure 6.2. The feedback procedure narrows the effective fluctuation distribution, limiting the range of x_n from $-3\sigma < x_n < 3\sigma$ such that they fall into the optimal sensing range surrounding the chosen bias. Since the corrected fluctuation becomes the estimation error, the difference between the output estimation and the initial fluctuation, $x_n - \tilde{x}_n$, the magnetic field fluctuations imparted onto the dark state is now less than those without feedback control resulting in a fluctuation range of $-3\sigma` < x_n - \tilde{x}_n < 3\sigma'$, where $\sigma' < \sigma$. Looking at Figure 6.2b, the black curve shows the sensitivity of our sensor, $g(\sigma)$, from equation 5.7 at each possible bias, δ_0, of the CPT spectral response. Recall that $g(\sigma)$ is calculated by averaging the magnetic field noise distribution centered δ_0, $\delta_0 - 3\sigma < \delta < \delta_0 + 3\sigma$, where δ is the detuning from Raman resonance. The largest possible reduction in σ would be $\sigma' = 0$, resulting in a sensitivity shown by the red curve in Figure 6.2, where $g(\sigma')$ is calculated for each δ_0 averaged over a delta function centered at δ_0. In other words, the effective sensitivity at a chosen bias lies somewhere between the red and black curves, the black being no feedback control $\sigma' = \sigma$, and the red being absolute control $\sigma' = 0$, meaning an enhanced sensitivity with feedback control when compared to our bare sensing experiment in the previous chapter. The effects of this can be seen by comparing the raw data in Figure 6.3.
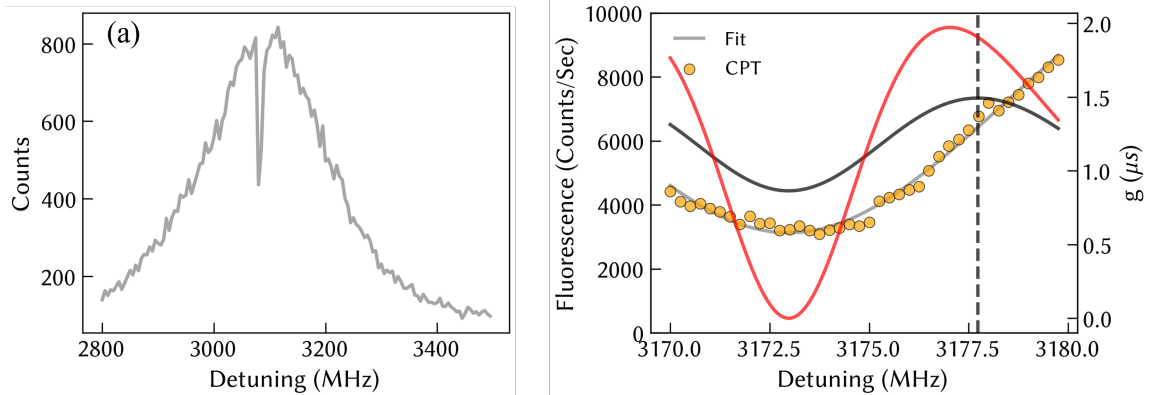
FIGURE 6.2. **(a)** Full CPT spectral response. **(b)** A closer look at the CPT spectrum in (a) where the yellow dots are fluorescence counts, and the grey curve is the underlying Lorentzian fit. Red and black curves show the sensitivity, g, from equation 5.7, at each point in the spectrum with and without fluctuation distribution.

Performance of our feedback control technique is directly assessed by measuring the improved spin decoherence time, T_2^*, of a ground state NV qubit. Measurement of T_2^* using microwave Ramsey interferometry is used ubiquitously in quantum control applications [26, 33]. As discussed in Chapter III, each Ramsey measurement begins by placing the qubit in an equal superposition, $(|m_s = 0\rangle + |m_s = +1\rangle)/\sqrt{2}$, using a microwave field detuned from ω_B by a frequency, δ_{MW}, after which it is left to freely precess at a rate equal to δ_{MW}. During precession, the qubit interacts with the fluctuating magnetic field which causes a fluctuations in ω_B thereby introducing random phase fluctuations leading to decoherence of the qubit. The system is then subjected to a spin-projection measurement where the effects of decoherence can be observed as a decay in amplitude of the spin's precession. After several measurements at different precession times we can determine the T_2^* of the system. Comparing the effects of the applied fluctuations with and without feedback control on T_2^* gives us a clear indicator of feedback control performance.

6.3. Experiment

For this experiment we use the same setup described in the preceding chapters. Some minor alterations were made to the experimental setup in order to implement the feedback control process. To resolve the ground state spins a permanent magnet was placed outside of the cryostation, splitting the $m_s = \pm 1$ states by 430 MHz. The CPT spectral response generated for these experiments featured a linewidth of 17.9 MHz made up of contributions from the hyperfine splitting, 2.2 MHz, spin dephasing, 0.62 MHz, and power broadening with an estimated $\Omega/2\pi = 10.6$ MHz.

To demonstrate the proof-of-principle feedback experiment, we apply an external time-varying magnetic field to the NV center by applying a slowly varying voltage across the CPW fabricated next to the SIL. The voltage is generated using an arbitrary function generator (AFG) follows a simulated OU process. The estimated magnetic field fluctuation is subtracted from the AFG signal before transmitting the fluctuation through the waveguide. Additionally, MW ground state control used for Ramsey interferometry is also applied via the CPW, using MW pulses with Rabi frequency, $\Omega_{MW}/2\pi = 20$MHz detuned from the $m_s = 0$ and $m_s = +1$ ground state transition by δ_{MW}.

6.3.1. Sensing and Feedback

Our feedback control experiment begins with the initialization of the NV to the $m_s = 0$ state using a 10 μs green laser pulse ($\lambda = 532$ nm) followed by a long (100 μs) CPT pulse during which the two CPT fields are applied to the NV while fluorescence is simultaneously collected. Real-time feedback is carried out using the FPGA in a Keysight M3302A card containing a digitizer and arbitrary
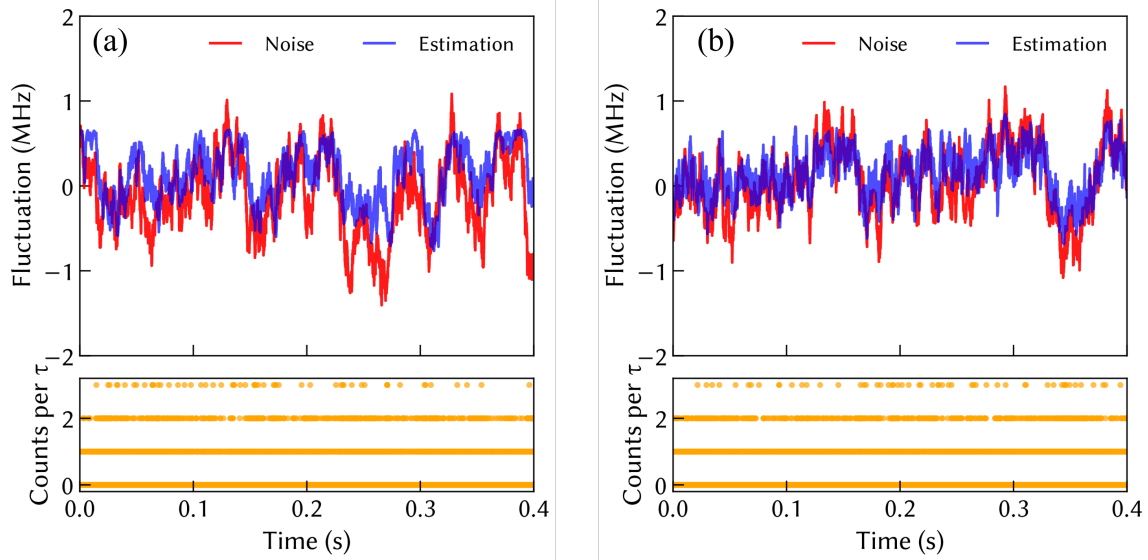
FIGURE 6.3. (a) Raw data for photon counts received during each update interval τ, disturbances input into system, and corresponding estimated fluctuation under sensing setup. (b) Similar raw data obtained with feedback loop applied. Simulated OU fluctuation has a $\sigma = 2.2$ MHz and $\tau_C = 10$ ms memory time.

waveform generator (AWG). The digitizer accumulates the number of photon counts per update time interval, and the AWG outputs a voltage corresponding to the estimated fluctuation generated from the AFG. Those signals are subtracted within the AFG before being sent to the CPW.

To demonstrate the real-time sensing and feedback carried out in our experiment, we provide a sample of our raw data in Figure 6.3. As shown in Figure 6.3a, under a standard sensing process, the blue curve is the estimation obtained by extracting information from corresponding photon sequence (orange dots) which follows the trend of generated noise (red curve). Figure 6.3b shows the raw estimation while applying the feedback. Note that sensing performance is slightly better than the estimation in Figure 6.3a.

6.3.2. Ramsey Verification

After each 100 μs sensing-interval, verification of the feedback process is carried out by Ramsey interferometry. The pulse sequence used for each Ramsey measurement shown in Figure 6.4a starts with another 10 μs green initialization pulse followed by a MW $\pi/2$-pulse, placing the NV center in a superposition between the $m_s = 0$ and $m_s = +1$ spin states. The NV center is then allowed to freely precess for a variable duration τ_{Ramsey}, exposed only to the OU process or feedback-subtracted signal. After applying a second MW $\pi/2$-pulse, the electron population in the $m_s = 0$ spin state is readout using the $m_s = 0$ to E_y transition. Figure 6.4b shows Ramsey measurement with and without feedback. The spin decoherence times caused by the OU process were measured to be on the order of 100 ns. Due to such a fast spin decoherence time, we required a detuning of 60 MHz to observe a sufficient number of Ramsey fringes in order to obtain a least-squares fit for a precise measurement of T_2^*.

6.4. Results

Looking at Figure 6.4b we can see the effects of feedback control on the spin decoherence time of the NV center. For both traces, the NV center was subjected to magnetic field fluctuations following an OU process with parameters $\tau_c = 15$ ms and $\sigma/2\pi = 2.2$ MHz. Each data point corresponds to the fluorescence obtained from a 100000 spin projection readouts for a free precession duration, τ_{Ramsey}. The resulting Ramsey fringe pattern is fit with the sum of three sinusoids, corresponding to each of the ^{14}N hyperfine spin projections ($m_I = 0, \pm 1$), multiplied by a Gaussian envelope, $e^{-(t/T_2^*)^2}$. Fits of the data shown in Figure 6.4b indicates spin decoherence times of $T_2^* = (182 \pm 18)$ ns and $T_2^* = (90 \pm 10)$ ns, with
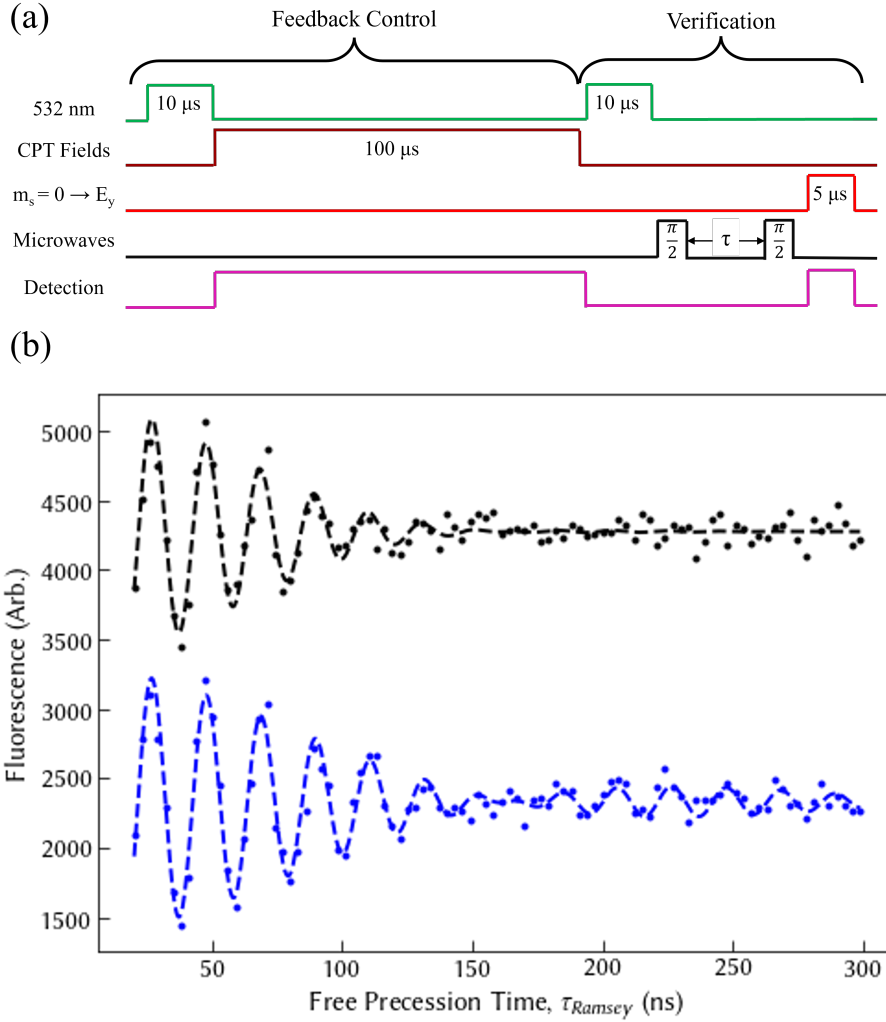
FIGURE 6.4. **(a)** Pulse sequence for real-time feedback and verification. **(b)** Ramsey interferometric measurements for determining the spin decoherence time, T_2^*, with and without feedback control shown in the blue and black respectively.

and without feedback control, respectively. This verifies the real-time estimation and feedback control technique, extending the decoherence time by a factor of 2.

A primary feature of this technique is its sensitivity to fluctuation parameters input into the FPGA. Specifically, one can use this technique to identify the statistical parameters of the time-varying field by optimizing the performance of the feedback system. For practical applications, the system is smooth and

insensitive to small fluctuations, making our application useful for determining the actual parameters of decoherence source. To demonstrate this, we subject the NV center to magnetic field fluctuations with $\tau_c = 10$ ms and $\sigma/2\pi = 2.2$ MHz. We then vary the parameters input to our real-time estimator and measure the resulting T_2^* after implementing feedback control on the system. The results from this experiment are shown in Figure 6.5. For our system the Bayesian estimator is the optimal estimator under approximation. Therefore, we expect the best performance to occur at the center of the heatmap where the correct parameters lie.
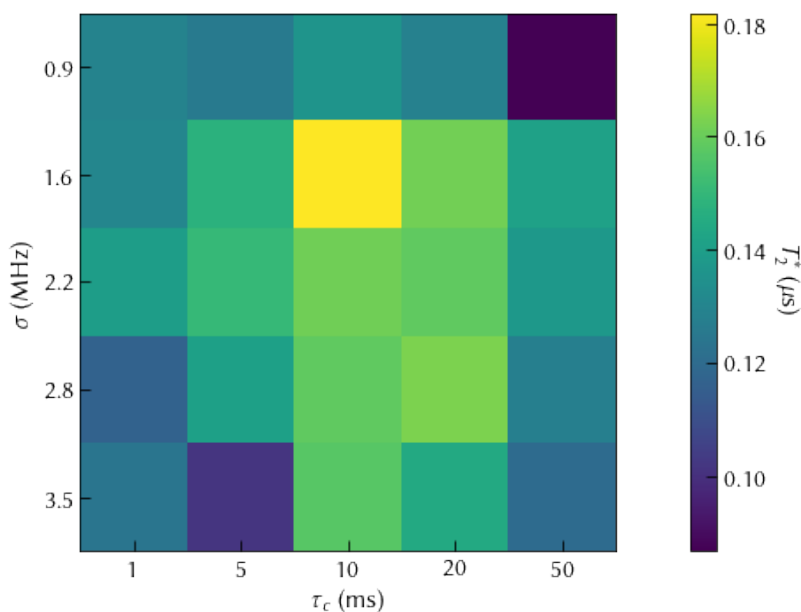
FIGURE 6.5. We scan the memory time and standard deviation used for modelling Bayesian estimator, while the actual parameters of fluctuation locates at the center with $\tau_c = 10$ ms and $\sigma/2\pi = 2.2$ MHz. The maximum decoherence time under feedback loop occurs at $\tau_c = 10$ ms and $\sigma/2\pi = 1.6$ MHz, which is quite close to the actual parameters.

Looking at the heatmap shown in Figure 6.5, we can see that our system correctly optimized T_2^* for the τ_c parameter but inaccurately predicts σ. The deviation from expectation can be caused by several factors such as experiment

71

noise, calibration error, assumption error for the Bayesian estimator, these all can make the Bayesian estimator no longer optimal, affecting the accuracy of parameter verification. As long as these factors are not significant, the parameters determined in this way should be quite close to the actual parameters.

We now turn our attention toward the performance of our feedback system and its dependence on the τ_c of the fluctuating field. Figure 6.6 shows the factor of improvement in T_2^* after implementing real-time feedback control for fluctuations with $\sigma/2\pi = 2.2$ MHz at various τ_c. The performance of the feedback system works well as we increase τ_c due to the increased number of collected photons for estimation. The improvement factor plateaus after $\tau_c = 15$ ms. As the fluctuation τ_c increases change in detected photon counts between subsequent τ intervals become too small for the system to perceive. Conversely, for smaller τ_c, the factor of improvement drops because there are not enough photon counts to capture the faster fluctuation dynamics.
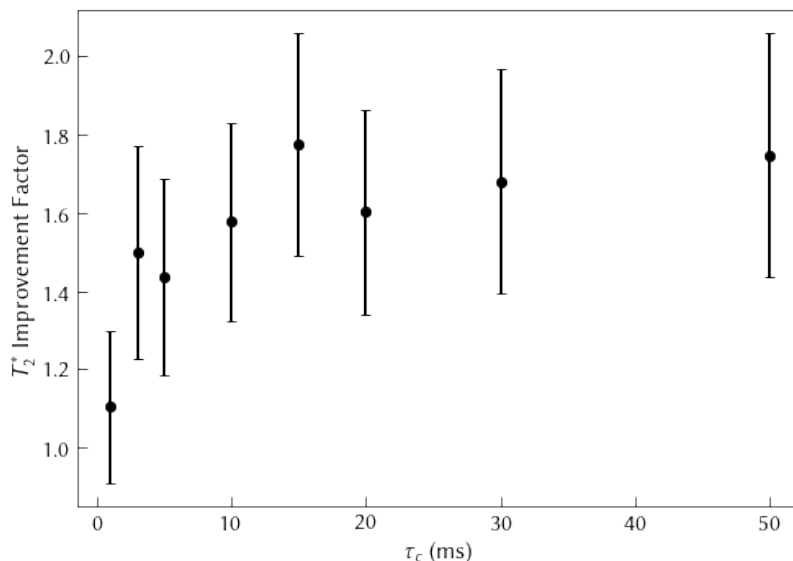
FIGURE 6.6. Factor of improvement in T_2^* using feedback control as a function of τ_c.

6.5. Summary

In summary, we have demonstrated real-time feedback control on a NV center affected by a time-varying magnetic field using the detection of a time-series of photon counts emitted from a CPT-based sensor. The performance of this technique was verified using Ramsey interferometric measurements to measure the improvement of T_2^* after applying real-time feedback control. The sensitivity of the Bayesian estimator to the input statistical parameters of the time-varying field enables an optimization protocol that can be used to extract the actual statistical parameters of the field.

CHAPTER VII

NUCLEAR SPIN POLARIZATION

7.1. Introduction

Nuclear spins are the focus of a variety of studies that require long relaxation times on the order of seconds due to weak interaction with their surroundings[83]. Some applications that utilize this property are quantum computing, specifically using nuclear spins as quantum registers [52][84], magnetic resonance-based biosensing [85], NV-based magnetometry [86], and active quantum error correction [87, 88, 89], each requiring a high degree of control over nuclear spins. Therefore, polarization of the nuclear spin into a single spin-state is of significant interest [12, 51, 66, 67, 90, 91]. Past experiments typically use a level-anticrossing (LAC) in the ground or excited state accessed via a strong Zeeman splitting due to a strong magnetic field (510 G). While in the vicinity of the LAC, the electronic spin state mixing is maximized, allowing for transition between spin levels. Due to the nature of spin conserving transitions, this allows for a spin "flip-flop" interaction to take place between the electronic and nuclear spin [51, 66, 91]. Such techniques have been used with ensembles [90] and single NV centers [66] at both cryogenic and room temperatures.

In this section we explore nuclear spin polarization in a regime further away from the LAC explored extensively by previous studies. By using the spin-preserving excited state transitions of an NV center we demonstrate nuclear spin pumping that can be used in addition to our CPT-based magnetometer to increase the sensitivity of our sensor to smaller magnetic field fluctuations.

7.2. Theory

For our experiments, we utilize the total spin preserving optical transitions of the NV center to optically pump from the nuclear spin of the NV. This process is mediated by the hyperfine interaction which couples the NV electron spin to the ^{14}N nuclear spin [51, 91]. In order to transfer an electron spin flip to a nuclear spin flop, some degree of electronic state mixing is necessary. For a NV center in the presence of no external fields, each of its excited states has a single spin character as discussed in Chapter II, making the probability of flipping the nuclear spin ≈ 0 [51]. In many nuclear spin control experiments, maximal state mixing is attained by placing a strong magnetic field along the electronic spin's quantization axis until the separation between the E_y and E_1 states reach an excited state level anti-crossing (ESLAC) (Fig 7.1). In the presence of the ESLAC, there exists significant state mixing which allows for E_1 to decay to $m_s = 0$ with greater probability the closer the states are to the anti-crossing. Additionally, the E_2 excited state is mixed with E_x via the spin-spin, transverse Zeeman, and transverse hyperfine interactions [66]. This allows for a weaker path to E_2 from $m_s = 0$, which in turn preferentially decays to $m_s = -1$. Alternatively, state mixing required for nuclear spin pumping can be found using NV centers with a high degree of strain, as seen in Section 2.4 Eq. 2.4. Comparing Figure 2.4 with Figure 7.1 one can see a similar ESLAC which suggests an analogous scheme is possible for nuclear spin polarization. Therefore, for our experiments we use the natural strain splitting of our NV center in order to achieve nuclear spin polarization.

Figure 7.2 outlines the cascaded pumping scheme used in [66], where electrons are pumped from $|+1\rangle$ to $|0\rangle$ via $|E_1\rangle$ and from $|0\rangle$ to $|-1\rangle$ via $|E_2\rangle$. Excited states $E_{1,2}$ have strong transitions from $m_s = \pm1$, respectively. However,
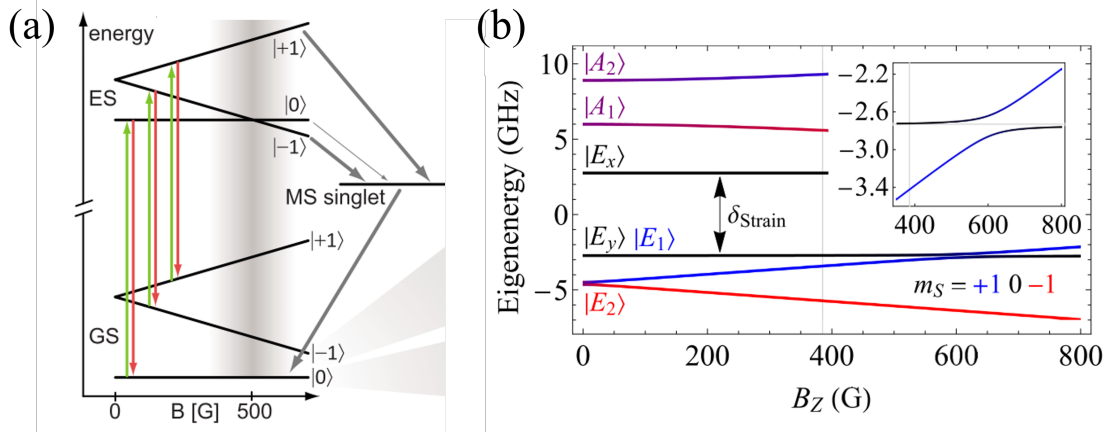
FIGURE 7.1. **(a)** Schematic from [51] depicting the effects of an external magnetic field on the ground and excited states of the NV without strain. **(b)** Figure from [66] which shows how the excited state LAC can be reached using a strong magnetic field. Due to the strain of this particular NV, an even stronger magnetic field is required to reach the LAC.

in the presence of strain or magnetic fields, sufficient state mixing allows for transitions from the $|0\rangle$ spin state to these excited states. The depiction in Figure 7.2 shows that pumping the strong transition $|+1\rangle \rightarrow |E_1\rangle$, which has a small probability of decaying to $|0\rangle$, can yield an electronic spin flip. While simultaneously pumping the weak $|0\rangle \rightarrow |E_2\rangle$ transition, preferentially decays to the $m_s = -1$ state results in an electronic spin flip in the same direction. Since each transition results in $\Delta m_s = -1$, in order to conserve the total spin a $\Delta m_I = +1$ occurs. After a sufficient number of optical cycles, the NV center's nuclear spin can be pumped to $m_I = +1$ by pumping it's electronic spin to $m_s = -1$.

For our experiment, we attempt to polarize the nuclear spin using only the $|0\rangle \rightarrow |E_2\rangle$ transition in an excited state configuration away from the ESLAC; aiming to improve the degree of polarization with repeated optical pumping. After pumping the $|0\rangle \rightarrow |E_2\rangle$ to its steady state, we can apply a MW π-pulse tuned
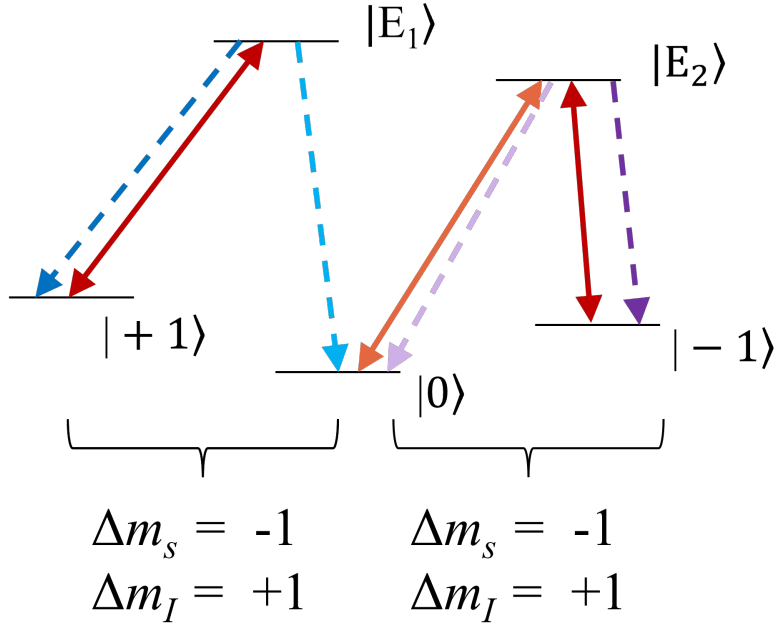
FIGURE 7.2. Transitions used in [66] for nuclear spin pumping. The optical transitions shown in red between $|+1\rangle \rightarrow |E_1\rangle$ and $|-1\rangle \rightarrow |E_2\rangle$ are degenerate and the forbidden $|0\rangle \rightarrow |E_2\rangle$ transition is in orange. Primary decay paths from $|E_1\rangle$ and $|E_2\rangle$ are dark blue and purple, respectively, while the forbidden decay paths are shaded in a lighter color. Each excitation and decay process that results in an electron spin flip, via a the hyperfine interaction, induces a nuclear spin flop in the other direction.

to $|-1\rangle \rightarrow |0\rangle$ ground state transition, allowing for us to repump the $|0\rangle \rightarrow |E_2\rangle$ optical transition. Some advantages to this approach are that it does not require a large magnetic field which has been shown to reduce fluorescence of the NV [92]. Also, this technique can be used with any degree of strain where the $|0\rangle \rightarrow |E_2\rangle$ is resolved.

7.3. Experiment

Experiments were carried out using the same optical setup discussed in Chapter III.

7.3.1. Determining transitions

In order to observe the lower frequency transitions required for nuclear spin polarization we must first identify the relevant transitions using pump-probe spectroscopy. While a carrier (pump) frequency is tuned to the $|0\rangle \rightarrow |E_y\rangle$ transition we sweep out the lower frequency transitions with an optical sideband (probe) generated from an EOM which we drive using an RF source (Figure 7.3). As the sideband passes over transitions that excite from $m_s = 0$ ground state spin, it partially depletes the population in that spin projection resulting in a dip of fluorescence. While as the laser is swept over the $|\pm 1\rangle$ transitions the population in $m_s = 0$ grows, resulting in the peaks seen in Figure 7.3b.
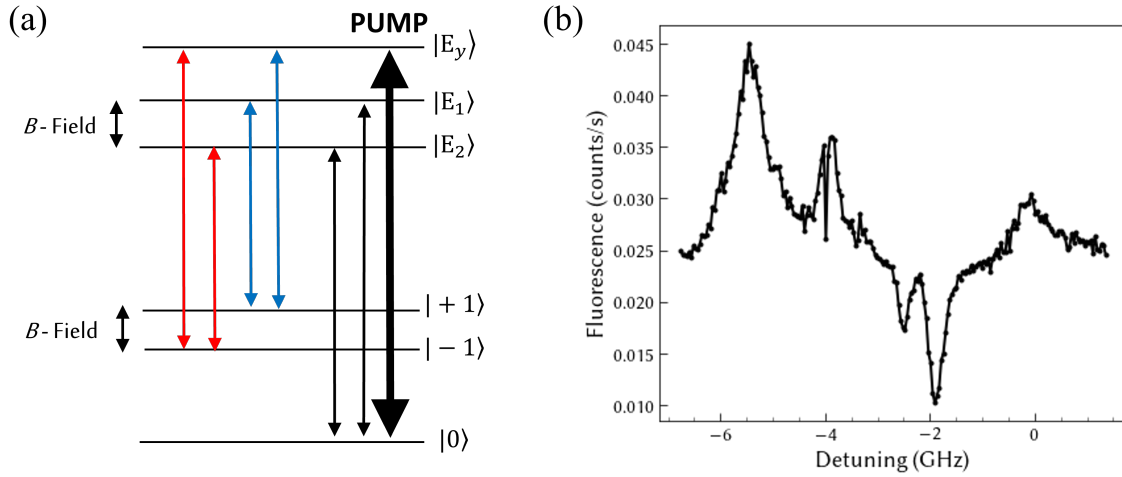
FIGURE 7.3. **(a)** Energy Level schematic of the pump-probe spectra taken in (b). **(b)** Pump-probe spectra while pumping the $|0\rangle \rightarrow |E_y\rangle$ transition. Dips in the spectra demonstrate less population in the $|0\rangle$ state due to optical pumping out of $|0\rangle$ from the probe, while peaks show optical cycling into the $|0\rangle$ state due to the probe pumping the electron population from $|\pm 1\rangle$ states

This is a necessary step for any experiment involving multiple transitions. Since the excitation beam can scatter, exciting other NV centers, multiple NV spectra can be observed in a single PLE scan. Using pump-probe, one can deduce

the spin character of each transition which is a necessary for confident transition identification.

7.3.2. Nuclear Spin Pump

To determine the duration of optical pumping on the $|0\rangle \to |E_2\rangle$ transition we perform a time-resolved PLE similar to that in Section 3.3 Figure 3.5. First we initialize the NV into the $m_s = 0$ state with a 10 μs green pulse. This is followed by a 30 μs red pulse tuned to the $|0\rangle \to |E_2\rangle$ transition. Acquisition of time-resolved PLE data is taken using a Picoquant TimeHarp 260 which interfaces with the computer via a PCIe slot. Inputs to the Picoquant include a sync pulse, which we place after our green initialization pulse, and the photon counts from our detector, which are time-tagged relative to the sync pulse. The decay observed in Figure 7.4 shows the number of integrated photon counts observed after 400 s of the previously described pulse sequence with an optical power of 11 μW. Optical pumping reaches a steady state after 5 μs.

MW induced spin transitions are nuclear spin preserving [42], therefore readout of the NV center's nuclear spin state is performed via hyperfine resolved ODMR, detailed in Section 3.4.1. Figure 7.5 shows readout of a nuclear spin pumped NV using either the $m_s = 0 \to m_s = +1$ or $m_s = -1$ transition. After pumping on the $|0\rangle \to |E_2\rangle$ transition, we expect the m_I projection to be biased towards $m_I = +1$. We expect the $|m_s = 0, m_I = +1\rangle \to |m_s = -1, m_I = +1\rangle$ to be higher in energy (Figure 2.2) and the reverse for the transition to $|m_s = -1, m_I = +1\rangle$, according to the Hamiltonian shown in Eq 2.1. This is consistent with the spectra shown in Figure 7.5.
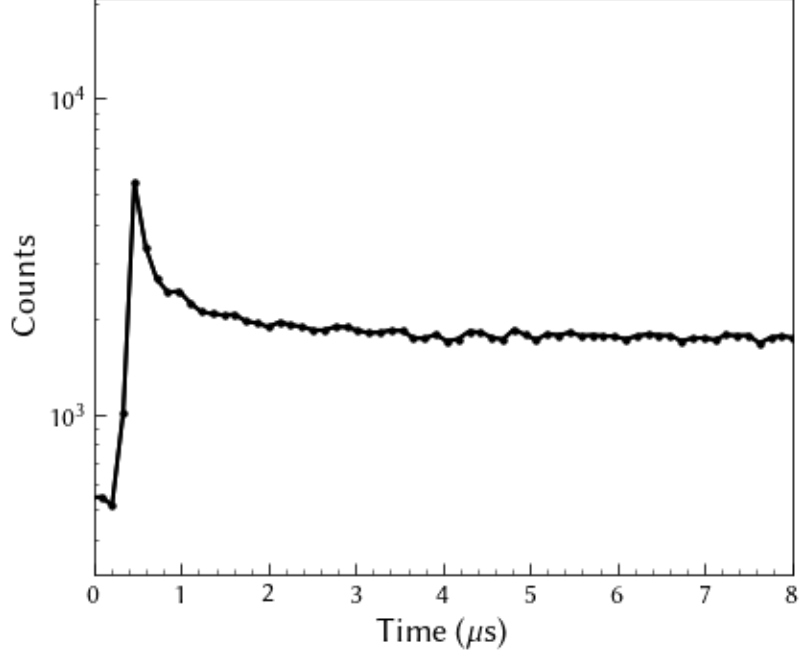
FIGURE 7.4. Time resolved PLE of the $|0\rangle$ to $|E_2\rangle$ transition shows optical pumping out of the initial $m_s = 0$ spin state with a decay that reaches a steady state after 5 μs.

The pulse sequence used for nuclear spin polarization is shown in Figure 7.6. After starting with a 10 μs green initialization pulse, we pump on the $|0\rangle \rightarrow |E_2\rangle$ transition for 5μs. The electron spin population occupies the $m_s = -1$ spin state since the dominant decay path from $|E_2\rangle$ is to $|-1\rangle$. Therefore we apply a strong microwave pulse to invert the population from $|-1\rangle$ to $|0\rangle$. This process is then repeated starting from the nuclear spin pump. With each repeat, the population of nuclear spin flips towards $m_I = +1$ should increase. After N repeats, we apply a weak, hyperfine resolved π-pulse and readout the nuclear spin projection with a 5 μs red laser pulse tuned to the $|0\rangle \rightarrow |E_y\rangle$ transition.

The results of the experiment are shown in Figure 7.7. In Figure 7.7a, after one round of nuclear spin pumping we begin to see the population transfer to the right resonance corresponding to $m_I = +1$. As N increases, the left resonance

80
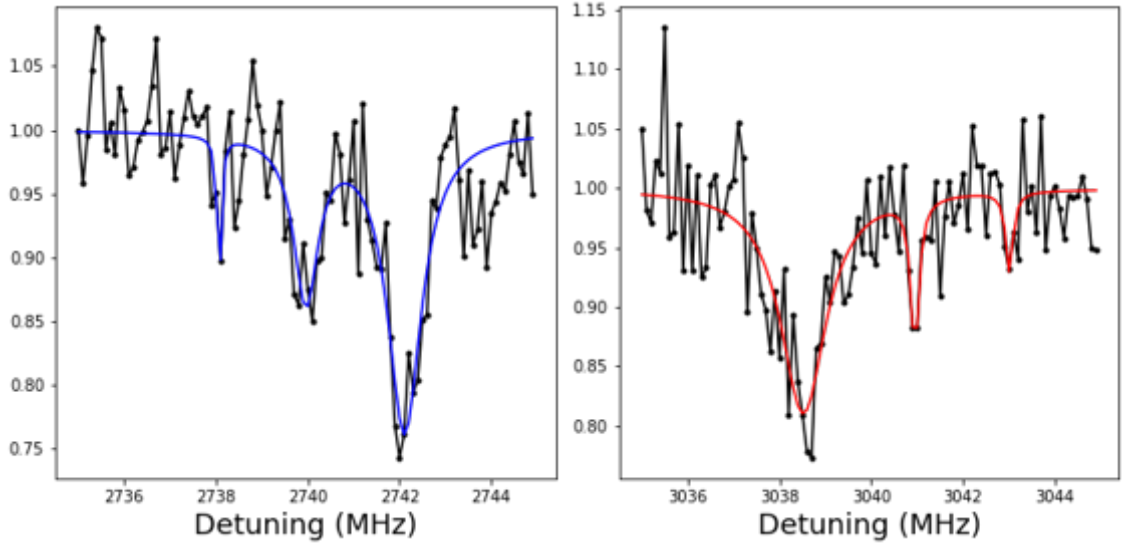
FIGURE 7.5. Hyperfine resolved ODMR spectra of a nuclear spin pumped ^{14}NV as read out via the $|0\rangle \rightarrow |-1\rangle$ (left) and $|0\rangle \rightarrow |+1\rangle$ microwave transition.

appears to get smaller relative to the other spin projections until it disappears for $N = 20$. It can also be seen that the ODMR signal gets increasingly noisier as we increase N. This could be attributed to less averaging taking place for each measurement since the acquisition time for each data point is kept constant and the duty cycle of our pulse sequence (Fig 7.6) increases. The noisier ODMR signal could also be due to ionization of the NV center since each increase in N also increases the total time of resonant excitation. This point could be solved by checking the ionization after readout, allowing for subtraction of points where the NV has been ionized, an approach used by past experiments [66].

We infer the population in each spin projection by summing the total amplitude of each dip and dividing each amplitude by the total. A plot of the population in each spin projection is shown in Figure 7.7b. Under closer inspection of Figure 7.7b we confirm our observation in Figure 7.7a and see the population in $m_s = -1$ drop to zero as well as the population in $m_I = +1$ increasing to
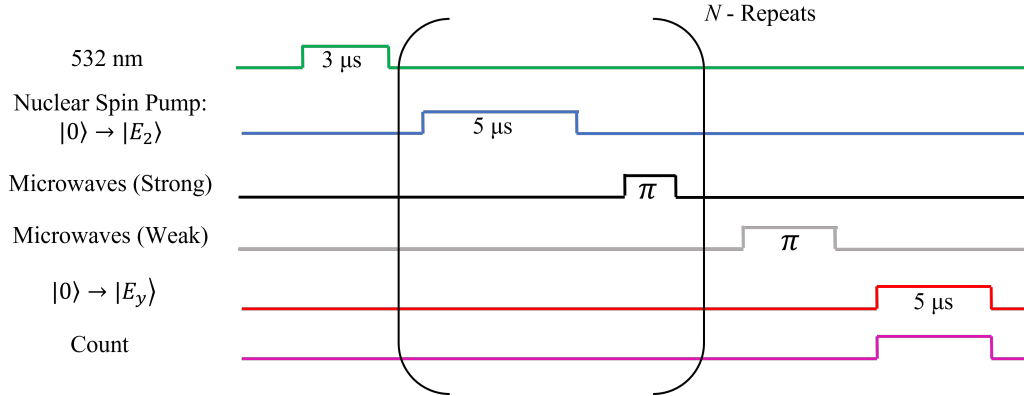
FIGURE 7.6. Pulse sequence used for nuclear spin pumping.
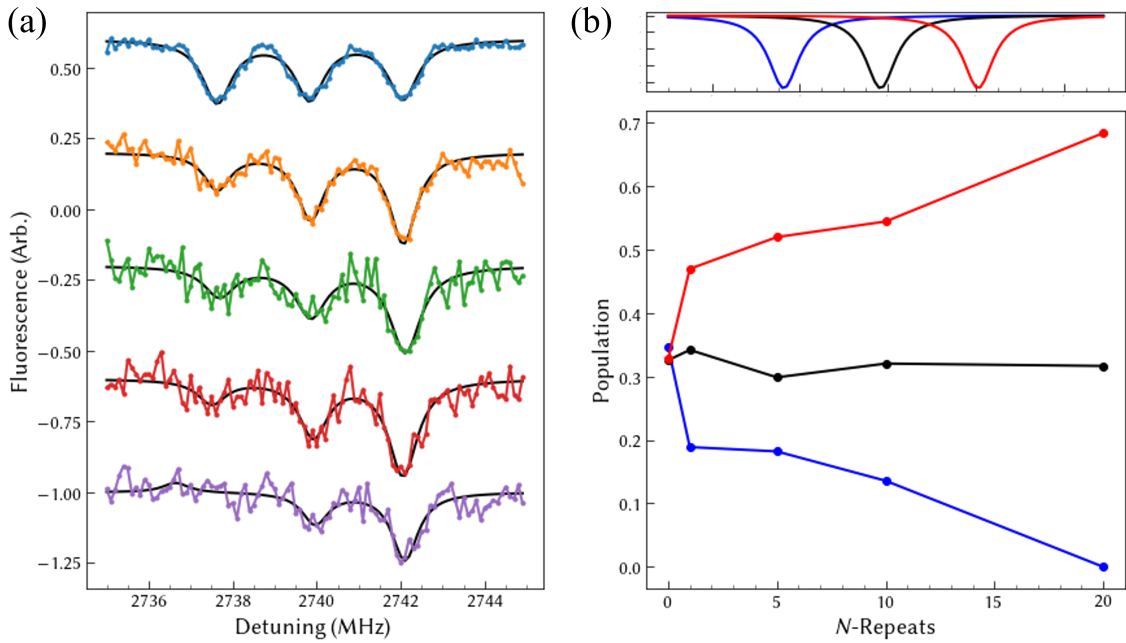
FIGURE 7.7. **(a)** Hyperfine ODMR readouts for increasing number of repeated nuclear spin pumps (blue:0, orange:1, green:5, red:10, purple:20). Spectra are vertically offset in order to better show the difference between successive trials.**(b)** Population in each nuclear spin state for different values of N. The upper plot shows each nuclear spin resonance of $m_I = -1, 0, +1$ from left to right to be used as a color reference.

about 70%. Interestingly, the $m_I = 0$ population remains steadily around 30%.

This might mean that another transition is required to flip the rest of the nuclear

82

spins as in [66] or that more repeats are needed. We did not attempt more repeats, however, since the quality of our ODMR signal appeared to decay.

7.4. Summary

In summary, we briefly discussed the previous approaches to nuclear spin polarization and developed our own approach which utilizes state mixing due to the presence of strain in the NV center's environment to perform nuclear spin pumping. We were able to polarize the nuclear spin of the NV center to a population of 70% in the $m_I = +1$ spin projection as confirmed by readout using ODMR. Next steps for progressing this technique for real-time sensing would require readout of the nuclear spin states using CPT. Nuclear spin polarization reduces the hyperfine contribution to the linewidth of the CPT spectral response and therefore enhances the sensitivity of our CPT sensor. This has the potential to make our sensor sensitive enough to detect the time-varying magnetic field generated by nearby ^{13}C spins found in diamond which are a primary decoherence source for the NV center.

CHAPTER VIII

CONCLUSIONS

Quantum sensing explores the pragmatism that a quantum system has to offer by measuring the system's sensitivity to physical quantities which are typically seen as an obstacles to the system's utility. Instead, such a weakness can be used to learn more about the quantum system and its environment with the potential to take advantage of newly discovered properties for future technologies.

8.1. Summary

In this dissertation, we took steps beyond the typical two-level quantum sensing workhorse of Ramsey interferometry, Using a confocal microscopy setup we put to use a naturally occurring Λ-type three level system in the NV center to place the NV in an optically induced dark state. We probed the sensitivity of the dark state's spectral response to magnetic fields, finding that we can use the wall of the optically quenched fluorescence dip as a way to track the time-varying fields known to be found in the NV center's solid state environment [13].

In Chapter V, we sought out to correlate the change in fluorescence with a fluctuating magnetic field by estimating the corresponding field. We compared various estimators with our own input noise, finding that by taking advantage of the statistical properties of the field, we can greatly enhance the performance of our estimator. With the detection of a single photon, we can generate an updated estimation of the time-varying magnetic field in real time. Consequentially the accuracy of the real-time dynamics can be improved by increasing the photon

count rate via optical excitation power. This, however, comes with a sensitivity trade off due to the power broadening of the CPT spectral response.

Feeding our estimated signal back into the quantum system using feedback control, we found an enhanced sensitivity to the fluctuating field and discovered that the sensitivity of our estimator to the statistical parameters of the estimated field can be optimized. By optimizing the improvement in the spin dephasing of the ground state spin system due to feedback control of the system, new information can be acquired about the NV center's surroundings. However, our system is only sensitive to large fluctuations caused by our artificial input noise.

To improve the sensitivity of our CPT-based sensor, we used the total spin preserving excited state transitions of the NV to shrink the hyperfine contribution of the ^{14}N spins to the CPT linewidth. The nuclear spin of the NV could was polarized 70% to the $m_I = +1$ spin projection. By totally eliminating the $m_I = -1$ spin contribution, we made promising strides toward lowering the linewidth away from the excited state level anti-crossing.

8.2. Future Work

A primary goal for our single-photon magnetometer is to measure the real-time dynamics of the ^{13}C spin bath. Further steps toward this goal would be readout of the NV center's nuclear spin projections after nuclear spin pumping, effectively reducing the linewidth so that smaller amplitude fluctuations could be sensed. Introducing our feedback control technique one can optimize the T_2^* with respect to the input statistical parameters of our estimator to inform further spin bath models.

Development of a real-time magnetometer with the added benefit of feedback control using a single solid-state spin add a new and powerful tool to the quantum sensing toolkit. Using the NV center as a model system for this proof-of-principle demonstration, the technique we have described can be expanded to other solid state spin systems [80]. Magnetometry applied to investigations of time-varying magnetic fields in nanoscale system, for example, nuclear spin baths [12, 13, 14], and two-dimensional semiconductors [9, 10] can develop further understanding of these systems.

REFERENCES CITED

[1] Jeremy L. O'Brien, Akira Furusawa, and Jelena Vučković. Photonic quantum technologies. *Nature Photonics*, 3(12):687–695, 2009. ISSN 17494885. doi: 10.1038/nphoton.2009.229.

[2] Gershon Kurizki, Patrice Bertet, Yuimaru Kubo, Klaus Mølmer, David Petrosyan, Peter Rabl, and Jörg Schmiedmayer. Quantum technologies with hybrid systems. *Proceedings of the National Academy of Sciences of the United States of America*, 112(13):3866–3873, 2015. ISSN 10916490. doi: 10.1073/pnas.1419326112.

[3] Takeshi Koshiba. Quantum cryptography. *Handbook of Natural Computing*, 3-4 (January):1521–1543, 2012. doi: 10.1007/978-3-540-92910-9_45.

[4] Carlton M. Caves. Quantum-mechanical noise in an interferometer. *Physical Review D*, 23(8):1693–1708, 1981. ISSN 05562821. doi: 10.1103/PhysRevD.23.1693.

[5] Dmitry Budker and Michael Romalis. Optical magnetometry. *Nature Physics*, 3: 227–234, 2007. ISSN 17452481. doi: 10.1038/nphys566.

[6] Vittorio Giovannetti, Seth Lloyd, and Lorenzo MacCone. Advances in quantum metrology. *Nature Photonics*, 5(4):222–229, 2011. ISSN 17494885. doi: 10.1038/nphoton.2011.35.

[7] Ashley Montanaro. Quantum algorithms: An overview. *npj Quantum Information*, 2(1):1–8, 2016. ISSN 20566387. doi: 10.1038/npjqi.2015.23. URL http://dx.doi.org/10.1038/npjqi.2015.23.

[8] T. D. Ladd, F. Jelezko, R. Laflamme, Y. Nakamura, C. Monroe, and J. L. O'Brien. Quantum computers. *Nature*, 464(7285):45–53, 2010. ISSN 00280836. doi: 10.1038/nature08812.

[9] I. Lovchinsky, J. D. Sanchez-Yamagishi, E. K. Urbach, S. Choi, S. Fang, T. I. Andersen, K. Watanabe, T. Taniguchi, A. Bylinskii, E. Kaxiras, P. Kim, H. Park, and M. D. Lukin. Magnetic resonance spectroscopy of an atomically thin material using a single-spin qubit. *Science*, 355(6324):503–507, 2017. ISSN 10959203. doi: 10.1126/science.aal2538.

[10] L. Thiel, Z. Wang, M. A. Tschudin, D. Rohner, I. Gutiérrez-Lezama, N. Ubrig, M. Gibertini, E. Giannini, A. F. Morpurgo, and P. Maletinsky. Probing magnetism in 2D materials at the nanoscale with single-spin microscopy. *Science*, 364(6444):973–976, 2019. ISSN 10959203. doi: 10.1126/science.aav6926.

[11] Gopalakrishnan Balasubramanian, Philipp Neumann, Daniel Twitchen, Matthew Markham, Roman Kolesov, Norikazu Mizuochi, Junichi Isoya, Jocelyn Achard, Johannes Beck, Julia Tissler, Vincent Jacques, Philip R. Hemmer, Fedor Jelezko, and Jörg Wrachtrup. Ultralong spin coherence time in isotopically engineered diamond. *Nature Materials*, 8(5):383–387, 2009. ISSN 14764660. doi: 10.1038/nmat2420.

[12] E. Togan, Y. Chu, A. Imamoglu, and M. D. Lukin. Laser cooling and real-time measurement of the nuclear spin environment of a solid-state qubit. *Nature*, 478(7370):497–501, 2011. ISSN 00280836. doi: 10.1038/nature10528. URL http://dx.doi.org/10.1038/nature10528.

[13] Shu Hao Wu, Ethan Turner, and Hailin Wang. Continuous real-time sensing with a nitrogen-vacancy center via coherent population trapping. *Physical Review A*, 103:1–10, 2021. ISSN 24699934. doi: 10.1103/PhysRevA.103.042607.

[14] Wen Yang, Wen Long Ma, and Ren Bao Liu. Quantum many-body theory for electron spin decoherence in nanoscale nuclear spin baths. *Reports on Progress in Physics*, 80(1), 2017. ISSN 00344885. doi: 10.1088/0034-4885/80/1/016001.

[15] C. L. Degen, F. Reinhard, and P. Cappellaro. Quantum sensing. *Reviews of Modern Physics*, 89:1–39, 2017. ISSN 15390756. doi: 10.1103/RevModPhys.89.035002.

[16] Andrew D. Ludlow, Martin M. Boyd, Jun Ye, E. Peik, and P. O. Schmidt. Optical atomic clocks. *Reviews of Modern Physics*, 87(2):637–701, 2015. ISSN 15390756. doi: 10.1103/RevModPhys.87.637.

[17] Romana Schirhagl, Kevin Chang, Michael Loretz, and Christian L. Degen. Nitrogen-vacancy centers in diamond: Nanoscale sensors for physics and biology. *Annual Review of Physical Chemistry*, 65:83–105, 2014. ISSN 0066-426X. doi: 10.1146/annurev-physchem-040513-103659.

[18] D. Carney, G. Krnjaic, D. C. Moore, C. A. Regal, G. Afek, S. Bhave, B. Brubaker, T. Corbitt, J. Cripe, N. Crisosto, A. Geraci, S. Ghosh, J. G.E. Harris, A. Hook, E. W. Kolb, J. Kunjummen, R. F. Lang, T. Li, T. Lin, Z. Liu, J. Lykken, L. Magrini, J. Manley, N. Matsumoto, A. Monte, F. Monteiro, T. Purdy, C. J. Riedel, R. Singh, S. Singh, K. Sinha, J. M. Taylor, J. Qin, D. J. Wilson, and Y. Zhao. Mechanical quantum sensing in the search for dark matter. *Quantum Science and Technology*, 6(2), 2021. ISSN 20589565. doi: 10.1088/2058-9565/abcfcd.

[19] Vittorio Giovannetti, Seth Lloyd, and Lorenzo Maccone. Quantum-enhanced measurements: Beating the standard quantum limit. *Science*, 306(5700): 1330–1336, 2004. ISSN 00368075. doi: 10.1126/science.1104149.

[20] Vittorio Giovannetti, Seth Lloyd, and Lorenzo MacCone. Quantum metrology. *Physical Review Letters*, 96(1):13–16, 2006. ISSN 10797114. doi: 10.1103/PhysRevLett.96.010401.

[21] I. K. Kominis, T. W. Kornack, J. C. Allred, and M. V. Romalis. A subfemtotesla multichannel atomic magnetometer. *Nature*, 422:596–599, 2003. ISSN 00280836. doi: 10.1038/nature01484.

[22] H. B. Dang, A. C. Maloof, and M. V. Romalis. Ultrahigh sensitivity magnetic field and magnetization measurements with an atomic magnetometer. *Applied Physics Letters*, 97:28–30, 2010. ISSN 00036951. doi: 10.1063/1.3491215.

[23] Robert Maiwald, Dietrich Leibfried, Joe Britton, James C. Bergquist, Gerd Leuchs, and David J. Wineland. Stylus ion trap for enhanced access and sensing. *Nature Physics*, 5:551–554, 2009. ISSN 17452481. doi: 10.1038/nphys1311.

[24] Michael J. Biercuk, Hermann Uys, Aaron P. VanDevender, Nobuyasu Shiga, Wayne M. Itano, and John J. Bollinger. Optimized dynamical decoupling in a model quantum memory. *Nature*, 458:996–1000, 2009. ISSN 00280836. doi: 10.1038/nature07951.

[25] I. Baumgart, J. M. Cai, A. Retzker, M. B. Plenio, and Ch Wunderlich. Ultrasensitive magnetometer using a single atom. *Physical Review Letters*, 116:1–5, 2016. ISSN 10797114. doi: 10.1103/PhysRevLett.116.240801.

[26] J. M. Taylor, P. Cappellaro, L. Childress, L. Jiang, D. Budker, P. R. Hemmer, A. Yacoby, R. Walsworth, and M. D. Lukin. High-sensitivity diamond magnetometer with nanoscale resolution. *Nature Physics*, 4:810–816, 2008. ISSN 17452481. doi: 10.1038/nphys1075.

[27] D. Le Sage, K. Arai, D. R. Glenn, S. J. Devience, L. M. Pham, L. Rahn-Lee, M. D. Lukin, A. Yacoby, A. Komeili, and R. L. Walsworth. Optical magnetic imaging of living cells. *Nature*, 496:486–489, 2013. ISSN 00280836. doi: 10.1038/nature12072. URL http://dx.doi.org/10.1038/nature12072.

[28] Roger R Fu, Benjamin P Weiss, Eduardo A Lima, Richard J Harrison, Xue ning Bai, Steven J Desch, Denton S Ebel, Clément Suavet, Huapei Wang, David Glenn, David Le Sage, Takeshi Kasama, Ronald L Walsworth, and Aaron T Kuan. A (5). 346:1089–1093, 2014.

[29] F Dolde, H Fedder, M W Doherty, T Nöbauer, F Rempp, G Balasubramanian, T Wolf, F Reinhard, L C L Hollenberg, F Jelezko, and J Wrachtrup. Electric-field sensing using single diamond spins. *Nature Physics*, 7:459–463, 2011. ISSN 1745-2473. doi: 10.1038/nphys1969. URL `http://dx.doi.org/10.1038/nphys1969`.

[30] Marcus W. Doherty, Viktor V. Struzhkin, David A. Simpson, Liam P. McGuinness, Yufei Meng, Alastair Stacey, Timothy J. Karle, Russell J. Hemley, Neil B. Manson, Lloyd C.L. Hollenberg, and Steven Prawer. Electronic properties and metrology applications of the diamond nv - center under pressure. *Physical Review Letters*, 112:1–5, 2014. ISSN 00319007. doi: 10.1103/PhysRevLett.112.047601.

[31] P. Neumann, I. Jakobi, F. Dolde, C. Burk, R. Reuter, G. Waldherr, J. Honert, T. Wolf, A. Brunner, J. H. Shim, D. Suter, H. Sumiya, J. Isoya, and J. Wrachtrup. High-precision nanoscale temperature sensing using single defects in diamond. *Nano Letters*, 13:2738–2742, 2013. ISSN 15306984. doi: 10.1021/nl401216y.

[32] T. Staudacher, F. Ziem, L. Häussler, R. Stöhr, S. Steinert, F. Reinhard, J. Scharpf, A. Denisenko, and J. Wrachtrup. Enhancing the spin properties of shallow implanted nitrogen vacancy centers in diamond by epitaxial overgrowth. *Applied Physics Letters*, 101(21), 2012. ISSN 00036951. doi: 10.1063/1.4767144.

[33] Hwang Lee, Pieter Kok, and Jonathan P. Dowling. A quantum Rosetta stone for interferometry. *Journal of Modern Optics*, 49(14-15):2325–2338, 2002. ISSN 09500340. doi: 10.1080/0950034021000011536.

[34] Spin Resonance Hahn, E.L. Spin Resonance Experiments J. 1070(1953), 1961.

[35] H. Y. Carr and E. M. Purcell. Effects of diffusion on free precession in nuclear magnetic resonance experiments. *Physical Review*, 94(3):630–638, 1954. ISSN 0031899X. doi: 10.1103/PhysRev.94.630.

[36] K. Khodjasteh and D. A. Lidar. Fault-tolerant quantum dynamical decoupling. *Physical Review Letters*, 95(18):1–4, 2005. ISSN 00319007. doi: 10.1103/PhysRevLett.95.180501.

[37] Zhi Hui Wang, G. De Lange, D. Ristè, R. Hanson, and V. V. Dobrovitski. Comparison of dynamical decoupling protocols for a nitrogen-vacancy center in diamond. *Physical Review B - Condensed Matter and Materials Physics*, 85(15):57–61, 2012. ISSN 10980121. doi: 10.1103/PhysRevB.85.155204.

[38] E. R. Macquarrie, T. A. Gosavi, S. A. Bhave, and G. D. Fuchs. Continuous dynamical decoupling of a single diamond nitrogen-vacancy center spin with a mechanical resonator. *Physical Review B - Condensed Matter and Materials Physics*, 92(22):1–13, 2015. ISSN 1550235X. doi: 10.1103/PhysRevB.92.224419.

[39] V. M. Acosta, K. Jensen, C. Santori, D. Budker, and R. G. Beausoleil. Electromagnetically induced transparency in a diamond spin ensemble enables all-optical electromagnetic field sensing. *Physical Review Letters*, 110 (21):1–6, 2013. ISSN 00319007. doi: 10.1103/PhysRevLett.110.213605.

[40] Kenichi Ohno, F. Joseph Heremans, Lee C. Bassett, Bryan A. Myers, David M. Toyli, Ania C. Bleszynski Jayich, Christopher J. Palmstrøm, and David D. Awschalom. Engineering shallow spins in diamond with nitrogen delta-doping. *Applied Physics Letters*, 101(8), 2012. ISSN 00036951. doi: 10.1063/1.4748280.

[41] Yiwen Chu and Mikhail D. Lukin. Quantum optics with nitrogen-vacancy centers in diamond. Chu, Y., , 2015. URL `http://arxiv.org/abs/1504.05990`.

[42] Marcus W. Doherty, Neil B. Manson, Paul Delaney, Fedor Jelezko, Jörg Wrachtrup, and Lloyd C.L. Hollenberg. The nitrogen-vacancy colour centre in diamond. *Physics Reports*, 528(1):1–45, 2013. ISSN 03701573. doi: 10.1016/j.physrep.2013.02.001. URL `http://dx.doi.org/10.1016/j.physrep.2013.02.001`.

[43] T. Gaebel, M. Domhan, C. Wittmann, I. Popa, F. Jelezko, J. Rabeau, A. Greentree, S. Prawer, E. Trajkov, P. R. Hemmer, and J. Wrachtrup. Photochromism in single nitrogen-vacancy defect in diamond. *Applied Physics B: Lasers and Optics*, 82(2 SPEC. ISS.):243–246, 2006. ISSN 09462171. doi: 10.1007/s00340-005-2056-2.

[44] P. Siyushev, H. Pinto, M. Vörös, A. Gali, F. Jelezko, and J. Wrachtrup. Optically controlled switching of the charge state of a single nitrogen-vacancy center in diamond at cryogenic temperatures. *Physical Review Letters*, 110 (16):1–5, 2013. ISSN 00319007. doi: 10.1103/PhysRevLett.110.167402.

[45] Yoshimi Mita. Change of absorption spectra in type-Ib diamond with heavy neutron irradiation. *Physical Review B - Condensed Matter and Materials Physics*, 53(17):11360–11364, 1996. ISSN 1550235X. doi: 10.1103/PhysRevB.53.11360.

[46] A. Batalov, V. Jacques, F. Kaiser, P. Siyushev, P. Neumann, L. J. Rogers, R. L. McMurtrie, N. B. Manson, F. Jelezko, and J. Wrachtrup. Low temperature studies of the excited-state structure of negatively charged nitrogen-vacancy color centers in diamond. *Physical Review Letters*, 102:1–4, 2009. ISSN 00319007. doi: 10.1103/PhysRevLett.102.195506.

[47] F. Jelezko, T. Gaebel, I. Popa, A. Gruber, and J. Wrachtrup. Observation of Coherent Oscillations in a Single Electron Spin. *Physical Review Letters*, 92 (7):1–4, 2004. ISSN 10797114. doi: 10.1103/PhysRevLett.92.076401.

[48] F. Jelezko, T. Gaebel, I. Popa, M. Domhan, A. Gruber, and J. Wrachtrup. Observation of coherent oscillation of a single nuclear spin and realization of a two-qubit conditional quantum gate. *Physical Review Letters*, 93(13):1–4, 2004. ISSN 00319007. doi: 10.1103/PhysRevLett.93.130501.

[49] Susumu Takahashi, Ronald Hanson, Johan Van Tol, Mark S. Sherwin, and David D. Awschalom. Quenching spin decoherence in diamond through spin bath polarization. *Physical Review Letters*, 101(4):1–4, 2008. ISSN 00319007. doi: 10.1103/PhysRevLett.101.047601.

[50] L. Childress, M. V. Gurudev Dutt, J. M. Taylor, A. S. Zibrov, F. Jelezko, J. Wrachtrup, P. R. Hemmer, and M. D. Lukin. Coherent dynamics of coupled electron and nuclear spin qubits in diamond. *Science*, 314(5797): 281–285, 2006. ISSN 00368075. doi: 10.1126/science.1131871.

[51] Philipp Neumann, Johannes Beck, Matthias Steiner, Florian Rempp, Helmut Fedder, Philip R Hemmer, Jörg Wrachtrup, and Fedor Jelezko. Single-Shot Readout of a Single Nuclear Spin. 329(July):542–545, 2010.

[52] M. V. Gurudev Dutt. Quantum Register Based on Individual electronic and Nuclear SPin Qubits in Diamond. *Science (New York, N.Y.)*, 316(June): 1312–1316, 2007.

[53] Wolfgang Pfaff, Tim H. Taminiau, Lucio Robledo, Hannes Bernien, Matthew Markham, Daniel J. Twitchen, and Ronald Hanson. Demonstration of entanglement-by-measurement of solid-state qubits. *Nature Physics*, 9(1): 29–33, 2013. ISSN 17452481. doi: 10.1038/nphys2444.

[54] V. V. Dobrovitski, A. E. Feiguin, R. Hanson, and D. D. Awschalom. Decay of Rabi oscillations by dipolar-coupled dynamical spin environments. *Physical Review Letters*, 102(23):1–4, 2009. ISSN 00319007. doi: 10.1103/PhysRevLett.102.237601.

[55] Wayne M. Witzel, Malcolm S. Carroll, Aukasz Cywiński, and S. Das Sarma. Quantum decoherence of the central spin in a sparse system of dipolar coupled spins. *Physical Review B - Condensed Matter and Materials Physics*, 86(3):1–27, 2012. ISSN 10980121. doi: 10.1103/PhysRevB.86.035452.

[56] G. De Lange, Z. H. Wang, D. Ristè, V. V. Dobrovitski, and R. Hanson. Universal dynamical decoupling of a single solid-state spin from a spin bath. *Science*, 330(6000):60–63, 2010. ISSN 00368075. doi: 10.1126/science.1192739.

[57] Mohammad Jamali, Ilja Gerhardt, Mohammad Rezai, Karsten Frenner, Helmut Fedder, and Jörg Wrachtrup. Microscopic diamond solid-immersion-lenses fabricated around single defect centers by focused ion beam milling. *Review of Scientific Instruments*, 85, 2014. ISSN 10897623. doi: 10.1063/1.4902818. URL http://dx.doi.org/10.1063/1.4902818.

[58] Ph Tamarat, T. Gaebel, J. R. Rabeau, M. Khan, A. D. Greentree, H. Wilson, L. C.L. Hollenberg, S. Prawer, P. Hemmer, F. Jelezko, and J. Wrachtrup. Stark shift control of single optical centers in diamond. *Physical Review Letters*, 97(8):1–4, 2006. ISSN 00319007. doi: 10.1103/PhysRevLett.97.083002.

[59] Ethan Turner, Shu-Hao Wu, Xinzhu Li, and Hailin Wang. Real-time magnetometry with coherent population trapping in a nitrogen-vacancy center. *Physical Review A*, 105:1–6, 2022. ISSN 2469-9926. doi: 10.1103/physreva.105.l010601.

[60] M. S. Shahriar, P. R. Hemmer, S. Lloyd, P. S. Bhatia, and A. E. Craig. Solid-state quantum computing using spectral holes. *Physical Review A - Atomic, Molecular, and Optical Physics*, 66(3):323011–323016, 2002. ISSN 10502947. doi: 10.1103/PhysRevA.66.032301.

[61] M. O. Scully and M.S.Zubairy. *Quantum Optics*. Cambridge University Press, Cambridge, England, 1997.

[62] Ignas Lekavicius, D. Andrew Golter, Thein Oo, and Hailin Wang. Transfer of phase information between microwave and optical fields via an electron spin. *Physical Review Letters*, 119:1–6, 2017. ISSN 10797114. doi: 10.1103/PhysRevLett.119.063601.

[63] Changjiang Wei and Neil B. Manson. Observation of electromagnetically induced transparency within an electron spin resonance transition. *Journal of Optics B: Quantum and Semiclassical Optics*, 1(4):464–468, 1999. ISSN 14644266. doi: 10.1088/1464-4266/1/4/318.

[64] P. R. Hemmer, A. V. Turukhin, M. S. Shahriar, and J. A. Musser. Raman-excited spin coherences in nitrogen-vacancy color centers in diamond. *Optics Letters*, 26(6):361, 2001. ISSN 0146-9592. doi: 10.1364/ol.26.000361.

[65] Christopher G. Yale, Bob B. Buckley, David J. Christle, Guido Burkard, F. Joseph Heremans, Lee C. Bassett, and David D. Awschalom. All-optical control of a solid-state spin using coherent dark states. *Proceedings of the National Academy of Sciences of the United States of America*, 110(19): 7595–7600, 2013. ISSN 00278424. doi: 10.1073/pnas.1305920110.

[66] M. L. Goldman, T. L. Patti, D. Levonian, S. F. Yelin, and M. D. Lukin. Optical Control of a Single Nuclear Spin in the Solid State. 2018. URL http://arxiv.org/abs/1808.04346.

[67] Benjamin Smeltzer, Jean McIntyre, and Lilian Childress. Robust control of individual nuclear spins in diamond. *Physical Review A - Atomic, Molecular, and Optical Physics*, 80(5):1–4, 2009. ISSN 10502947. doi: 10.1103/PhysRevA.80.050302.

[68] D. Andrew Golter, Thomas K. Baldwin, and Hailin Wang. Protecting a Solid-State Spin from Decoherence Using Dressed Spin States. *Physical Review Letters*, 113(23):1–5, 2014. ISSN 10797114. doi: 10.1103/PhysRevLett.113.237601.

[69] G. Kucsko, P. C. Maurer, N. Y. Yao, M. Kubo, H. J. Noh, P. K. Lo, H. Park, and M. D. Lukin. Nanometre-scale thermometry in a living cell. *Nature*, 500 (7460):54–58, 2013. ISSN 00280836. doi: 10.1038/nature12373.

[70] A. Cooper, E. Magesan, H. N. Yum, and P. Cappellaro. Time-resolved magnetic sensing with electronic spins in diamond. *Nature Communications*, 5:1–7, 2014. ISSN 20411723. doi: 10.1038/ncomms4141.

[71] M. D. Shulman, S. P. Harvey, J. M. Nichol, S. D. Bartlett, A. C. Doherty, V. Umansky, and A. Yacoby. Suppressing qubit dephasing using real-time Hamiltonian estimation. *Nature Communications*, 5(May):1–6, 2014. ISSN 20411723. doi: 10.1038/ncomms6156.

[72] R. Santagati, A. A. Gentile, S. Knauer, S. Schmitt, S. Paesani, C. Granade, N. Wiebe, C. Osterkamp, L. P. McGuinness, J. Wang, M. G. Thompson, J. G. Rarity, F. Jelezko, and A. Laing. Magnetic-field learning using a single electronic spin in diamond with one-photon readout at room temperature. *Physical Review X*, 9:1–18, 2019. ISSN 21603308. doi: 10.1103/PhysRevX.9.021019.

[73] Harry L Van Trees. *Detection, estimation, and modulation theory, part I: detection, estimation, and linear modulation theory.* John Wiley & Sons, 2004.

[74] Cheng Zhang and Klaus Mølmer. Estimating a fluctuating magnetic field with a continuously monitored atomic ensemble. *Physical Review A*, 102(6):1–8, 2020. ISSN 24699934. doi: 10.1103/PhysRevA.102.063716.

[75] C. Bonato, M. S. Blok, H. T. Dinani, D. W. Berry, M. L. Markham, D. J. Twitchen, and R. Hanson. Optimized quantum sensing with a single electron spin using real-time adaptive measurements. *Nature Nanotechnology*, 11(3): 247–252, 2016. ISSN 17483395. doi: 10.1038/nnano.2015.261.

[76] Lucio Robledo, Lilian Childress, Hannes Bernien, Bas Hensen, Paul F.A. Alkemade, and Ronald Hanson. High-fidelity projective read-out of a solid-state spin quantum register. *Nature*, 477(7366):574–578, 2011. ISSN 00280836. doi: 10.1038/nature10401.

[77] Dolev Bluvstein, Zhiran Zhang, and Ania C.Bleszynski Jayich. Identifying and Mitigating Charge Instabilities in Shallow Diamond Nitrogen-Vacancy Centers. *Physical Review Letters*, 122(7):76101, 2019. ISSN 10797114. doi: 10.1103/PhysRevLett.122.076101. URL https://doi.org/10.1103/PhysRevLett.122.076101.

[78] E. Togan, Y. Chu, A. Imamoglu, and M. D. Lukin. Laser cooling and real-time measurement of the nuclear spin environment of a solid-state qubit. *Nature*, 478(7370):497–501, 2011. ISSN 00280836. doi: 10.1038/nature10528.

[79] David A. Hopper, Joseph D. Lauigan, Tzu Yung Huang, and Lee C. Bassett. Real-Time Charge Initialization of Diamond Nitrogen-Vacancy Centers for Enhanced Spin Readout. *Physical Review Applied*, 13(2):1, 2020. ISSN 23317019. doi: 10.1103/PhysRevApplied.13.024016. URL https://doi.org/10.1103/PhysRevApplied.13.024016.

[80] David D. Awschalom, Ronald Hanson, Jörg Wrachtrup, and Brian B. Zhou. Quantum technologies with optically interfaced solid-state spins. *Nature Photonics*, 12(9):516–527, 2018. ISSN 17494893. doi: 10.1038/s41566-018-0232-2. URL http://dx.doi.org/10.1038/s41566-018-0232-2.

[81] Søren Gammelmark and Klaus Mølmer. Bayesian parameter inference from continuously monitored quantum systems. *Physical Review A - Atomic, Molecular, and Optical Physics*, 87(3):1–9, 2013. ISSN 10502947. doi: 10.1103/PhysRevA.87.032115.

[82] Udo Von Toussaint. Bayesian inference in physics. *Reviews of Modern Physics*, 83(3):943–999, 2011. ISSN 00346861. doi: 10.1103/RevModPhys.83.943.

[83] U. F.S. D'Haenens-Johansson, A. M. Edmonds, B. L. Green, M. E. Newton, G. Davies, P. M. Martineau, R. U.A. Khan, and D. J. Twitchen. Optical properties of the neutral silicon split-vacancy center in diamond. *Physical Review B - Condensed Matter and Materials Physics*, 84(24), 2011. ISSN 10980121. doi: 10.1103/PhysRevB.84.245208.

[84] L M K Vandersypen and I L. Chuang: NMR techniques for quantum control and computation 1069. *Rev. Mod. Phys.*, 76(October 2004):1037–1069, 2005. URL `http://journals.aps.org/rmp/abstract/10.1103/RevModPhys.76.1037`.

[85] Leif Schröder, Thomas J. Lowery, Christian Hilty, David E. Wemmer, and Alexander Pines. Molecular imaging using a targeted magnetic resonance hyperpolarized biosensor. *Science*, 314(5798):446–449, 2006. ISSN 00368075. doi: 10.1126/science.1131847.

[86] I Lovechinsky, A.O. Sushkov, E Urbach, N.P. DeLeon, S. Choi, K DeGreve, R Evans, R Gertner, E Bersin, C Miller, L McGuinness, F Jelezko, R. L Walsworh, H Park, and M. D. Lukin. Nuclear magnetic resonance detection and spectroscopy of single proteins using quantum logic. 351(6275):836–842, 2016.

[87] G. Waldherr, Y. Wang, S. Zaiser, M. Jamali, T. Schulte-Herbrüggen, H. Abe, T. Ohshima, J. Isoya, J. F. Du, P. Neumann, and J. Wrachtrup. Quantum error correction in a solid-state hybrid spin register. *Nature*, 506(7487): 204–207, 2014. ISSN 00280836. doi: 10.1038/nature12919.

[88] Masashi Hirose and Paola Cappellaro. Coherent feedback control of a single qubit in diamond. *Nature*, 532(7597):77–80, 2016. ISSN 14764687. doi: 10.1038/nature17404. URL `http://dx.doi.org/10.1038/nature17404`.

[89] J. Cramer, N. Kalb, M. A. Rol, B. Hensen, M. S. Blok, M. Markham, D. J. Twitchen, R. Hanson, and T. H. Taminiau. Repeated quantum error correction on a continuously encoded qubit by real-time feedback. *Nature Communications*, 7(May):1–7, 2016. ISSN 20411723. doi: 10.1038/ncomms11526.

[90] Ran Fischer, Andrey Jarmola, Pauli Kehayias, and Dmitry Budker. Optical polarization of nuclear ensembles in diamond. *Physical Review B - Condensed Matter and Materials Physics*, 87(12):1–7, 2013. ISSN 10980121. doi: 10.1103/PhysRevB.87.125207.

[91] F. Poggiali, P. Cappellaro, and N. Fabbri. Measurement of the excited-state transverse hyperfine coupling in NV centers via dynamic nuclear polarization. *Physical Review B*, 95(19):1–8, 2017. ISSN 24699969. doi: 10.1103/PhysRevB.95.195308.

[92] M. Capelli, P. Reineck, D. W.M. Lau, A. Orth, J. Jeske, M. W. Doherty, T. Ohshima, A. D. Greentree, and B. C. Gibson. Magnetic field-induced enhancement of the nitrogen-vacancy fluorescence quantum yield. *Nanoscale*, 9(27):9299–9304, 2017. ISSN 20403372. doi: 10.1039/c7nr02093g.